Development and Characterization of an Inertial Electrostatic Confinement Device for Space Propulsion Applications

A thesis accepted by the Faculty of Aerospace Engineering and Geodesy of the University of Stuttgart in fullfilment of the requirements for the degree of Doctor of Engineering Sciences (Dr.-Ing.)

by
Constanze Syring
born in
Schwerin

Main referee: apl. Prof. Dr.-Ing. habil. Georg Herdrich

Co-referee: Prof. Dr.-Ing. Stefanos Fasoulas

Co-referee: Prof. Dr.-Ing. Jochen Schein

Day of the exam: 21.02.2023

Institute of Space Systems

University of Stuttgart

2023

Five years of work on this very personal project led me through fullfilling highs and

exhausting lows, which can be described in the best way by:

"The most difficult thing is the decision to act, the rest is merely tenacity."

"The most effective way to do it is to do it."

"It is far easier to start something than it is to finish it."

(Amelia Earhart)

Acknowledgement

Contents

List of Figures

List of Tables

Glossary

Acronyms

DSMC	Direct Simulation Monte Carlo
EEDF	Electron Energy Distribution Function
EP	Electric Propulsion
ESA	European Space Agency
FWHM	Full Width Half Maximum
HSC	High Speed Camera
IEC	Inertial Electrostatic Confinement
IRS	Institut für Raumfahrtsysteme (Institute of Space Systems)
ITER	International Thermonuclear Experimental Reactor
MIT	Massachusetts Institute of Technology
NIF	National Ignition Facility
NIST	National Institut of Standards and Technology
OES	Optical Emission Spectroscopy
PARADE	Plasma Radiation Database
PIC	Particle In Cell
POPS	Periodically Oscillating Plasma Sphere
TRL	Technology Readiness Level

Variables

A_C	m^2	Cathode Surface
A_A	m^2	Anode Surface
A_o	m^2	Open Anode Surface (transparent)
A_g	m^2	Grid Anode Surface
A_{kj}	s^{-1}	Transition Rate Coefficient
c_s	m/s	Sound Velocity
d	m	Electrode Gap

E_C	J	Collision Energy
E_i	eV	Ionization Energy
F	N	Thrust
g	m	Grid Hole Diameter
$g_{i,k}$	-	Degeneracy Factor
$g_{o,A}$	m	Cathode Opening Radius
$g_{o,C}$	m	Anode Opening Radius
I	A	Current
I_B	A	Beam Current
I_D	A	Discharge Current
I_{IC}	A	Circulating Ion Current
I_{PS}	A	Power Supply Current
I_{sp}	s	Specific Impulse
$I_{\hbar\nu}$	A	Secondary Photoelectric Emission Current
k_{ion}	s^{-1}	Ionization Rate Coefficient
N	-	Particle Number
n	m^{-3}	Particle Number Density
n_{core}	m^{-3}	Core Particle Number Density
$n_{e,i}$	m^{-3}	Electron/Ion Particle Number Density
n_H	m^{-3}	Heavy Particle Number Density
n_n	m^{-3}	Neutral Particle Number Density
p	Pa	Pressure
p_{ch}	Pa	Chamber Pressure
P_{Brems}	W	Bremsstrahlung Power
P_{Exc}	W	Excitation Power
P_{Grid}	W	Grid Collision Power
P_{Ion}	W	Ionization Power
r_A	m	Anode Radius
r_C	m	Cathode Radius
r_{core}	m	Core Radius
r_{ed}	m	Edge Radius
r_{jet}	m	Jet Radius
R	N	Friction Force

S	-	Ionization Collision Term
T_e	K	Electron Temperature
T_H	K	Heavy Particle Temperature
T_i	K	Ion Temperature
T_n	K	Neutral Paticle Temperature
U	-	Partition Function
V	V	Voltage
V_D	V	Discharge Voltage
V_{ch}	m^3	Chamber Volume
V_{exc}	m^3	Excitation Volume
V_{ion}	m^3	Ionization Volume
v	m/s	Velocity
x_s	m	Sonic Point Position
Z	-	Charge Number
Z_{av}	-	Average Charge State
α	-	Ionization Degree
β	-	Ratio Jet to Grid Opening Area
γ	-	Adiabatic Index
δ	-	Secondary Electron Emission Coefficient
η_e	-	Effective Transparency
η_g	-	Geometric Transparency
λ	m	Wavelength
ν	s^{-1}	Collision Frequqency
σ_{ion}	m^2	Ionization Cross Section
ζ	-	Number of Valence Electrons
Φ_{well}	V	Potenial Well
χ	[-]	Factor
ω	s^{-1}	Ionization Rate

Constants

A_R	Richardson Constant	$1.20173 \frac{A}{m^2 K^2}$
c_0	Speed of Light in Vacuum	$299792458 m/s$

e	Elementary Charge	$1.602 \cdot 10^{-19} C$
h	Planck's Constant	$6.626 \cdot 10^{-34} Js$
$\hbar$	Reduced Planck Constant	$1.054 \cdot 10^{-34} Js$
k_B	Boltzmann Constant	$1.380 \cdot 10^{-23} J/K$
m_e	Electron Mass	$9.109 \cdot 10^{-31} kg$
R_y	Rydberg Energy	$2.1798 \cdot 10^{-18} J$
S_{Brems}	Bremsstrahlung Radiation Constant	$1.69 \cdot 10^{-38} m^4 \sqrt[2]{\frac{Ckg}{s}}$
ϵ_0	Vacuum Permittivity	$8.854 \cdot 10^{-12} F/m$

Abstract

Future space missions need new technologies which enable scientific revolution or improve competitiveness on the commercial space market. One of the technologies continuously improving and gaining more and more impact on new satellite platform developments are electric space propulsion systems which provide a wide performance envelope at the limits of current technology development and in concepts even further than that. Propulsion systems with arcjets, Hall-Effect thrusters (HET) and gridded ion engines (GIE) gained enough heritage and maturity to be called conventional and cover demands for thrust, specific impulse, efficiency and lifetime for today's needs. However, new concepts need to be analyzed and tested for applicability to new thruster technologies which may provide additional functions as proposed for Inertial Electrostatic Confinement (IEC). This principle, invented for fusion applications, uses electrostatic fields in a spherical grids system to accelerate ions into a confinement where they tend to fuse if the acceleration potential is high enough to reach the necessary velocities. One of the operation modes visible in fusion and non-fusion operation is a jet mode enabling an extraction of particles out of the confinement. Due to that, this technology shall be investigated for propulsion applications in non-fusion operation, which can be called an electric propulsion device with the potential to be enhanced in fusion operation to even higher exit velocities. The *fusion* operation is considered to be a cutting edge - technology factor. Electric propulsion operation may also be maintained with an open grid system, not enclosed with a chassis, enabling the use of the residual atmosphere in a very low earth orbit as propellant. This results into an *airbreathing* electric propulsion system (RAM-EP), which is a second cutting edge - technology factor. A third factor driving a development is *active thrust vector control*, not moving the whole thruster with a mechanical steering mechanism, but moving the plasma beam within the thruster, which is worth to be studied with this technology. All these factors provoked an investigation of the current technology readiness level (TRL) for the IEC device with respect to electric propulsion applications as basis for further cutting edge - technology developments. The levels *basic principle* (TRL1) and *technology concept / application* (TRL2) had already been studied partially before this research has been started at IRS, but the work has been published mainly in parallel to this thesis. For fusion devices the working principle was studied and a database for plasma properties and operation conditions, as well as some analytical models for loss mechanisms are existent. Non-fusion devices in jet mode operation were investigated with respect to a phenomenological de-

scription of the jet extraction and a preliminary assessment of jet plasma properties and operation conditions. Starting from this, the work performed aimed at deepening the knowledge of functionality and design. A test vacuum facility was prepared for tests with grid-based IEC devices. The grid setups were subjected to performance mapping with respect to geometric scaling, propellant and pressure level variation, jet operation modes and power limits (including $I - V$-characteristics) for ignition and continuous operation. Moreover, plasma properties such as species composition in confinement and jet, particle temperatures, and densities were assessed based on assumptions for the particle energy distributions. Plasma modeling in combination with experiments allowed to frame definitions for the different phases such as plasma generation, extraction and acceleration. Assessments of power consumption for ionization and erosion losses are presented and a preliminary model for thrust and specific impulse calculation is described. Concluding from this, the technology readiness level 3 (*characteristic proof-of-concept*) is reached for this technology by combining a profound database of experimental data with models for thrust, specific impulse, and power losses which were validated partially. However, more attention has to be turned on assumptions for the particle energy distributions and particle velocities which should be assessed directly via diagnostic measurements. In that way the understanding of deviations of particle densities depending on the electron temperature can be improved which in turn are input parameters for thrust calculations. Additionally, direct thrust measurements should be performed.

Zusammenfassung

Für zukünftige Raumfahrtmissionen werden stetig neue Technologien gebraucht, welche damit neuen naturwissenschaftlichen Erkenntnisgewinn ermöglichen und die Wettbewerbsfähigkeit auf dem kommerziellen Raumfahrtmarkt verbessern. Eine dieser Technologien sind elektrische Raumfahrtantriebssysteme, die permanenter Entwicklung und Optimierung unterliegen und mehr und mehr Einfluss auf die Entwicklung neuer Satellitenplattformentwicklungen bekommen. Sie ermöglichen einen breiten Leistungsumfang im Bereich der derzeitigen Entwicklungsgrenzen und sind konzeptionell betrachtet noch vielversprechender. Antriebssysteme mit Lichtbogenantrieben, Hall-Effektantrieben (HET) und Gitterionenantrieben (GIE) haben entsprechend genug Flugerfahrung gesammelt und einen Technologiereifegrad erreicht, so dass man sie als konventionelle Technologie bezeichnen kann. Sie decken den heutigen Bedarf an Schub, spezifischem Impuls, Effizienz und Lebensdauer ab. Trotzdem werden neue Konzepte wie der inertiale elektrostatische Trägheitseinschluss (Inertial Electrostatic Confinement - IEC) auf Anwendbarkeit als Antriebssystem untersucht, da sie Zusatzfunktionen möglich machen. Dieses Plasmaeinschlussprinzip wurde für Fusionsenergieanwendungen entwickelt, und benutzt elektrostatische Felder in einem sphärischen Gittersystem, um Ionen in einen Einschluss zu beschleunigen, wo sie bei ausreichend hohem Beschleunigungspotential fusionieren können. Einer der Betriebsmodi, welcher in Fusionsbetrieb und Nicht-Fusionsbetrieb auftritt, ist der Strahlmodus (Jet Mode), der auch die Auskopplung von Teilchen aus dem Einschluss ermöglicht. Aus diesem Grund ist es sinnvoll, diese Technologie auf Antriebsanwendungen im Nicht-Fusionsbetrieb zu untersuchen, wodurch sie den elektrischen Raumfahrtantrieben zugeordnet werden kann. Die Erweiterung durch Fusionsbetrieb könnte sehr hohe Austrittsgeschwindigkeiten ermöglichen, ist aber den fortschrittlichen Antriebskonzepten zuzuordnen. Die Option des *Fusionsbetriebs* ist als abgrenzender Spitzentechnologiefaktor zu bewerten, welcher die Basisentwicklung als elektrischer Raumfahrtantrieb treiben soll. Außerdem könnte ein potentieller elektrischer IEC-Antrieb auch ohne Triebwerksgehäuse betrieben werden, mit einem von dem Restgas umgebenden Gittersystem, was die Umsetzung in ein *Atmosphäre atmendes Triebwerk* (RAM - electric propulsion) erlaubt. Diese Option ist ebenfalls als ein Spitzentechnologiefaktor einzuordnen. Ein dritter Faktor, der die Entwicklung treiben kann und bei dem eine Anwendungsstudie sinnvoll wird, ist die *aktive Schubvektorkontrolle*, bei der nicht das gesamte Triebwerk mittels eines Lenkmechanismus bewegt werden muss, sondern der Plasmastrahl selbst bewegt wird. Diese drei Faktoren haben dazu geführt, dass innerhalb dieser

Arbeit der Technologiereifegrad (Technology Readiness Level - TRL) für das IEC-Prinzip im Hinblick auf die Anwendung elektrischer Antriebe als Basistechnologie geprüft und erweitert wurde. Die Level *grundlegendes Prinzip* (TRL1) und *Technologiekonzept / Anwendung* (TRL2) wurden bereits teilweise untersucht und veröffentlicht, während die IEC Forschung und Entwicklung am IRS vorangetrieben wurde. Für Fusionsgeräte wurde das Funktionsprinzip ausgiebig studiert und dadurch eine Datenbasis für Plasmaeigenschaften und Betriebspunkte geschaffen, sowie teilweise analytische Modelle für Verlustleistungen erstellt. Es wurden Nicht-Fusionsgeräte im Strahlmodus in Bezug auf eine phänomenologische Beschreibung der Strahlauskopplung untersucht und erste Versuche, um die Strahlplasmaeigenschaften und Betriebsbedingungen zu bestimmen, durchgeführt. Ausgehend davon zielte diese Arbeit darauf ab, das Verständnis von Funktionalität und Design zu vertiefen. Eine Vakuumtestkammer wurde für diese Zwecke vorbereitet und ausgerüstet. Der Leistungsumfang wurde mittels Gitterelektrodenkonfigurationen und Variationen von Treibstoffen, Drucklevel, Strahlmodi und Leistungslimits (einschließlich $I-V$-Charakteristiken) für Zündung und kontinuierlichen Betrieb untersucht. Des Weiteren wurden Plasmaeigenschaften wie die Spezieszusammensetzung im Einschluss und im Strahl, sowie Teilchentemperaturen und -dichten basierend auf Annahmen für die Teilchenenergieverteilungsfunktionen bestimmt. Plasmamodellierungen in Kombination mit Experimenten haben es erlaubt, Definitionen für Plasmagenerierung, -extraktion und -beschleunigung zu formulieren. Abschätzungen des Leistungsbedarfs für Ionisation und Erosionsverluste werden vorgestellt and ein erstes Modell zur Berechnung von Schub und spezifischem Impuls beschrieben. Daraus schlussfolgernd ist der Technologiereifegrad (TRL) 3 durch eine Kombination aus einer umfangreichen experimentellen Datenbasis mit Modellen für Schub, spezifischem Impuls und Leistungsverlustmechanismen erreicht worden. Jedoch sollte zukünftig der Fokus auf die Annahmen zur Teilchenenergieverteilungsfunktion und die Teilchengeschwindigkeiten gerichtet werden, die direkt mittels Plasmadiagnostik gemessen werden können, um die Abweichung der Teilchendichten abhängig von der Elektrontemperatur besser zu verstehen, welche wiederum Eingangsgrößen für die Schubberechnung sind. Zusätzlich sollten direkte Schubmessungen durchgeführt werden.

1. Introduction

Demanding space mission concepts for science missions or future manned missions call for highly efficient and highly precise propulsion concepts. Until now, conventional electric propulsion technologies have been developed for moon missions like SMART-1, planetary science missions like GOCE or Beppi Colombo and for fundamental research as performed on a space mission like LISA [1–3]. But requirements for the propulsion system are becoming more stringent and demanding in terms of performance for commercial missions, throtability, accuracy, specific impulse I_{sp}, efficiency and thrust F. Part of the fundamental research at IRS is to evaluate plasma device concepts with respect to their applicability to future propulsion concepts. One of the concepts under investigation is Inertial Electrostatic Confinement (IEC), a plasma confinement device originally invented for fusion applications.

The first IEC device, which was a fusion reactor, was patented by Farnsworth [4] in 1966 and further developed by Hirsch [5]. Then until the 1990s research on IEC was limited due to the more promising technologies of the National Ignition Facility (NIF) and International Thermonuclear Experimental Reactor (ITER) with respect to the fusion gain. But several research groups went on exploring the potential of IEC for other applications such as neutron sources, plasma sources for surface modification and space propulsion systems [6–13], eventually even resulting into potential commercial products [14].

With respect to electric propulsion applications, this concept may offer non-fusion and fusion operation, potentially resulting in a high I_{sp} propulsion system (non-fusion) with the possibility to enhance the system performance by additional heating of plasma fusion processes. *Fusion* operation is considered to be a cutting edge - technology factor, that can drive the base development as electric propulsion system. Non-fusion operation can also be combined to a RAM (*airbreathing*) electric propulsion application with a grid electrode system that is exposed to the residual atmosphere in a low earth orbit. And even *active thrust vector control* is worth a conceptual and experimental study, which allows to steer the plasma beam within the thruster instead of using a steering mechanism that moves the whole thruster. These features should be part of the near future development. However, for an evaluation of the applicability the thrust generation process needs to be understood, so that the base application will be investigated first. Research on this topic assumes an
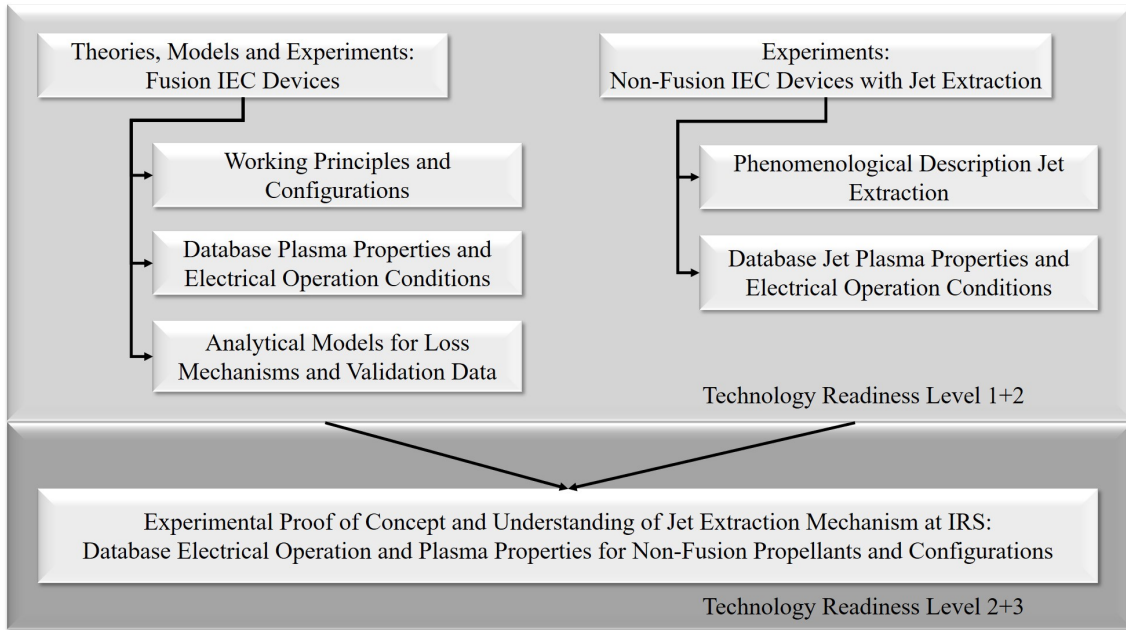
Figure 1.1.: Approach to reach TRL3

electrostatic acceleration mechanism or a combination of thermal expansion and electrostatic acceleration. The focus of this thesis is the proof of concept for a jet extraction of an IEC device at IRS and the understanding of the mechanism leading to a jet.

In the first step the technology readiness level for space applications has been identified. There are definitions for the evaluation of a technology readiness level, which are described in ISO 16290 or ECSS-E-AS-11C (see Table 1.1). The goal is to assess whether the technology readiness level TRL 3 can be reached. The approach depicted in Figure 1.1 has been selected.

A literature research for IEC fusion devices gives enough confidence in adequateness of the confinement theory and a profound database of operation conditions and plasma properties for fusion applications. Some analytical models are available for power estimation of loss mechanisms in these devices too.

With respect to the applicability of IEC devices with jet extraction in non-fusion mode, investigations have been performed at the University of Illinois since 2000, at the Massachusetts Institute of Technology (MIT) since 2004 and at the Institute of Space Systems (IRS), University of Stuttgart since 2011. For this application, the jet mode is essential and therefore research performed aimed at the characterization of this plasma jet. Starting with conceptual studies and experiments at the University of Illinois [9, 16], investigations

Table 1.1.: Technology readiness level definition [15]

No.	TRL	Milestone	Achievement (documented)
1	Basic principles observed and reported	Potential applications are identified following basic observations but element concept not yet formulated	Expression of the basic principles intended for use. Identification of potential applications
2	Technology concept and/or application formulated	Formulation of potential applications and preliminary element concept. No proof of concept yet.	Formulation of potential applications. Preliminary conceptual design of the element, providing understanding of how the basic principles would be used.
3	Analytical and experimental critical function and/or characteristic proof-of-concept	Element concept is elaborated and expected performance is demonstrated through analytical models supported by experimental data/characteristics.	Preliminary performance requirements (can target several missions) including definition of functional performance requirements. Conceptual design of the element. Experimental data inputs, laboratory-based experiment definition and results. Element analytical models for the proof of concept.

were directed into a combined plasma source of a helicon stage and a second IEC stage (Helicon Injected Inertial Plasma Electrostatic Rocket). These experiments included total plasma current measurements with a Faraday cup and electron energy measurements using a gridded energy analyzer [12]. Additionally, a piezo electric sensor was used to study the force generated by the extracted jet. From these experiments, it was derived that the jet may consist primarily of a high-energy electron beam having a peak energy of half of the full grid potential. However, these results did not explain the extraction, but gave a first assessment of some of the jet plasma properties for a combined plasma source. Research conducted at MIT aimed at methods and techniques to improve the confinement and life-time by reducing loss mechanisms, e.g. collisions [11, 17]. In total, this knowledge can be evaluated with a TRL1 to TRL2.

In the second step, a plan is needed that shows how to determine the thrust and how to describe the thrust mechanism. The following possibilities (see Figure 1.2) will allow an evaluation of thrust generation for an IEC device. From the experimental side, direct and indirect thrust measurements can be performed. Direct thrust measurements with a thrust balance were not feasible due to availability constraints of a suitable thrust balance. The latter would have required developing a setup that is able to measure an expected continuous thrust in the μN to mN range at the power levels tested in this thesis. Indirect thrust measurements are usually performed by measuring electrical discharge parameters and calculations of thrust with a set of equations. This in turn requires the fundamental understanding of the thrust generation mechanism, which is also the aim of this work. In that way, indirect thrust estimation would be feasible. This approach deals with a numerical tool that shall enable an estimation of the energy available for thrust generation and an assessment of the thrust generation mechanism itself and the resulting thrust. The simulation assessment also requires input data in terms of geometric dimensions, electrical operation parameters and plasma properties. After these first assessments the research at IRS with respect to IEC started from scratch when the first IEC setup was operated in 2011. There is a profound expertise of electric propulsion systems at IRS, but less knowledge about fusion devices with respect to experiments. For that reason, the first goal was not to assess completely the jet properties right away, but rather to understand the phenomena in an IEC device leading to a jet extraction. In that way, the work published in this report is not only complementary to the work of the University of Illinois, but also critical for the evaluation of a potential IEC thruster. This work includes
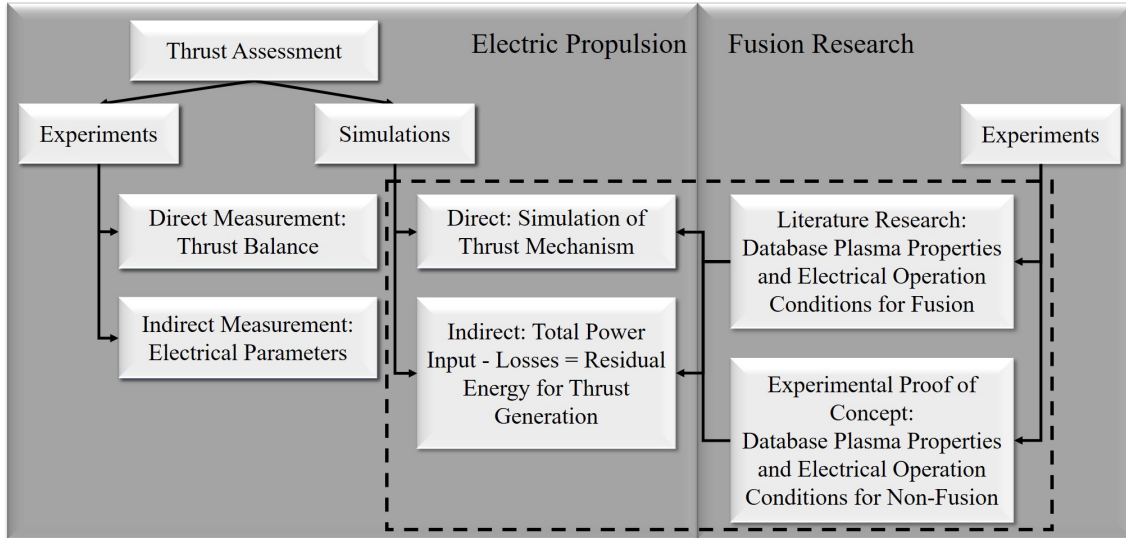
Figure 1.2.: Thrust assessment for application evaluation

investigations of discharge behavior with respect to a pre-conditioning phase, ignition with different electrode designs, operation of these setups in different modes and with different propellants. Moreover, the plasma composition of confinement and extraction plasma will be presented. And finally, videos taken with a high-speed camera will show the stability of certain operation modes and the triggering phenomenon for the transitions between the operation modes is presented.

Although not part of this thesis, from a numerical point of view the following work has been performed in recent years in parallel. An ESA-Ariadna study for the kinetic modeling (Particle-In-Cell) of the jet extraction out of an IEC device indicated that in fact electrons could leave the plasma confinement [18], supporting the results of the University of Illinois. However, only insufficient leads were found that could give information about the ion's behavior in this jet. The budget of this study gave only limited access to computational time, so that a formation of virtual electrodes and trajectories of ions in the cathode were only simulated deficiently.

Based on this new knowledge and improving evaluation capabilities for a technology readiness level 3, the logic depicted in the dashed box in Figure 1.2 has been used to assess, develop and validate the chosen models with the existing experimental database. The direct simulation of the thrust mechanism assumes that the principle of plasma acceleration by plasma expansion is valid in this first assessment, which supports the thermal acceleration of ions. And complementary to that, a loss model was derived enabling the

estimation of energy left for the jet after reducing the input power by power lost due to ionization, excitation, Bremsstrahlung and particle-grid-collision losses [19], which is an assessment of efficiency. The indirect approach was also used for fusion energy gain research on IEC neutron sources [6]. In this way, a sufficient database to validate the code for Bremsstrahlung, ion - grid collisions and electron - grid collisions is available. Ionization and excitation losses were compared to NIST data and checked for physical plausibility. Charge exchange reactions may play a role in the losses calculation due to the level of operation pressures, but have not been implemented into the tool yet. The modeling of excitation processes also allows the identification of lines in the recorded spectra and a first assessment of particle temperatures and densities was obtained. These models can be validated against direct or indirect thrust measurements in future research activities, which will be necessary to advance the technology readiness level. The work shown in this thesis, enables a classification of TRL3. However, the work that is necessary to conclude this level, has not been finished yet.

2. Fundamentals of the IEC Principle and Configurations

Inertial Electrostatic Confinement (IEC) is an umbrella term for several concepts, using electrostatic forces or electromagnetic fields. The main concepts are the grid based design, the Periodically Oscillating Plasma Sphere (POPS) [20], the Polywell generator [21] and the Penning Trap [22]. The general principle uses electrostatic fields to trap particles, e.g. by an externally applied potential or virtual electrodes. Depending on the polarity, these can either be electrons or ions. The first device was thought up by Farnsworth and enhanced by Hirsch [23], which is considered the simplest design and which is used for this evaluation. This section explains the confinement principle as it has been investigated in neutron sources, elaborates on the existence of different particle species and their origins, observed operation modes with jet extractions and a hypothesis about their formation, as well as IEC design configurations.

2.1. Confinement Principle

The simplest setup of an IEC device consists of two spherical, concentric electrodes. The outer grid is used as the anode and the inner grid as the cathode. If the anode is the vacuum chamber, then the volume inside the vessel is flooded with a propellant (see Figure 2.1). Having a potential difference between the grids, a glow discharge ignites between the
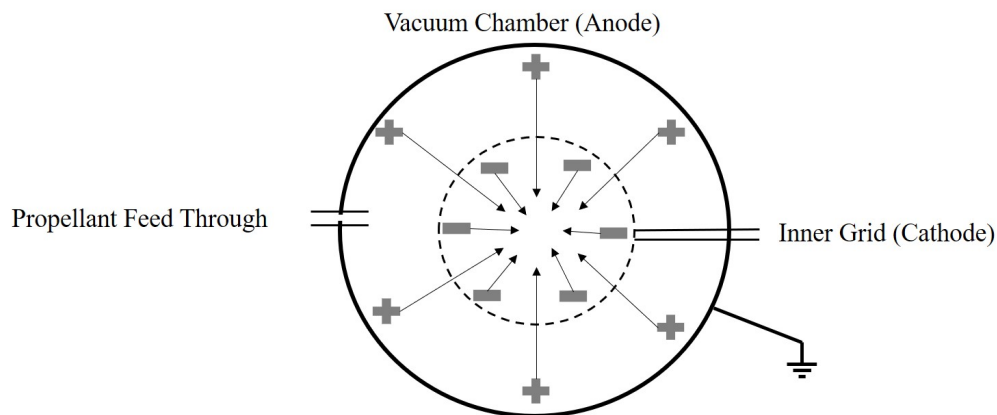
Figure 2.1.: Confinement principle schematic

electrodes creating charge carriers. The ions will be accelerated into the center of the negatively biased inner cathode grid; electrons are directed to the grounded anode. If the ion acceleration is sufficiently high, fusion processes might occur in case fusion-able propellants are used. Otherwise, the ions will be accelerated to the other side of the cathode where they leave the inside and get accelerated back again. In this way they tend to oscillate through the system until they are lost by collisions. For that reason, this confinement is dynamic. The confinement mechanism and fusion processes have been investigated extensively for neutron/plasma source applications [6, 11, 17, 24–30].

Thereby, different operation modes have been identified, which are the star mode relevant for fusion applications [14] (Figure 2.2a) and the jet modes (Figure 2.2b/c) for space propulsion applications [13].

(a) Star Mode (b) *tight* Jet Mode (c) *spray* Jet Mode
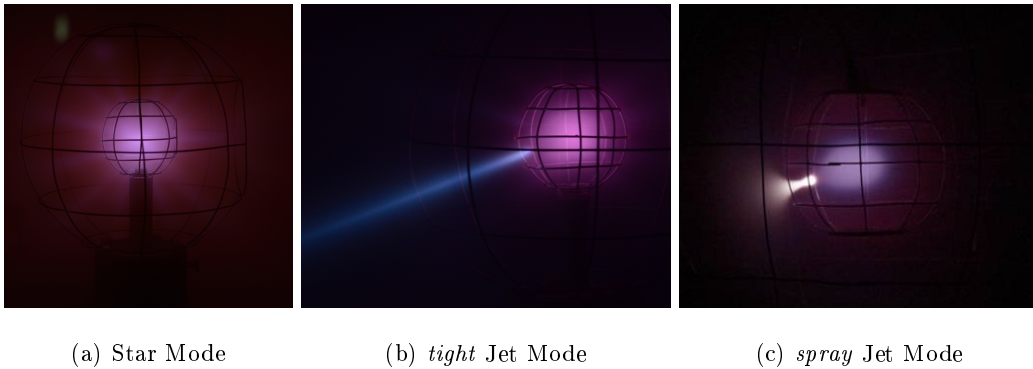
Figure 2.2.: Discharge Modes

2.1.1. Particle Species

Due to the dynamic behavior of this system, particles of different origins occur in the plasma confinement. The following list gives an overview and helps to understand the fundamentals of particle generation, but does not specify the particle sources within the jet when it leaves the grid system.

Ions

The applied plasma source for the experiments conducted in this thesis is a glow discharge, which means ions accelerated into the center are created in the inter-electrode space. These are called primary ions. During their travel into the cathode center, they encounter collisions with the cathode grid and other particles, get lost or oscillate through the cathode.

New ions may be generated by charge exchange collisions. A fast ion hits a slow neutral from the background gas and a slow ion and fast neutral is created. These ions are called secondary ions.

Electrons

Generally, at least two populations of electrons are distinguished in IEC devices depending on their origin of birth. Within a glow discharge, the so-called primary electrons are created. These flow from cathode to anode. It is proven that the inner electrode has a secondary source of electrons with a different energy distribution than the primary electrons [28,31]. However, it is not clear yet which physical phenomenon is responsible for secondary electron generation, hence different possibilities have to be considered here [18]:

Field Emission: The Fowler-Nordheim equation [32] covers this phenomenon, yielding an electron current density due to a tunneling effect:

$$j(E) = \frac{e^3 m^*}{8\pi h m W_e} E^2 \exp\left(-\frac{8\pi\sqrt{2mW_e^3}}{3ehE} \right) \tag{2.1}$$

Field emission occurs when a strong electric field E enables electrons bound in a solid to tunnel through the barrier and escape the solid. In Equation (2.1), e, m^*, m, W_e, and h represent the elementary charge, the effective mass, the particle's mass in the dielectric, the work function, and Planck's constant. With $W_e = 4.5eV = 7.2099 \cdot 10^{-19} J$ (stainless steel, [33]), $m^*/m = 8$, and $E = V/d$ for the configurations considered in this thesis ($V_{max} = 3500V$, $d_{min} = 0.05m$), this yields a vanishing current density j. The electric field has been derived from $E = V/d$ yielding electric fields which are significantly lower than what might be the case in reality. Therefore, this process still can play a role for the following reasons: The surface of the wires is not perfect, but rough. Due to the geometrical properties of the individual tiny material accumulations on the surface the effective electric field is increased so that the estimated field emission might become not vanishing low and even significant.

Thermionic Emission: The effect of thermionic emission is estimated at the cathode using the Richardson-Dushman equation [34]:

$$j(T) = A_R T^2 \exp\left(-\frac{W_e}{k_B T} \right) \tag{2.2}$$

Here, j is the emitted current density of the cathode grid (in consequence of the thermionic emission), T is the temperature, k_B is the Boltzmann constant, and A_R is the Richardson constant expressed as

$$A_R = \frac{4\pi m_e k_B^2 e}{h^3} = 1.20173 \cdot 10^6 \frac{A}{m^2 K^2}. \tag{2.3}$$

This value of A_R is an upper limit of the thermionic emission. If the cathode has a temperature of up to $T_c \approx 500K$, which might be the case for the experiments in this thesis, the resulting current density goes up to $j = 3.44 \cdot 10^{-12} A/m^2$. These values are assumed to be negligible.

Ion-Grid Collisions: A few positively-charged primary ions that are accelerated, might be able to unhinge electrons from the cathode grid surface by impact. Ion-grid collisions are a major loss mechanism. A part of the kinetic energy that is transferred to the grid is thermal energy and the other part can be accounted for erosion processes that remove material from the grid. As part of this process, there is also the possibility of electron emission by collisions [35].

Neutral - Neutral Collisions: Ionization processes due to reactive collisions between neutrals are expected to occur only after a charge exchange process leading to a high energy neutral (and a low energy ion). This source of electrons can not be considered as negligible, but the preceding process is still to be investigated to have a reliable assessment.

Neutral - Ion Collisions: The following assessment does not consider charge exchange reactions when a fast ion hits a slow neutral and a slow ion and fast neutral is created. Here, only electron emission by these collisions is considered as secondary source. Primary ions are accelerated towards the cathode. Hence, the maximum ion velocity is reached at r_c after a steady acceleration over a maximum distance of $d = r_a - r_c$. The expected ion energies are considered to be in the order of $\sim keV$. The cross sections taken from [36] were analyzed for the $Ar^+ - Ar$ case and data was found to be not sufficient for an evaluation [18].

Ion - Ion Collisions: Given the high number of ionization levels of argon, the reaction $Ar^+ + Ar^+ \rightarrow Ar^{2+} + Ar^+ + e$ as a potential electron source inside the cathode might play a role. However, reliable cross section data could not be identified. On the other hand,

the second ionization energy is significantly higher than the first one so that it is assumed that this process is negligible.

Neutrals

Depending on the plasma source, which will be discussed in the following section, the ionization efficiency might not be 100%, so that neutrals are existent from the propellant inflow. These are primary neutrals, which can encounter collisions with the other species as depicted above. Secondary neutrals can be created by charge-exchange reactions resulting into fast neutrals. These neutrals in turn can be a contributor to grid erosion.

2.2. IEC Designs

From the design point of view, it is necessary to classify the devices with respect to functional aspects. This is also relevant for a concept evaluation in terms of possible applications. Such a classification includes the following design-dependent considerations which are depicted in Figure 2.3:
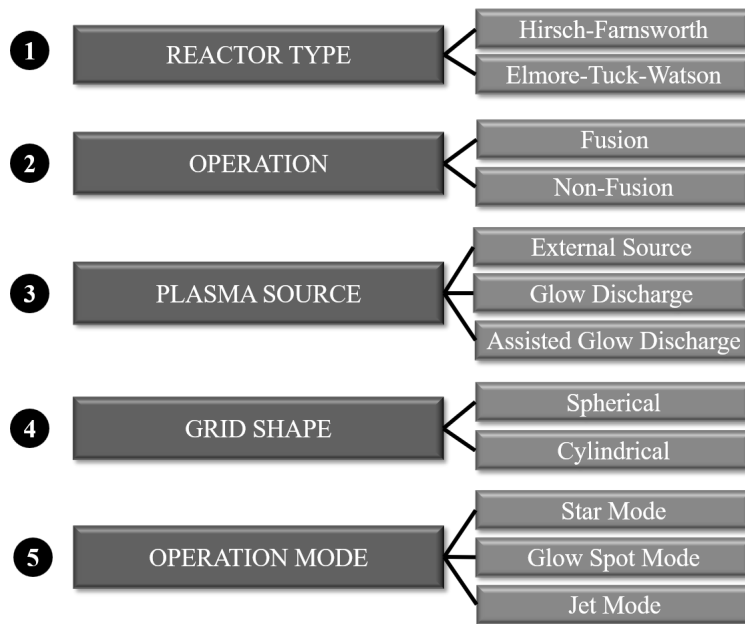
Figure 2.3.: Design parameters

The reactor type for the gridded IEC device is chosen between the principles of Hirsch-Farnsworth and Elmore-Tuck-Watson. The principle of the Farnsworth-Hirsch reactor has already been shown in section 2.1. The other concept of Elmore, Tuck and Watson has

mostly been studied theoretically [37] and hence will not be studied in detail herein. Then, by defining the propellant and input voltages, fusion and non-fusion mode can be chosen. Typical propellants for IECs in fusion mode (e.g. neutron sources) are hydrogen and helium isotopes, but also $p - 11B$ is one of the promising propellants. In non-fusion mode, any gaseous propellant can be used. Due to its low ionization energy, low reactiveness, good availability and affordability, argon is a candidate to favor. But it is one of the gases with higher molar mass and depending on the acceleration mechanism this can be an advantage or a disadvantage. Helium has a very low molar mass. Therefore, it is suitable for thermal acceleration, but has a very high first ionization stage. As alternative propellant, the residual atmosphere in a very low earth orbit is evident. However, nitrogen appears molecular, which means energy has to be spend for the dissociation and then for the ionization. Moreover, oxygen is a very reactive gas and aggravates the grid erosion. Hydrogen is the non-fusion alternative to $D - T$. If the acceleration is driven by a thermal acceleration, this propellant has a very high heat capacity. But it also has a molecular structure, nevertheless with a low ionization energy. Carbon dioxide is only interesting for Mars and Venus missions and has not been investigated yet. The carbon component could cause a layer of residuals on the grids and the erosion with oxygen will be an issue as well (Table 2.1).

Table 2.1.: IEC propellants

Fusion	Non-Fusion
$D - T$	Ar/Ne
$D -^3 He$	He
^3He -^3He	Air/N_2
$p -^{11} B$	H_2
	CO_2

The plasma source defines the ionization degree and is therefore also an important criterion for efficiency. There are different plasma sources used for the operation of an IEC device. Three categories are shown in Table 2.2. The glow discharge mechanism has been described in section 2.1. If an external source is used, as it is mostly done for fusion setups, electron and ion sources are decoupled and ions are injected from outside using guns. Electrons are only generated as secondary particles by ion-grid collisions or thermionic

effects. The pressure can be very low in these devices in order to ensure that beam-beam interaction is predominant, favoring the fusion rate per unit power. A combination of glow discharge and external source (e.g. ion gun) leads to higher ion densities in the system if relevant for the application. Electrons are generated by the glow discharge and e.g. heated filaments as primary particles and also as secondary particles as described in section 2.1.1.

Table 2.2.: IEC plasma sources

	Ion Source	Electron Source
Glow Discharge	Collisional ionization	Collisional ionization, secondary: ion-grid collisions
Assisted Glow Discharge	Collisional ionization, ion gun	Collisional ionization, secondary: ion-grid collisions, thermionic effect
External Source	Ion gun	Secondary: ion-grid collisions, thermionic effect

The grid shape to be chosen has to be a trade-off between symmetrical confinement and robust design. The spherical device ensures a better confinement of particles, but design, manufacturing and handling of the grids is more complex than for the cylindrical setup. The cylindrical shape is more robust and commonly used in commercial IEC fusion devices. The operation modes are explained in the following sections in more detail.

The geometric parameters (Figure 2.4) relevant for the following theories and experiments are design-dependent and setup specific.

- cathode radius r_C

- anode radius r_A

- grid gap d

- grid hole size g

- grid opening for jet extraction at anode $g_{o,A}$ and cathode $g_{o,C}$
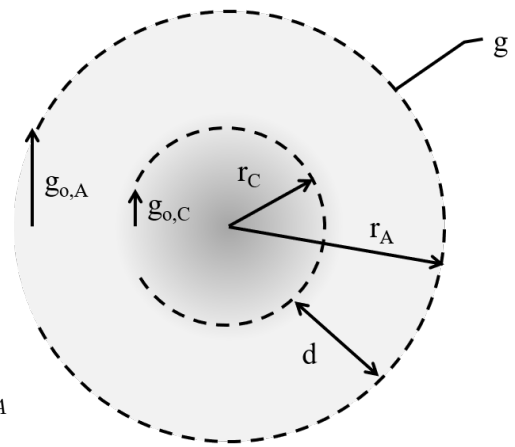
Figure 2.4.: Setup dimensions

The geometric transparency is a parameter between 0 and 1 that gives an assessment for the size of the cathode's open area used by the ions to circulate. The higher the geometric transparency of the grid, the lower the fraction of ions hitting the grid. This parameter is defined as follows [38]:

$$\eta_g = \frac{A_o}{A_g}. \tag{2.4}$$

Here, the open area of the grid surface is A_o and the grid surface area is A_g. In theory, the geometric transparency η_g is substituted by the effective transparency η_e, if focusing of the ions is good enough to reduce ions hitting the grid (e.g. by *microchanneling*). For the external source devices $\eta_e = \eta_g$ is valid while for glow discharge and assisted glow discharge the geometric transparency is related to the effective transparency by an empirical coefficient [24].

2.3. Operation Modes

Three different modes can be identified for a gridded IEC device. Depending on the design and homogeneity of the applied fields, they are manifested with certain discharge phenomena. The *star mode* (Figure 2.2 (a)) is not relevant for this thesis, but was seen during test phases. It appears at low propellant pressures and a symmetric confinement, which also necessitates a highly symmetric grid design. Detailed operation conditions for all modes will be described in later chapters. The *jet mode* occurs if a complete symmetry of the grid is not given, but one grid opening is larger than the others and certain operation conditions (*I*-*V*-characteristic) are commissioned. Here, the *spray* jet mode (Figure 2.2 (c)) and *tight* jet mode (Figure 2.2 (b)) are distinguished.

Jet Extraction Theory

Theories exist how this jet extraction could be established but none is yet adequately confirmed by measurements or simulations. The general consensus is that the jet extracted from the confinement is based on an electron-triggered mechanism. Looking at the potential field lines generated only by the externally applied field, the cathode inside is field-free in absence of particles (see Figure 2.5). The potential distribution inside of the cathode is mainly provoked by self-fields of the particles entering it. However, the grid structure also provokes that the applied field has impact on the inside of the cathode potential distribution at the grid openings. Although only ions are accelerated into the cathode center due
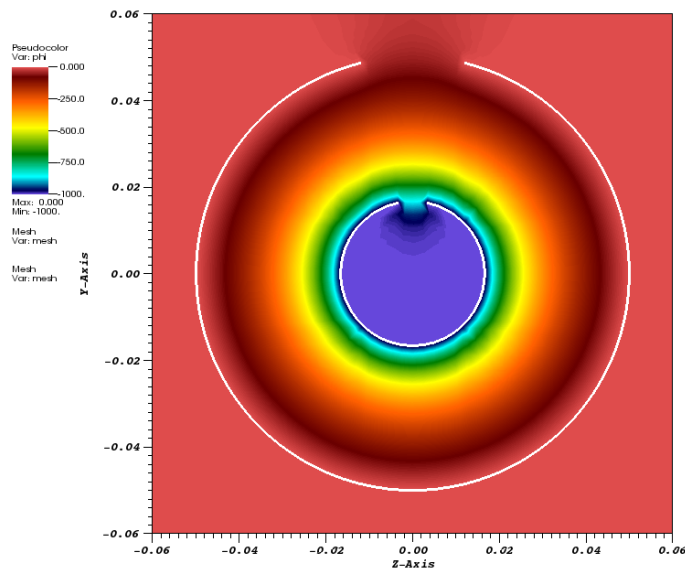
Figure 2.5.: Potential distribution due to external fields (simulation test case: $V_A = 0V$, $V_C = -1kV$, $d_A = 0.1m$, $d_C = 0.034m$, $g_{o,A} = 0.012m$, $g_{o,C} = 0.0033m$)

to the negative cathode potential, they in turn collide with the grid or with other particles and electrons are generated. These are trapped inside the cathode due to the high negative potential at the grid and virtual electrodes are created in the center which can be an anode due to existing electrons or cathodes due to the oscillating ions. If the grid openings are large, the less negative potential lines can reach trapped electrons. And if their thermal energy is high enough, these electrons are able to overcome the reduced grid potential at the opening to leave the cathode. It is also assumed that due to the curved shape of the field lines the electrons get accelerated on a constricted beam path, which works like a collective lens. This theory has been supported by simulations at IRS [18].

But so far that does not explain how highly energetic ions from the cathode center can leave the system via this jet *extraction*. In these aforementioned simulations with a Particle-In-Cell tool, an electron jet was reproduced. But ions moving through the cathode opening, was only indicated by formations of space charge sheaths which moved to the grid opening with ambipolar diffusion. The resulting assumption made here, is that the electrons drag ions with them, but electrons are usually much faster than ions and much lighter. If electrons leave the cathode center through one of the grid openings, the abundance of negative charge carriers between virtual anode and cathode grid leads to a strong electrostatic force that pushes ions at the edge of this virtual anode in the direction of the leaving electrons. As soon as enough the ions have left a balance establishes and the process stops until the

space charge shift is high enough to start the process again. An *extraction* of electrons and ions from the cathode is considered feasible with this mechanism.

Whether ambipolar diffusion can also explain an *acceleration* process to reach high I_{sp} as soon as they have left the cathode grid is still questionable. A proper empirical approach covering the responsible processes without resolving them in detail might base on plasma acceleration by area expansion, which was discussed by Manheimer [39] and has been adapted for IEC in section 4.2 [19].

3. Experimental Proof-of-Concept

This chapter describes the experiments conducted at IRS and results needed for qn understanding of the IEC technological functionality and hence for the evaluation of the technology readiness. Information about the used test facility and test setups is given, as well as test results and conclusions. The test logic that was used aimed primarily at identifying the different modes, assess and determine ignition and operation characteristics and scaling laws for the used IEC configurations. Additionally, the plasma has been investigated for species composition and jet transition.

3.1. Test Setup, Design Configurations, Diagnostics

For simplicity and comparison, these experiments were conducted with configurations and test setups that are easy to reproduce and enable comparability. Since the IEC technology and test environment was build up from scratch for this thesis at IRS, it was possible to ensure flexibility and deepen the understanding of influences from the test setup on the test results. Although not specifically mentioned in the explanations hereafter, critical parameters as chamber pressure and applied voltages and current readings were checked with validation and calibration procedures on a regular basis and unit to unit comparability of test equipment was verified.

3.1.1. Test Facility

The used vacuum facility is cylindrical, has a diameter of $1m$ and a length of $2.75m$ (see Figure 3.2). The chamber is equipped with a fully automatic three-stages pumping system providing an ultimate pressure of $10^{-4}mbar$. The operating pressure in the chamber p_{ch} is obtained by feeding gas into the chamber with a mass flow controller ($\dot{m}$ in Figure 3.2, Tylan FC2901 4S, S/N AE0310197) and is verified by a calibrated mass flow meter (Bronkhorst Mini Cori Flow M12P-AAD-22-0-S, S/N B13200221B). Chamber pressure p_{ch} is measured with a Pfeiffer Compact Full Range Gauge PKR 251 (S/N 44494524).

3.1.2. Grid Configurations

Four different grid setups were used for the discharge and scaling experiments that show the evolution of the design (Table 3.1). Since scaling of spherical electrodes does not permit changing the electrode surface and the electrode gap separately, ratios are introduced in order to allow a better comparison. The first configuration (C1) is composed of an anode with $0.3m$ in diameter and a cathode of $0.1m$ and was hung up with nylon wires in the chamber. A second configuration C2a is composed of a $0.15m$ anode and a $0.05m$ cathode. The anode of C2a can also be combined with a $0.035m$ cathode which is C2b (Figure 3.1). In this case, the grids are placed on a PEEK holder for the anode and an aluminum oxide holder for the cathode to ensure a fixed position. Grid setups C2a and b were manufactured in order to facilitate the manufacturing and therefore to increase the symmetry of the grids by reducing the size of the setup. Moreover, C2a was chosen to have the respective diameters in order to scale down the C1 setup by a factor of two and to keep the ratio of electrode gaps and electrode surfaces (anode/cathode). With the cathode of $0.035m$ the electrode gap in C2b can be varied, changing the ratio of electrode gaps and electrode surfaces. The number of longitude and latitude wires was maintained for all four configurations (5 latitude / 8 longitude). It also follows that the size of grid openings was reduced with C2a and C2b. Configuration C3a was the last evolution of the design. With this configuration, diameters and electrode gap were kept the same as for C2a, but one of the grid openings of each electrode was increased intentionally by adding another ring in the equator region. The anode opening was set with a $0.075m$ diameter from the beginning, but the cathode opening had to be increased from $0.020m$, $0.022m$ to $0.025m$ in diameter to enable a controlled jet extraction. For all setups, the grid wires have a diameter of $1mm$ and are made of stainless steel, spot welded into spherical grids.

3.1.3. Electrical Setup

The used power supply from FUG enables a voltage of max $-3.5kV$ and a current of $100mA$. Since the power unit only gives a rough display of voltage, a differential voltage probe (V) (Testec TT-SI 9110) is used to measure and scale down the voltage output transferring the data via a Datascan^{TM} system to a LabVIEW^{TM} acquisition program. Current (I) is measured by the voltage drop at a shunt implemented in the return line between anode and power supply (see Figure 3.2).

(a) C1 grids   (b) C2b and C2a grids   (c) C2a Setup
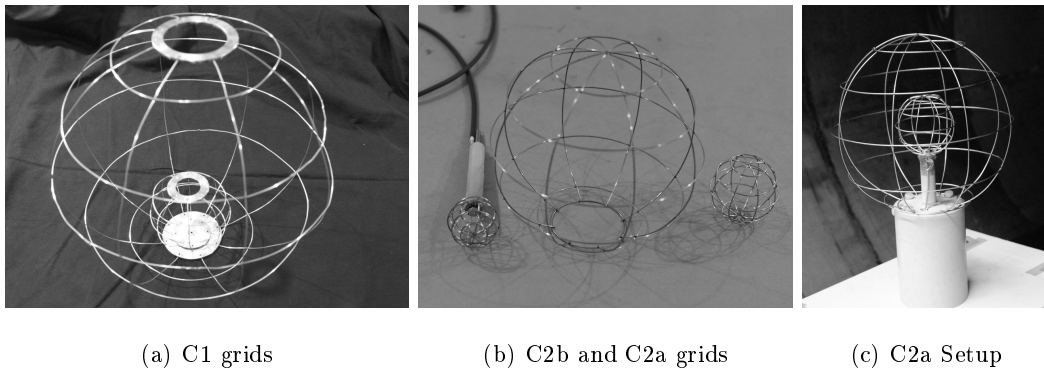
Figure 3.1.: Grid Setups
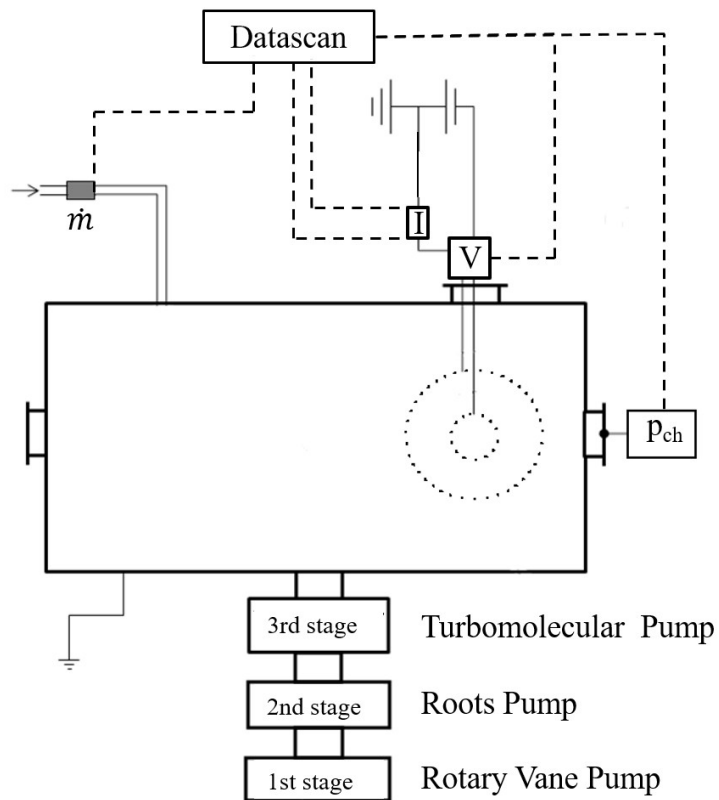
Figure 3.2.: Experimental Setup

Table 3.1.: Grid Configurations

	C1	C2a	C2b	C3a
Anode Diameter d_A	$0.3m$	$0.15m$	$0.15m$	$0.15m$
Cathode Diameter d_C	$0.1m$	$0.05m$	$0.035m$	$0.05m$
Electrode Gap d	$0.1m$	$0.05m$	$0.0575m$	$0.05m$
Gap Ratio (d_{C1}/d_{C2a}, d_{C2a}/d_{C3a})	2			
	0.87			
Ratio Electrode Surfaces (A_A/A_C)	9	9	18.31	9
Cathode Opening Radius $g_{o,C}$				$0.025m$
Anode Opening Radius $g_{o,A}$				$0.075m$
Geometric transparency η_g	0.98	0.84	0.78	0.84

3.1.4. Propellants

In general, IEC devices can be operated with any gaseous propellant. Argon was chosen, because it is easy to ionize and an inert gas, that is affordable and has a good availability compared to xenon. Helium was chosen because it is a very light weight gas similar to fusion propellants. Since the particle acceleration mechanism is not completely understood yet, also a thermal component can play a role where helium is beneficial due to its low mass and high heat capacity. Additionally, helium has a very high ionization energy compared to argon. Nitrogen was chosen due to its molecular appearance and it is a main component of air.

3.1.5. Plasma Diagnostics

The fundamentals of the plasma confinement are quite well known for fusion devices, but only scarce data is existent for the jet extraction. As depicted in section 2.1.1, the plasma species should be identified, which is feasible with optical emission spectroscopy. The stability and transition between the different jet modes is critical for continuous operation of these devices and can be assessed with a high-speed camera. The setups are discussed in the following paragraphs.

Optical Emission Spectroscopy

The plasma composition within the plasma confinement and plasma jet was investigated with optical emission spectroscopy (OES, Figure 3.3). An S2000 Ocean Optics spectrometer was used for these spectroscopic investigations. The spectrometer has a 2048-element linear CCD-array detector with fixed gratings and a $0.32nm$ FWHM optical resolution ($300 - 900nm$). Additionally, the light was focused by a collimator on the fiber optic entrance enabling a higher resolution. The collimator can be moved in $0.5 - 1cm$ steps in order to gather data at different positions in the cathode and the inter-electrode space. Starting from the center of the cathode, the system has been moved up to $7cm$ to the left and the right in horizontal direction in step sizes depending on the intensity of the discharge at the outer positions. A light source with a $0.6mm$ aperture was installed in the vacuum chamber ahead of the experiments in order to exactly determine the local position and the spatial dimension of the measurement volume. By moving the light source in $0.2mm$ increments in the axial direction, the axial intensity distribution was obtained. Fitting a Gaussian profile to these intensities yields an area of $7.2mm$ (axial) full width at half maximum. Wavelength calibration has been conducted with a mercury-argon lamp comparing lines to pixel numbers using a two-degree polynomial fit followed by an intensity calibration with an integrating sphere.

High-Speed Camera Measurements

For the high-speed videos of the transition between the jet modes and the stability investigations of both jet modes a high-speed camera CR5000x2 supplied by Optronis combined with a HiCATT 18 intensifier of Lambert Instruments were used. Aperture, frame rate, exposure time and intensifier gain are given in chapter 3.2.4 for the discussed data.

3.2. Test Results

This chapter shows all results of the experimental proof-of-concept. With the grid setups described in section 3.1.2, the ignition behavior with a glow discharge (see section 2.2) has been investigated and compared to fusion device data with glow discharge ignition [24]. After that, grid configurations were tested for operation conditions and scaling behavior. Plasma compositions in confinement and jet for the different propellants (see section 3.1.4) have been characterized and the transition between the operation modes has been
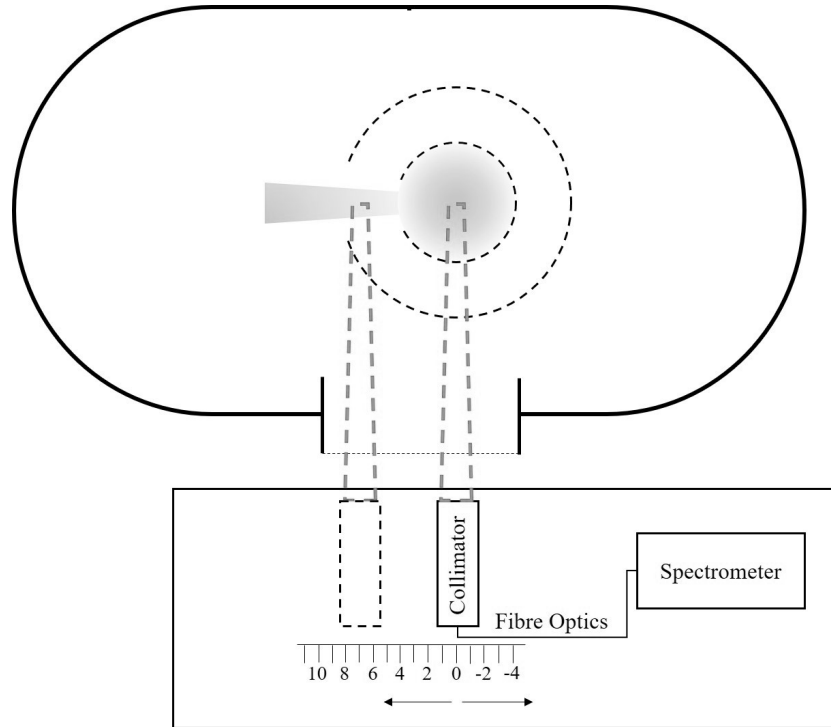
Figure 3.3.: Optical Emission Spectroscopy Setup

monitored with a high frequency camera in order to gain more information about the jet extraction mechanism.

3.2.1. Ignition: Glow Discharge

A distinct phenomenon for all setups is a pre-conditioning phase in which the IEC is very unstable and spark-like discharges occur on the grids. These occur whenever the grid was under air for some time, other residuals are left on the grids, or the surface roughness of the wires is high e.g., after manufacturing. After some time of initial operation so that the setup heats up, outgassing processes are initiated and the arcing has cleaned the surface, the IEC goes into stable operation.

Ignition mapping showed that the $I-V$-characteristic had no distinct ignition phenomena visible as it is the case for an arc discharge for example. The power supply gives current data with an accuracy of $0.1mA$ and the discharge is visible at $0.3mA$ characterized by a glow within the cathode. For that reason, the following ignition data was always recorded at an ignition current of $0.3mA$ in order to have a kind of breakdown criterion.

Figure 3.4 shows the breakdown characteristic of all configurations (see 3.1.2) with argon. It is similar to a conventional Paschen curve, although spherical permeable grids are used

here. In the range of $p \cdot d < 1Pa \cdot m$, there is almost no jet visible yet at $0.3mA$, just a glow in the center and sometimes a very faintly visible jet. At $p \cdot d > 2Pa \cdot m$ levels, the breakdown (dashed box) starts directly with the spray mode. This is considered a pressure dependence of the modes that will be discussed later in this chapter. A fitting curve has been derived from this data that shall allow predictions for argon ignitions. For all electrode configurations the ignition points seem to follow this function. However, the range above $p \cdot d > 5Pa \cdot m$ has not been tested due to pressure red lines of the pumping system. At $p \cdot d > 2Pa \cdot m$, the ignition voltage seems to increase again. But the data can only be an indicator, since the increase is within the accuracy of the measurement equipment. The fitting function has been derived to

$$V_D = 38 \cdot (p \cdot d)^{(-1.12)} + 231 \tag{3.5}$$

Figure 3.5 shows breakdown characteristics in nitrogen for configuration C2a, C2b and
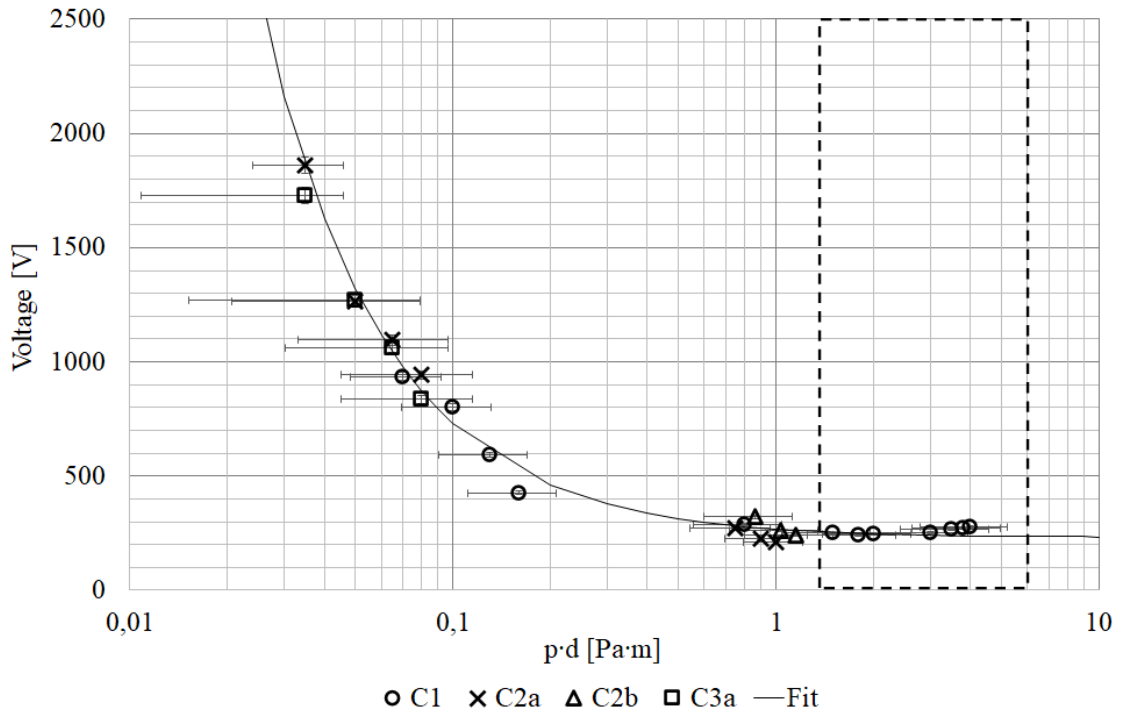
Figure 3.4.: Ignition conditions depending on the $p \cdot d$ for argon

C3a. Here again, the acquired data seems to follow a similar curve as in argon, which has been fitted to the data. Nevertheless, less data points are available for nitrogen which reduces reliability for $p \cdot d > 1Pa \cdot m$. No spray jet ignition has been observed for the available range of nitrogen and helium data points. Equation 3.6 shows the respective fit

function (p in Pa, d in m).

$$V_D = 204 \cdot (p \cdot d)^{(-0.6)} \qquad (3.6)$$

The data for helium visualized in Figure 3.6 has also been fitted to an ignition curve.
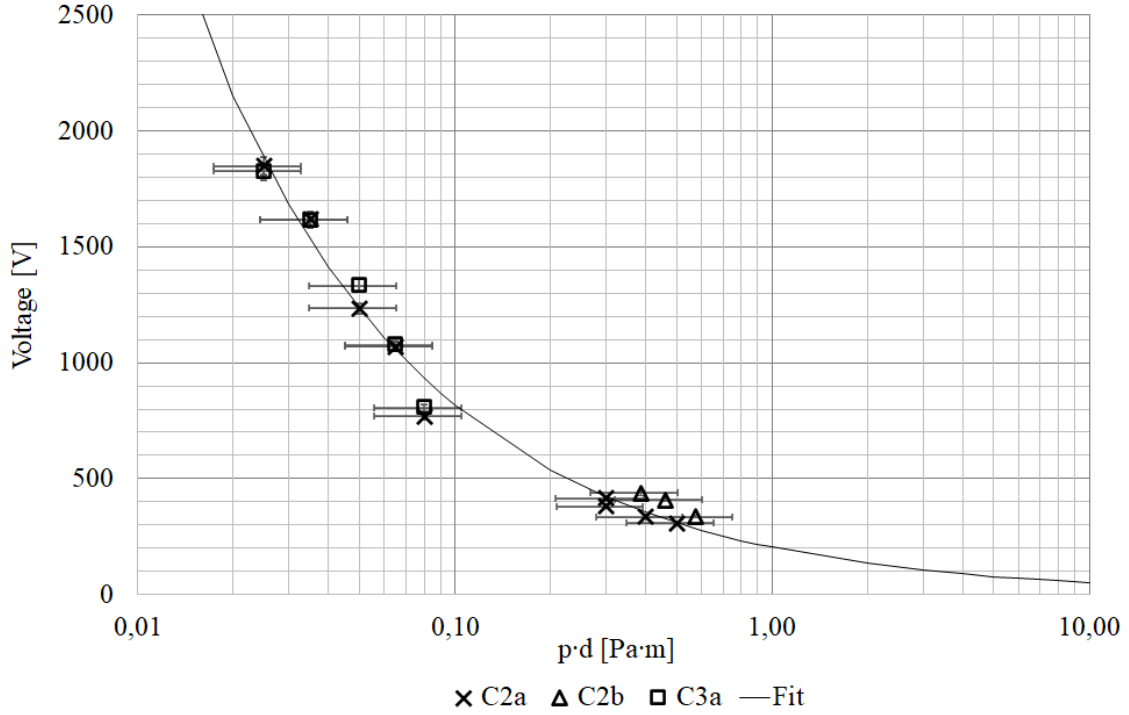
Figure 3.5.: Ignition conditions depending on the $p \cdot d$ for nitrogen

Due to its high ionization energy, it is less easy to ignite than the other propellants. Also here, the fitting curve for $p \cdot d > 0.6 Pa \cdot m$ shows less reliability at this point due to a lack of experimental data and the derived fit curve for the breakdown voltage can only be an indicator. The fit function is (p in Pa, d in m):

$$V_D = 398 \cdot (p \cdot d)^{(-0.49)}. \qquad (3.7)$$

This data has been compared to the work of the research group at the University of Illinois. It is also stated here, that the gridded IEC discharge works in a different range than the conventional discharges of planar, solid electrodes. For a fixed breakdown voltage the $p \cdot d$ is much higher for solid electrodes (planar and spherical) as for transparent electrodes [24]. This can be attributed to the ion flow through the electrodes. The shape of the breakdown characteristic in [24] is equal to the work shown here, however ignition voltages are higher by more than a factor of 5 for the same $p \cdot d$ and geometric grid transparencies (e.g. 84% for C2a). This could be linked to the fact that breakdown characteristics of
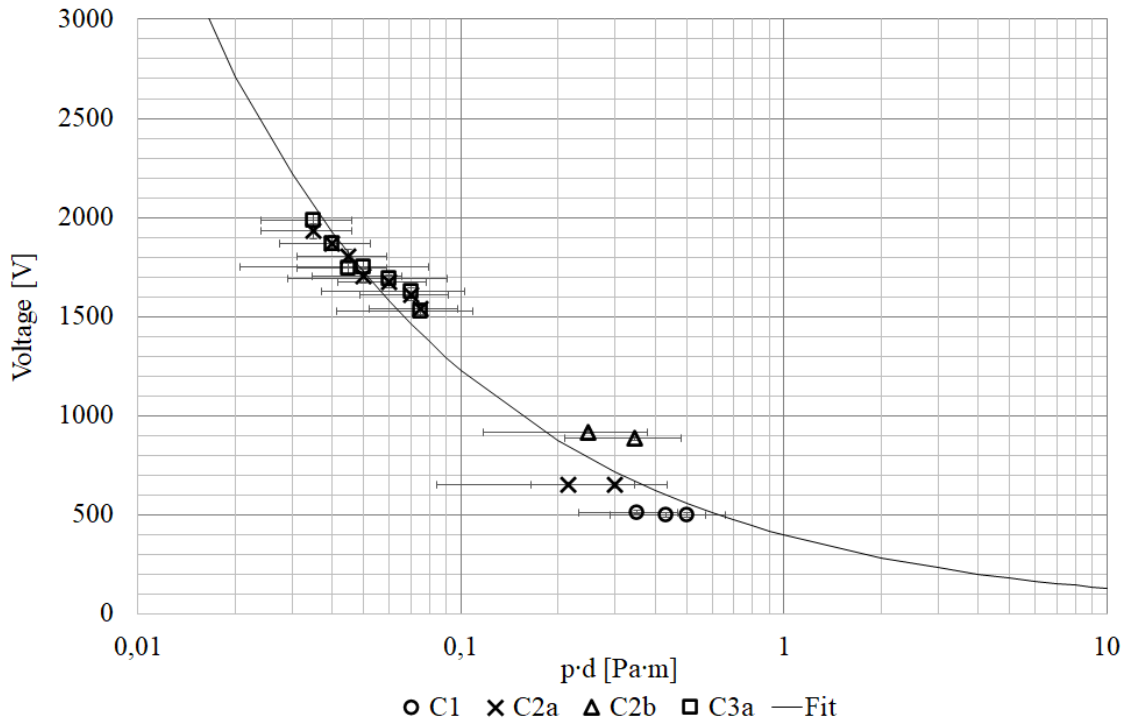
Figure 3.6.: Ignition conditions depending on the $p \cdot d$ for helium

hydrogen and deuterium have been presented, the breakdown current was not defined with $0.3 mA$ as in this thesis or that differing effective grid transparencies are influential. A theory supported by experimental data has been presented, that *microchannels* change the geometric transparency to an *effective* transparency which guides the ions into the cathode center and not on the grids, which will let the breakdown voltage increase [24].

3.2.2. Scaling Parameters of Grid Systems and Behavior of Discharge Parameters

The discharge behavior after ignition is highly dependent on several parameters. The discharge phenomena can be divided into *tight* and *spray* jet mode operation, which are the foci of this thesis. These phenomena can be characterized by discharge current and discharge voltage ($I - V$-characteristic) and these parameters are dependent on factors such as configuration (electrode gap / electrode surface), propellant and pressure level. All of these factors have already been discussed for the ignition behavior in the foregoing section. The IEC device can be operated in current or voltage control.

Pressure Dependency

Figure 3.7 shows $I - V$-characteristics for C2a with argon at different pressure levels. The C2a configuration had no enlarged grid opening in anode and cathode for a directed jet extraction, but an asymmetry in one of the grid holes that enabled a jet extraction (see Figure 2.2 for *tight* and *spray* jet mode). Here, the different modes are clearly identified by the $I - V$-characteristic when the pressure level is varied. At higher pressure levels
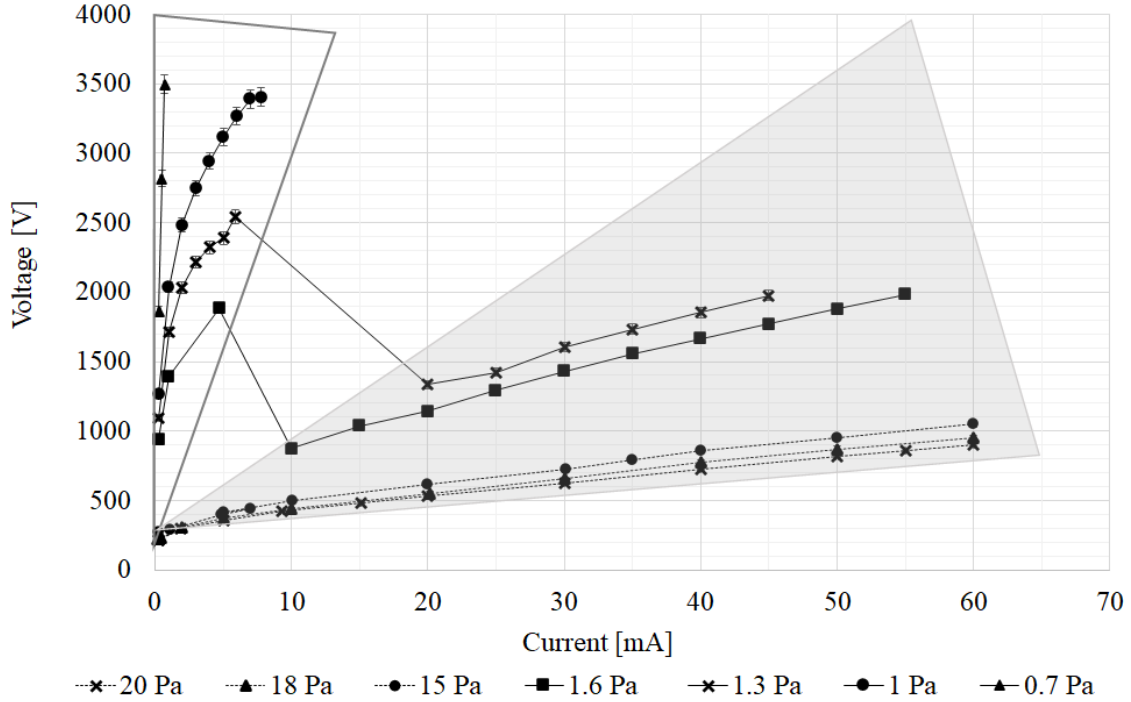
Figure 3.7.: Discharge parameters for *tight* and *spray* jet mode for different pressure level in Ar (C2a)

$p_{ch} \geq 15Pa$, the IEC is operated in *spray* jet mode (dotted lines, grey highlighted region in Figure 3.7). After ignition the *spray* is visible immediately. At lower levels, the IEC can be operated in the *tight* jet mode (transparent box in Figure 3.7) until a pressure specific operation condition is reached and the IEC jumps from a stable *tight* jet into a stable *spray* jet mode as visible for pressure level $1.6Pa$ and $1.3Pa$. For level $1Pa$ and $0.7Pa$, this transition has not been reached due to the voltage limitation of the power supply at $3.5kV$. The transition is investigated and analyzed in section 3.2.4. However, from the performance mapping, it was derived that there is an operational range between *tight* and *spray* mode where the IEC cannot be operated in a stable condition. This behavior occurs for helium and nitrogen as well and is therefore not propellant dependent. In further

investigations, the IECs were only operated in pressure regimes where at least the *tight* mode or better both jet modes are visible (first *tight*, then *spray*).

A directed jet extraction, such as with configuration C3a, shows the same behavior depicted in Figure 3.8 to 3.10. Figure 3.9 shows in this pressure range, that no *spray* jet mode was observed with the available power source working with helium as propellant. Tests with nitrogen show the same distinct $I - V$-characteristics with transitions in the same pressure range as with argon, which confirms that the jet modes can be clearly characterized and the $I - V$-characteristic changes with pressure. The dotted line for pressure level $1.3Pa$ in Figure 3.10 shows a transition, which has not been stable. The *spray* jet mode has been reached but could not be maintained. The mode was jumping back and forth. An explanation is given in the next section. The IEC devices were operated only up to $60mA$, even though the power limit might not have been reached. Configuration C3a showed a high thermal load at the extraction region of the cathode grid. As stated in section 2.1.1 thermionic emission can be an additional source for secondary electrons. For comparison, the power level has been kept below a visible glowing of the grids (see Figure 3.11) to avoid this effect.

Figure 3.8.: Discharge parameters for *tight* and *spray* jet mode for different pressure level in Ar (C3a)

Figure 3.9.: Discharge parameters for *tight* jet mode for different pressure level in He (C3a)

Figure 3.10.: Discharge parameters for *tight* and *spray* jet mode for different pressure level in N (C3a)
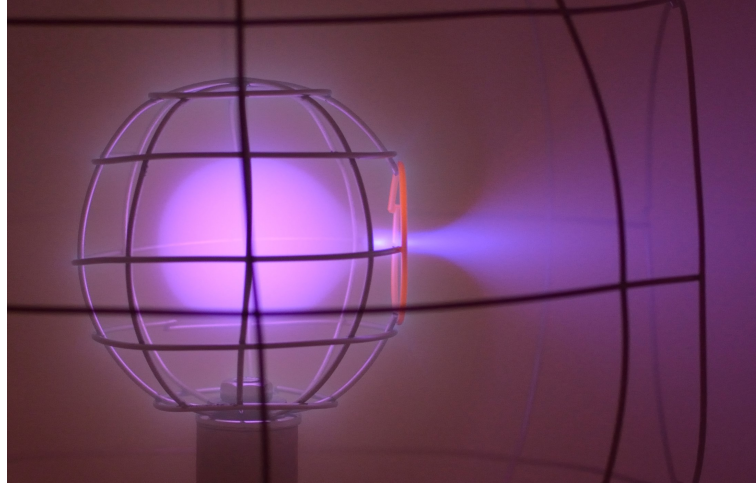
Figure 3.11.: Glow at the cathode grid exit (C3a)

Configuration Dependency

As discussed above, there is a change in transition behavior between C2a and C3a that has been observed for argon in the foregoing section. This change is considered to be related to the enlarged grid opening in C3a that induces a larger instability into the IEC confinement/extraction. This effect of different designs observed in test data for argon, depicted in Figure 3.7 and 3.8, is characterized by the fact that the transition occurs at lower voltages and even lower pressures for C3a. The transition at $1.3Pa$ occurs already at $2000V$ instead of $2500V$ and the transition at $1Pa$ can be observed with C3a which is not feasible with C2a due to the voltage limit of the test power supply which is reached. The data for nitrogen has been checked as well in order to eliminate a propellant dependency. In Figure 3.10 has been shown that there was an instable behavior at a pressure of $1.3Pa$. In operation with configuration C3a the transition of *tight* to *spray* mode was initiated but could not be maintained. As soon as the *spray* mode was observed, the mode jumped back into *tight* jet mode, which happened back and forth again. In C2a (see Figure 3.12), there was no transition due to the voltage limit as it was the case for argon. For helium this effect was not observed (see Figure 3.9), since for both configurations the power limit was reached before the transition region could be reached. The $I - V$-characteristic matches well between C2a and C3a.

Another $I - V$-characteristic dependency that was investigated, is the influence of different electrode gaps and electrode surfaces on the discharge parameters. Configurations C1, C2a and C2b were designed for that purpose and tested. The comparisons are done
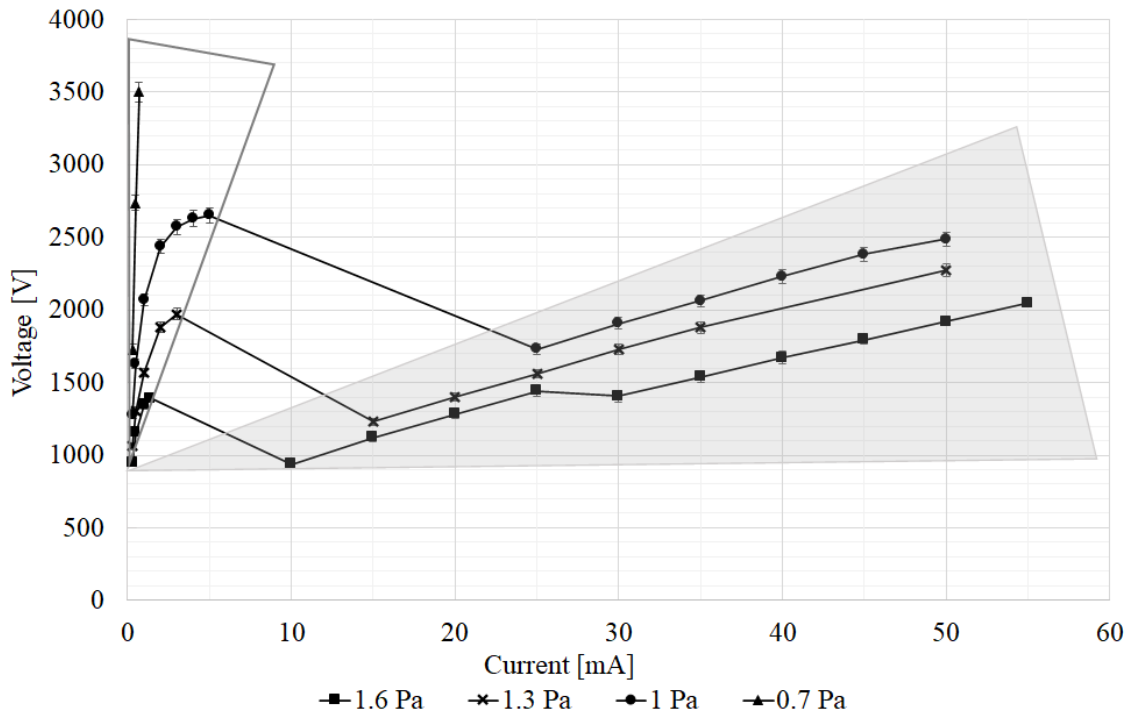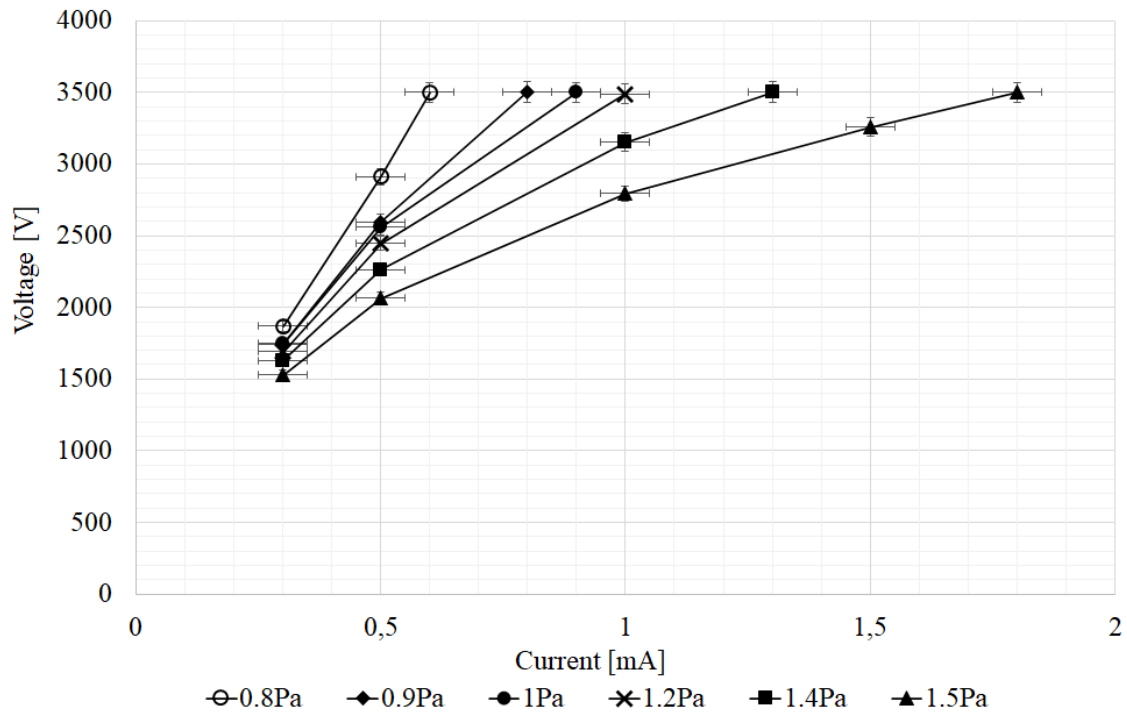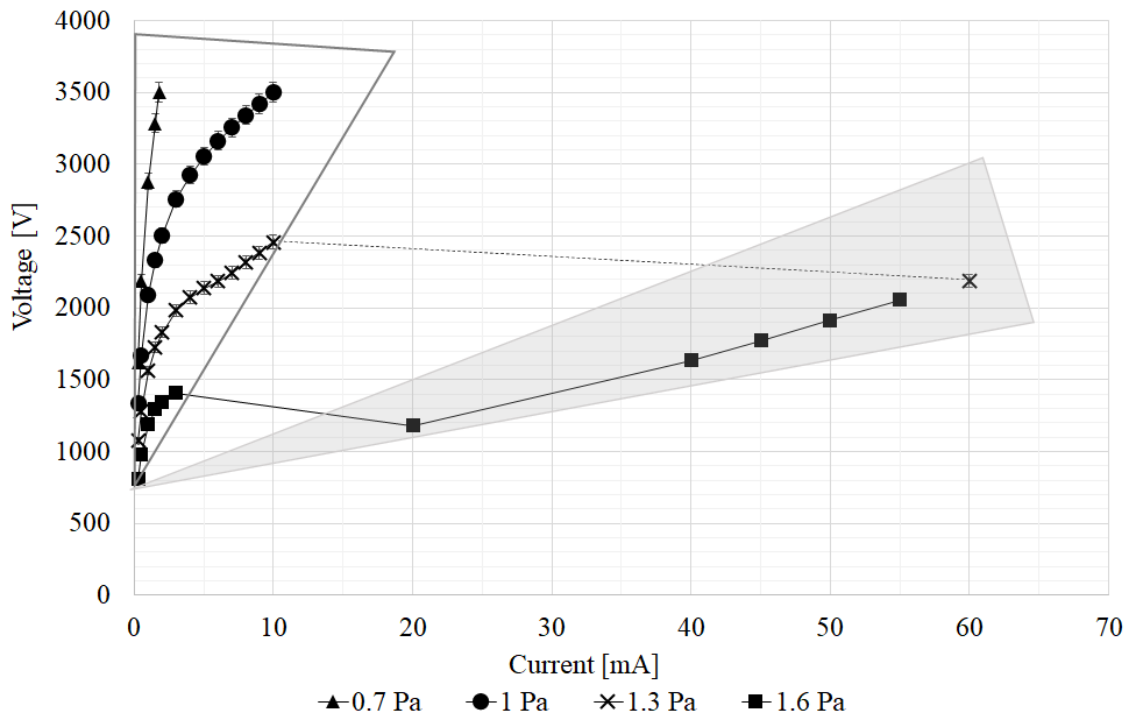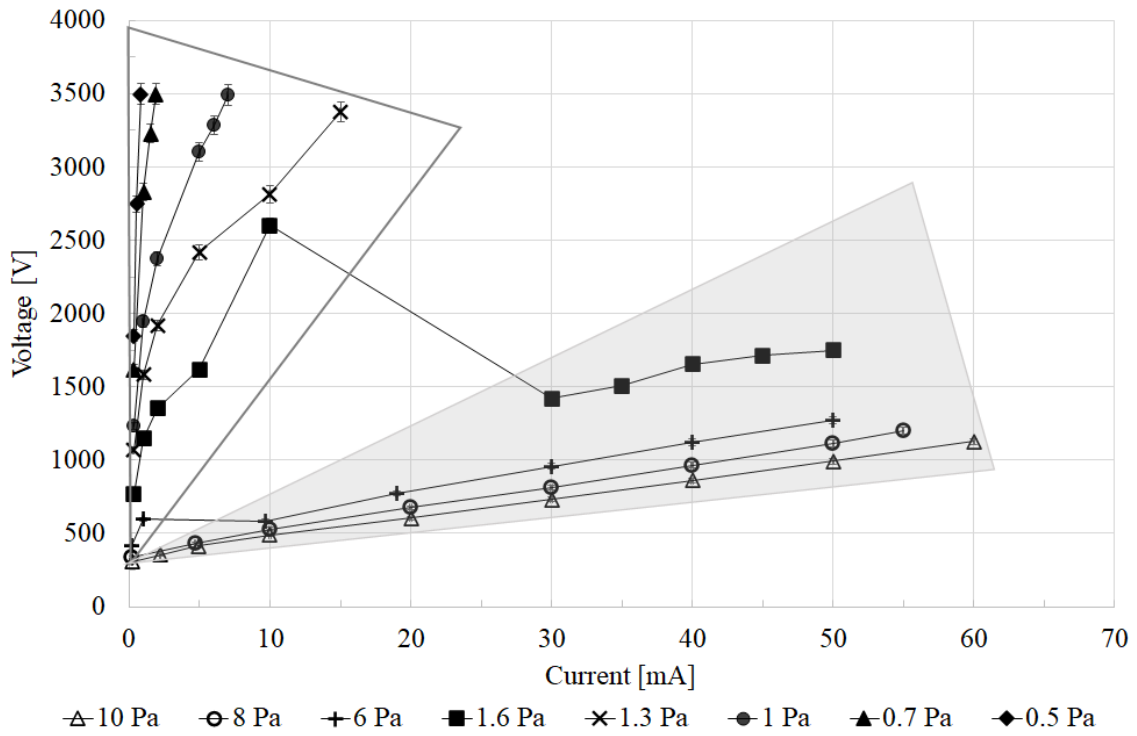
Figure 3.12.: Discharge parameters for *tight* and *spray* jet mode for different pressure level in N (C2a)
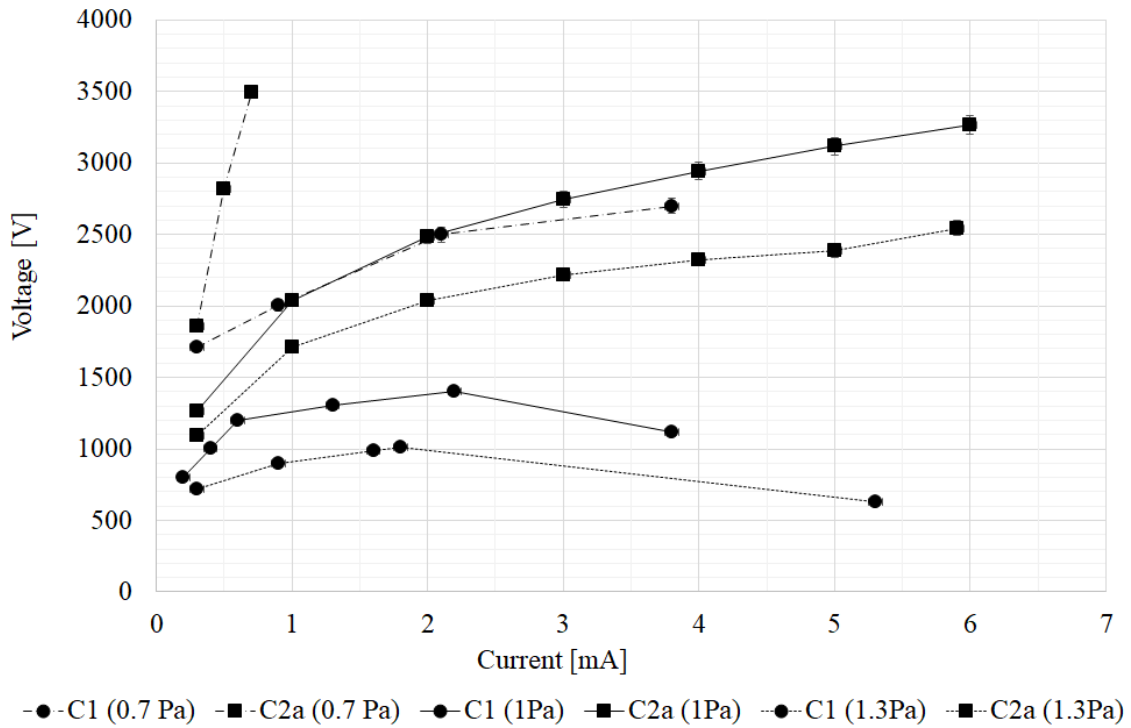
Figure 3.13.: Discharge parameters of C1 and C2a for argon $p_{ch} \leq 1.3Pa$
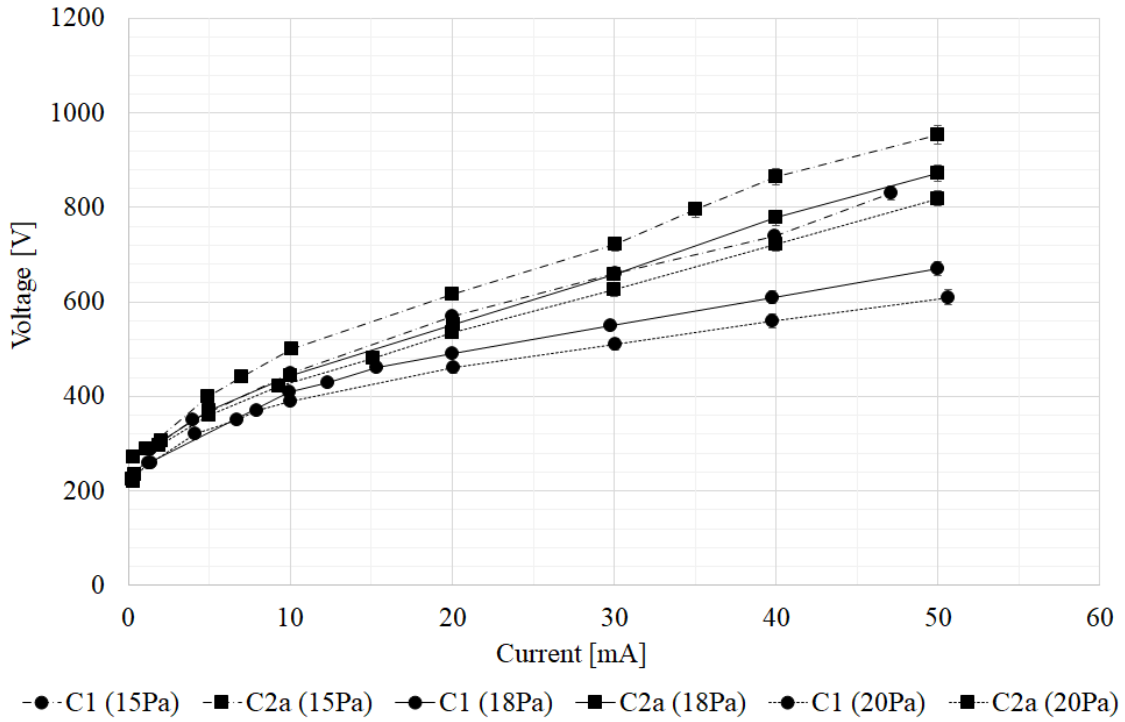
Figure 3.14.: Discharge parameters of C1 and C2a for argon $p_{ch} \geq 15Pa$
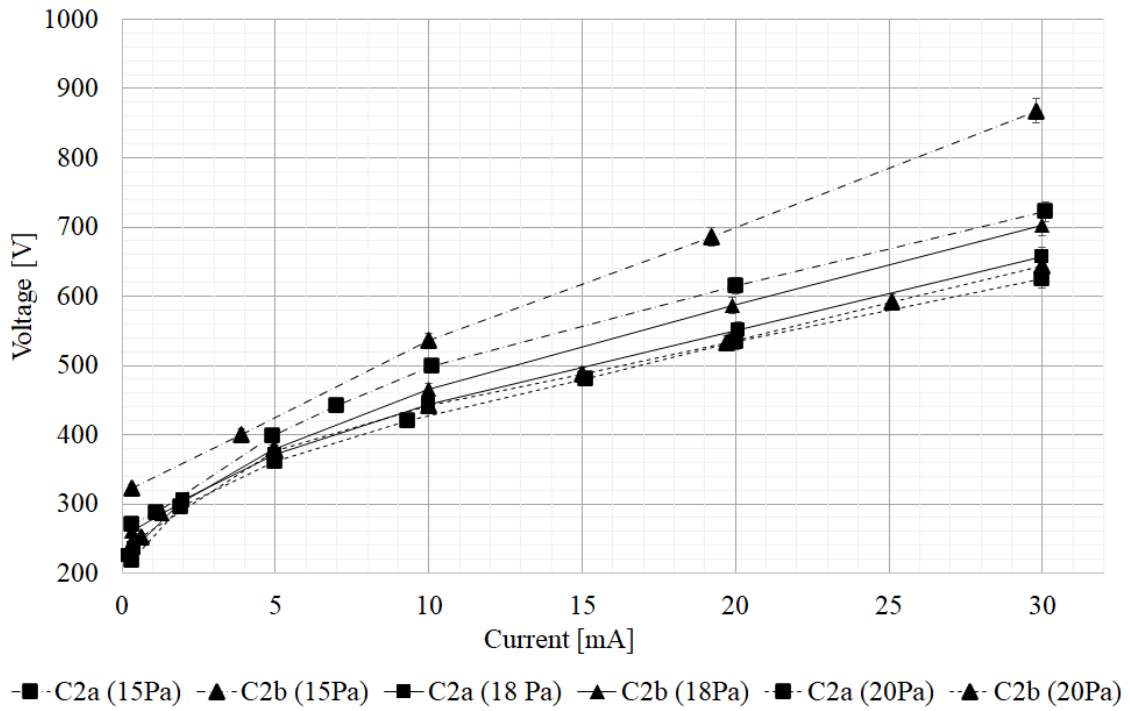
Figure 3.15.: Discharge parameters of C2a and C2b in argon $p_{ch} \geq 15Pa$

for argon and supported with data of nitrogen or helium.
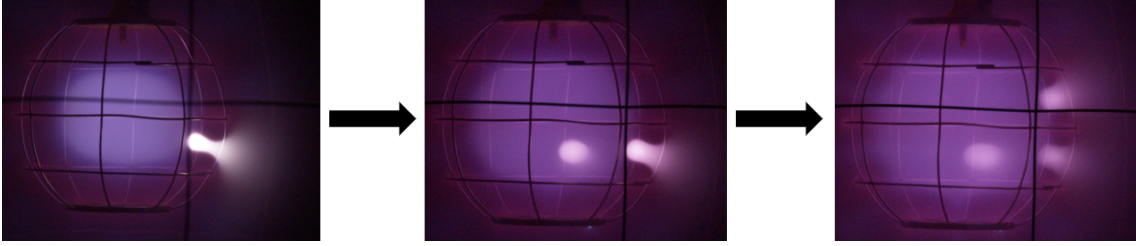
Figure 3.16.: C1 operated with several jets

Firstly, configuration C1 and C2a were compared. The intention of this configuration pairing was to halve the electrode gap and to keep the ratio of electrode surfaces constant. Figure 3.13 shows data for the low-pressure range $p_{ch} \leq 1.3Pa$. The $I-V$-characteristics are very different, which can be related to the fact that the C1 configuration was always ignited into spray mode, although pressure and discharge currents were very low. The fact that C1 only operates with *spray* mode can be attributed to the increased grid hole size of C1 compared to C2a (the same number of latitude and longitude wires and wire thickness for both configurations). The decrease in discharge voltage with increasing discharge current is here not related to the transition from *tight* to *spray* jet mode, but to the occurrence of more than one *spray* jet (see Figure 3.16). Configuration C2a has been operated only in *tight* jet mode at the same pressure levels and power limits. One would expect that with decreased electrode gap such as with C2a, the discharge voltage would decrease with scaling from C1 to C2a for the same pressure level. However, the *spray* jets in C1 seem to allow a better conductivity between the grids. This conductivity of the *spray* mode has been further investigated in section 3.2.4. If both configurations, operated in *spray* mode, are compared at pressure levels $p_{ch} = 15Pa$ to $20Pa$, it is evident that with increasing pressure the $I-V$-characteristics of C1 and C2a move further apart from each other (see Figure 3.14). Here again, this can be related to the fact that C1 develops more than one *spray* jet while C2a keeps only one during the operational range that is visible and conductivity between the grids is not as good as with several jets (see Figure 3.16).

Comparison of C2a and C2b (see Figure 3.15) allowed scaling of the electrode gab and also cathode surface. Operating both configurations at pressure levels $p_{ch} = 15Pa$ to $20Pa$ was keeping only one *spray* jet the whole time. Here, with increasing pressure the discharge curves are getting closer to each other, which implies that with increasing pressure the difference in electrode gaps of $0.75cm$ becomes negligible in this range. This

behavior is also visible when operating these configurations in *spray* mode with nitrogen.

Propellant Dependency

Until now, only breakdown and discharge conditions were discussed for electrode design and pressure levels. But the $I-V$-characteristic is not only depending on these parameters, but also on the used propellant. Figure 3.17 shows discharge data for argon, helium and nitrogen using configuration C3a for all three gases and the same pressure levels. The curve for argon shows the lowest voltages necessary to draw equivalent currents. This is due to the fact that argon is very easy to ionize and sufficient charge carriers are available already at lower voltages. Molecular nitrogen has a similar first ionization energy as argon, but occurs first molecular. Ionized nitrogen will appear as N^+ (see section 3.2.3) so that a fraction of the energy input will also be used for the dissociation process before ionization to N^+ will occur. This explains the higher voltages necessary for the same discharge currents
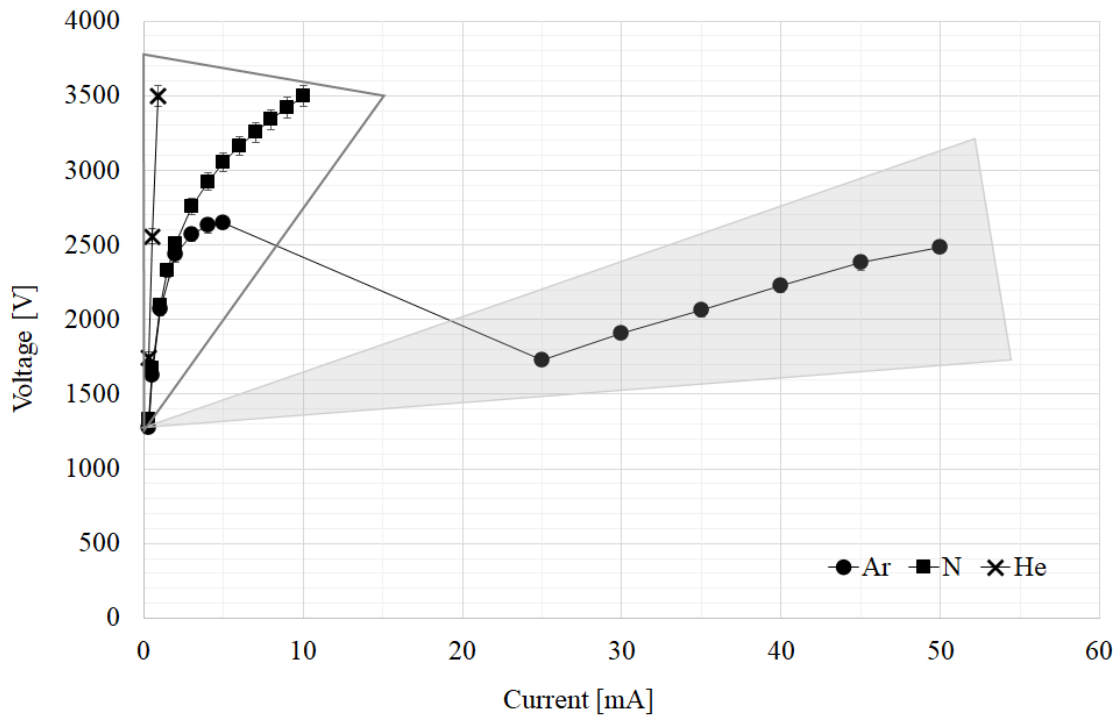
Figure 3.17.: Discharge parameters for C3a with argon, helium and nitrogen at $1Pa$

(first ionization energy nitrogen $14.53eV$ and argon $15.75eV$). Helium has the highest first ionization stage of all used propellants. Hence, it is explicable that only very low currents can be achieved with the available maximum voltage of $-3.5kV$. The transition between both modes occurs for argon at lower power levels than for nitrogen and helium.

3.2.3. Confinement and Jet: Plasma composition

Plasma diagnostics are necessary in order to support or refute the plasma extraction theory for a plasma confinement of section 2.1 and section 2.3. Typical propellants for neutron sources are deuterium and tritium [29]. For other propellants such as argon, helium or nitrogen (air) used in IEC devices only scarce data is available. As indicated, the main plasma component within the cathode are neutrals from background gas. The ionization degree through the glow discharge in the inter-electrode space is not the same as in the cathode center due to collisions that ions encounter. Therefore, the higher the background pressure the lower the detectable fraction of ions in the confinement plasma for the same discharge current. The spectroscopic investigations were performed for argon, helium and nitrogen. For helium, only neutral species could be observed within the plasma confinement at operation conditions with $10 - 20W$ (Figure 3.18). These power limits are defined by the test power supply.
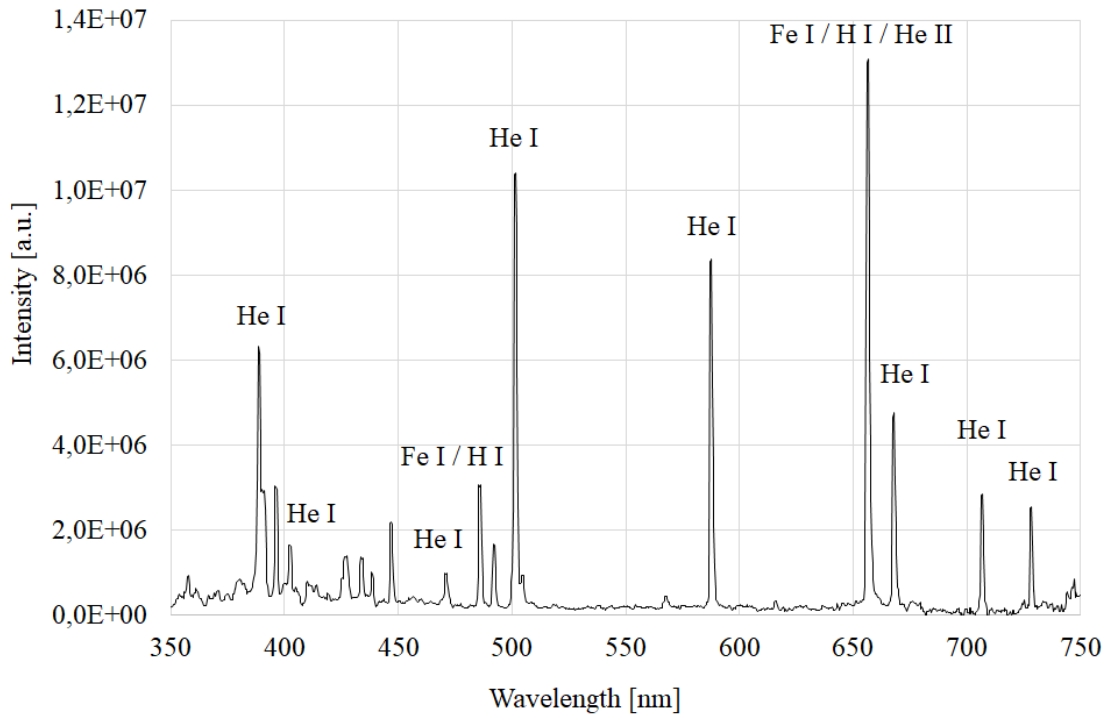
Figure 3.18.: Spectra of helium discharge at cathode center position (C2a, $V_D = 1697V, I_D = 10mA, p_{ch} = 4.3Pa$)

Since the intensities of helium plasmas in IEC sources are very low at these power levels, further investigations of the beam plasma were conducted in an argon and a nitrogen plasma. The operation conditions that were tested are shown in Table 3.2. For these

experiments, it was not feasible to separate pressure and propellant dependencies for direct comparison. Looking at Figure 3.8 and 3.10, these are the adequate operation points to be used for OES examinations. For argon, the transition at $1Pa$ occurs at $5.5mA$ so that the *tight* jet is bright enough to measure reliable intensities. Below $1Pa$, the transition does not occur and above $1Pa$ at too low discharge currents. For nitrogen, $1Pa$ is not suitable since no transition can be provoked with the available power, $1.3Pa$ is not stable, so $1.6Pa$ has been used as pressure level. Having different pressure levels means that pressure dependencies cannot be excluded. These experiments were conducted with configuration C3a.

Propellant, Mode	Pressure	Current	Voltage
Argon, *tight*	$1Pa$	$5mA$	$2710V$
Argon, *spray*	$1Pa$	$50mA$	$2487V$
Nitrogen, *tight*	$1.6Pa$	$5mA$	$1737V$
Nitrogen, *spray*	$1.6Pa$	$50mA$	$1990V$

Table 3.2.: Operation Conditions for OES

The spectra have been recorded at several positions to get data of the confinement plasma at $1.5cm$ far away from the center, the plasma at the cathode exit plane in the jet at $2.5cm$ and the plasma in the jet in the inter-electrode space at $4cm$. All spectra have been recorded at $3000ms$ exposure time. In conclusion, the following data can be compared in terms of species composition:

- different measurement position for one mode and propellant

- *tight* to *spray* for the same propellant

The spectra recorded in argon for the *tight* jet mode are shown in Figures 3.19 and 3.20. These spectra show mostly lines of argon ions in the wavelength range of $400 - 480nm$ and neutral argon in the range of $690 - 850nm$. Comparison of the positions in confinement plasma and jet plasma shows that from position 1.5 to $2.5cm$ intensities of Ar^+ (Ar II) and neutral Ar (Ar I) decrease. Also, from position 2.5 to $4cm$ a decrease is detected. The ratio of decreasing intensities for argon ions and neutral argon at the different positions indicates that there is no particular change of species composition in certain plasma regions, only excitation is reduced. For argon in *spray* mode intensities are generally higher (see Figure
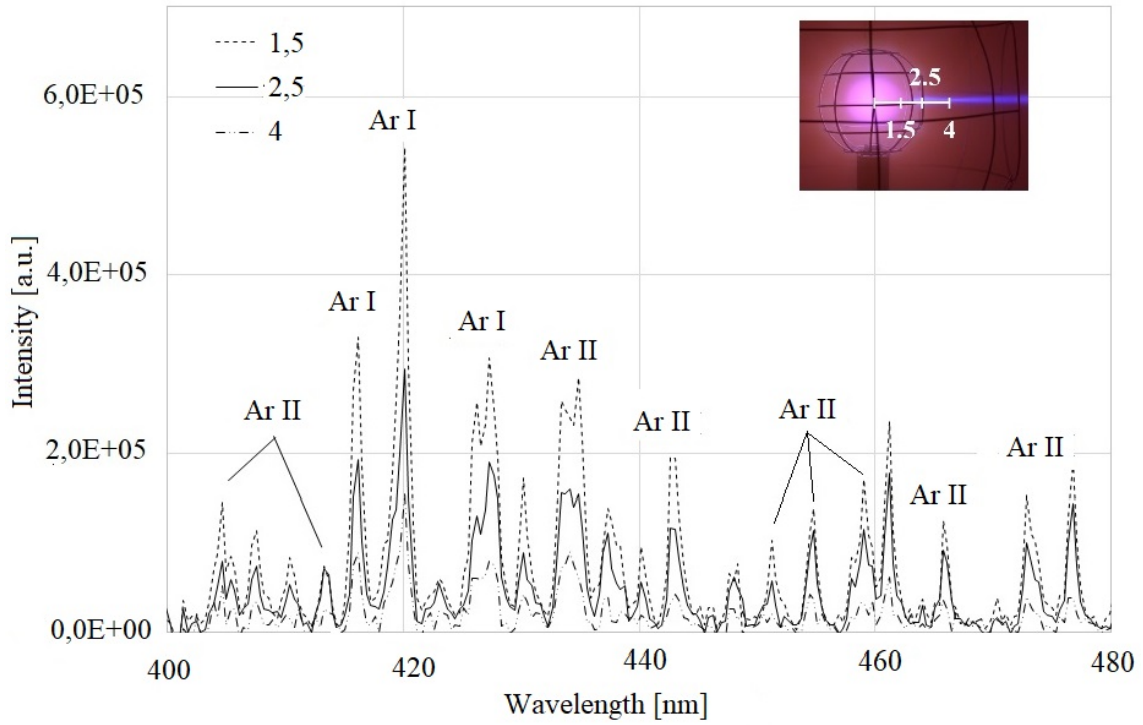
Figure 3.19.: Spectra of argon discharge at position 1.5, 2.5 and $4cm$ in the wavelength range $400 - 480nm$ (*tight* jet, $V_D = 2710V, I_D = 5mA, p_{ch} = 1Pa$)
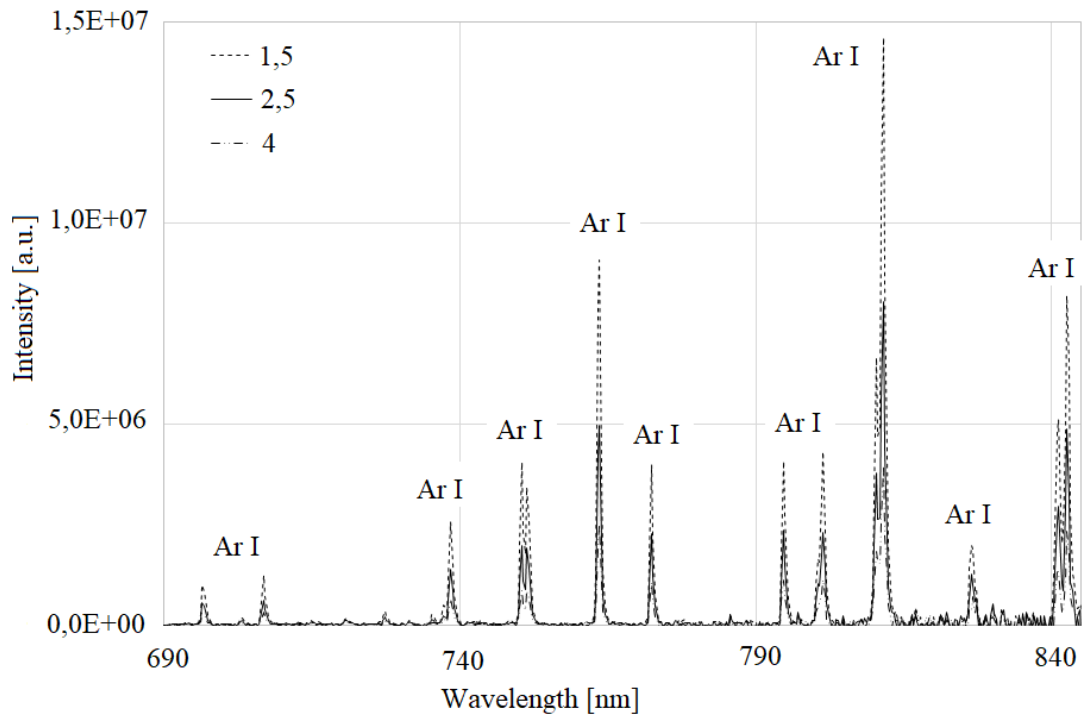
Figure 3.20.: Spectra of argon discharge at position 1.5, 2.5 and $4cm$ in the wavelength range $690 - 850nm$ (*tight* jet, $V_D = 2710V, I_D = 5mA, p_{ch} = 1Pa$)
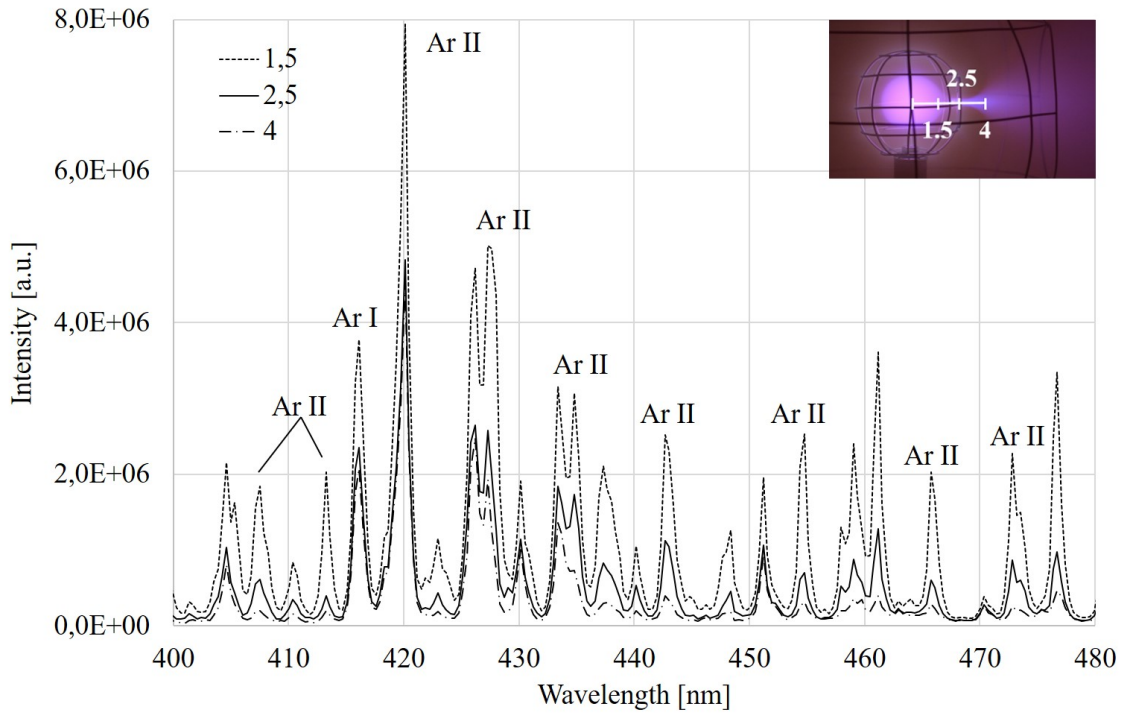
Figure 3.21.: Spectra of argon discharge at position 1.5, 2.5 and $4cm$ in the wavelength range $400 - 480nm$ ($spray$ jet, $V_D = 2487V, I_D = 50mA, p_{ch} = 1Pa$)
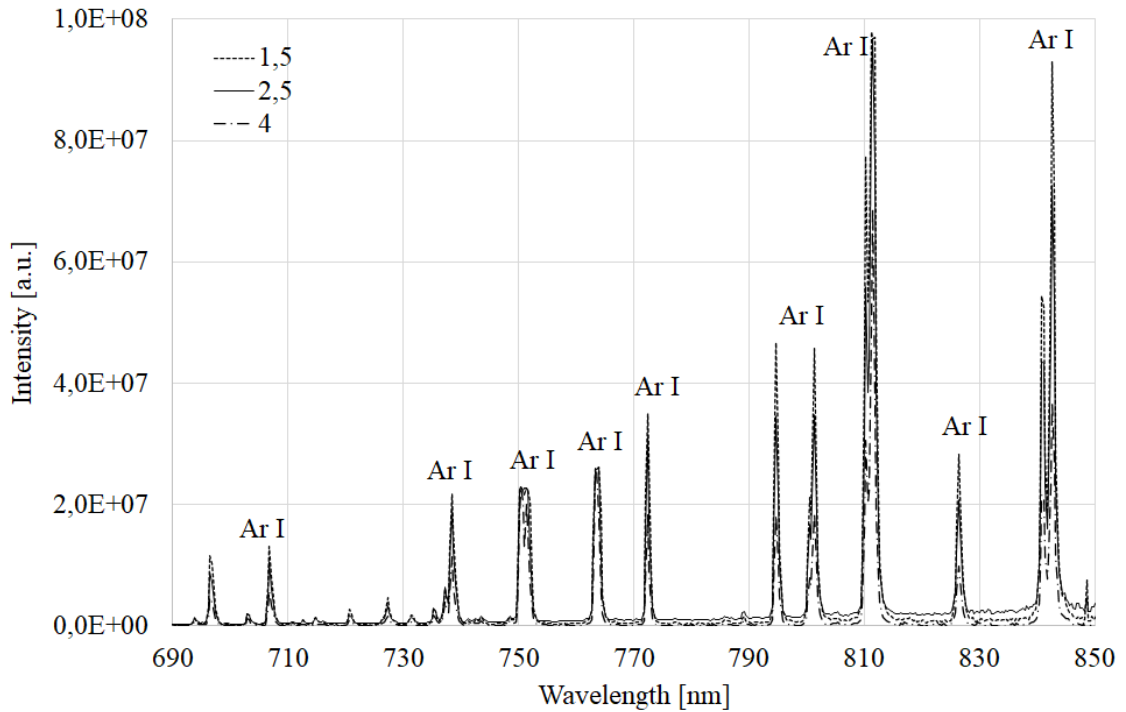
Figure 3.22.: Spectra of argon discharge at position 1.5, 2.5 and $4cm$ in the wavelength range $690 - 850nm$ ($spray$ jet, $V_D = 2487V, I_D = 50mA, p_{ch} = 1Pa$)

3.21 and 3.22). Comparing the position $1.5cm$ with position 2.5 and $4cm$, the portion of ions is much higher at the position in the confinement and does not change much between cathode exit and inter-electrode space, while neutral argon reduces continuously between measurement positions from 1.5 to $4cm$.

Figures 3.23 and 3.24 show nitrogen spectra recorded in *tight* jet mode. These spectra show strong lines of ionized nitrogen (N II) and nitrogen atoms (N I) within $350 - 500nm$ and molecular bands within $550 - 800nm$. A distinct spectral line of neutral nitrogen (N I) occurs at $746.83nm$, too. A simulation with the internal IRS tool PARADE (Plasma Radiation Database) was performed in order to confirm this identification analysis. Another characteristic spectral line occurs at $656nm$ which can be either iron from sputtered grid material or hydrogen as residual in the background gas. This line was found in all spectra independent of the used propellant (see Figure 3.18). The analysis of the different positions shows that the fraction of excited N^+ increases when moving from the confinement plasma at position $1.5cm$ to the jet plasma at $2.5cm$ at the cathode exit, while the intensity of the molecule N_2 and atomic N (N I) decreases. Moving from position $2.5cm$ to $4cm$ into the inter-electrode space both intensities decrease as well. For a *spray* mode (see Figure 3.25 and 3.26) the same behavior appears for the neutral composites N_2 and N. However, for the ionized N^+ the intensity decreases from the 1.5 to $2.5cm$ position and stays almost constant jumping from the 2.5 to $4cm$.

Even though measurements were conducted at different pressure levels for argon and nitrogen, similarities are evident for the *spray* mode. However, the species distribution in *tight* mode is not consistent when comparing measurements in argon and nitrogen. Several issues could have an influence. Although the optical setup outside and the grid setup inside of the chamber were not changed between argon and nitrogen operation, the plasma bulk in the center and jet shape can be different due to the fact that the different propellants have distinct *I-V*-characteristics. In that way, it is possible that at $2.5cm$ different discharge regions were examined. Additionally, pressure levels are differing. These influences on plasma composition have not been investigated due to test setup constraints.

3.2.4. Discharge Stability and Transition between Operation Modes

The mode properties and therefore abilities for thrust generation are also linked to the stability of the respective mode. With bare eyes, the plasma jet seems to be perfectly stable. Nevertheless, the theory of jet extraction depicted in section 2.3 indicates that a
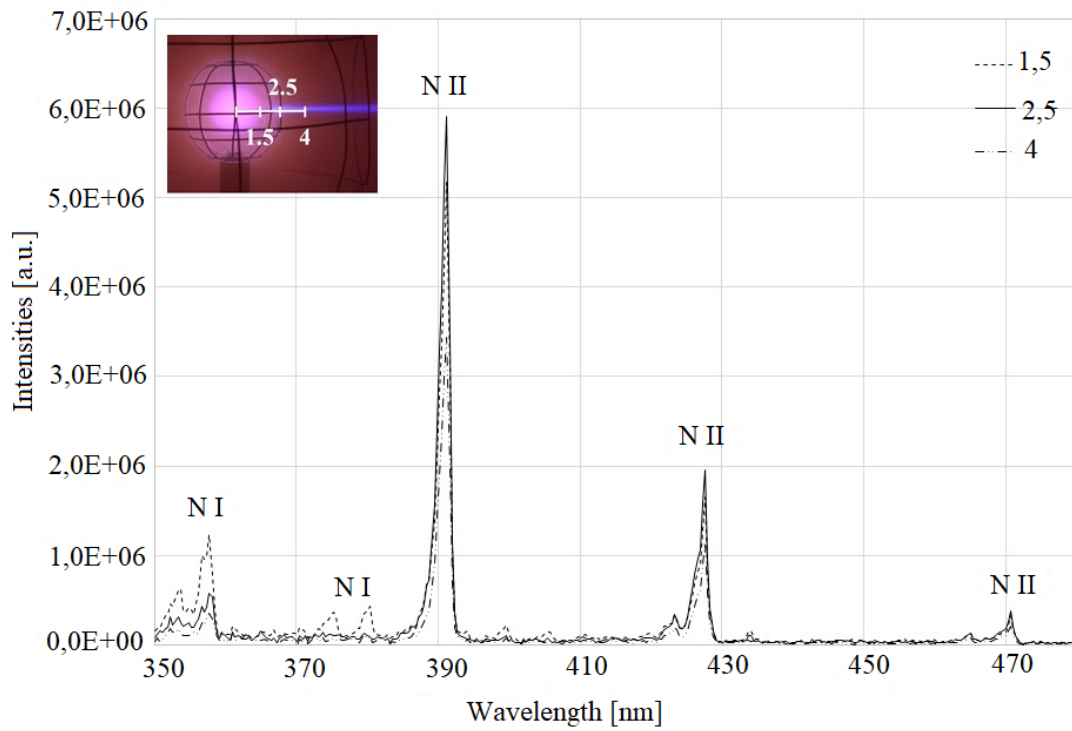
Figure 3.23.: Spectra of nitrogen discharge at position 1.5, 2.5 and $4cm$ in the wavelength range $350 - 480nm$ (*tight* jet, $V_D = 1737V, I_D = 5mA, p_{ch} = 1.6Pa$)
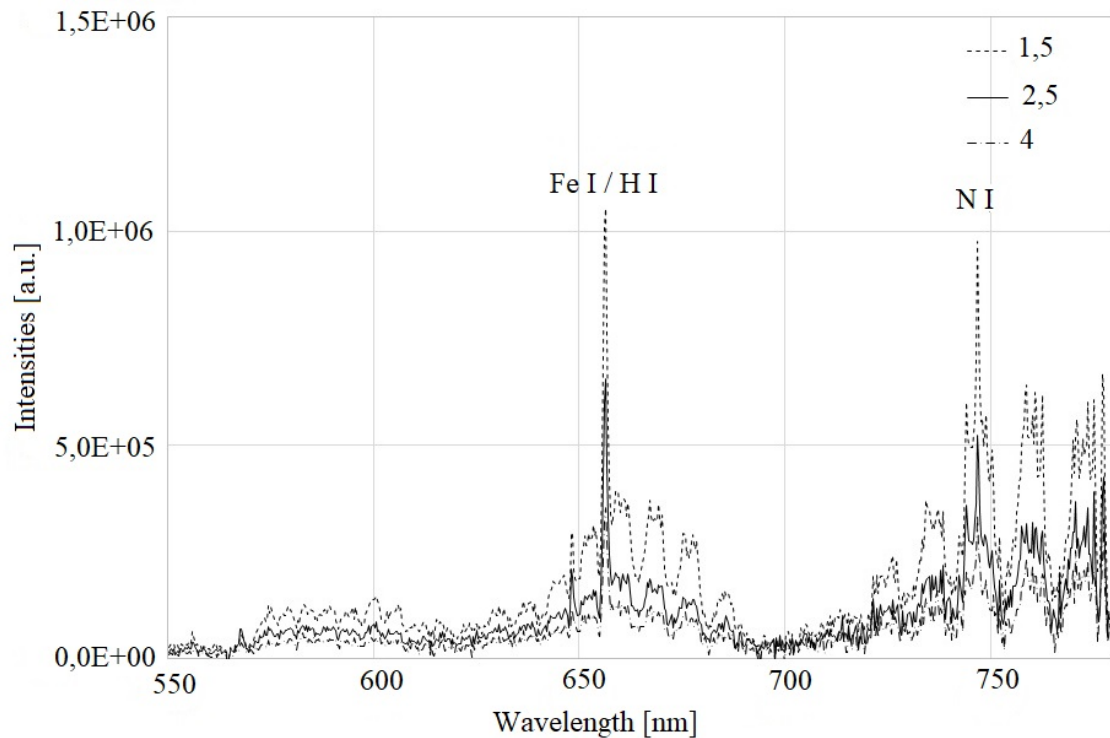
Figure 3.24.: Spectra of nitrogen discharge at position 1.5, 2.5 and $4cm$ in the wavelength range $550 - 800nm$ (*tight* jet, $V_D = 1737V, I_D = 5mA, p_{ch} = 1.6Pa$)
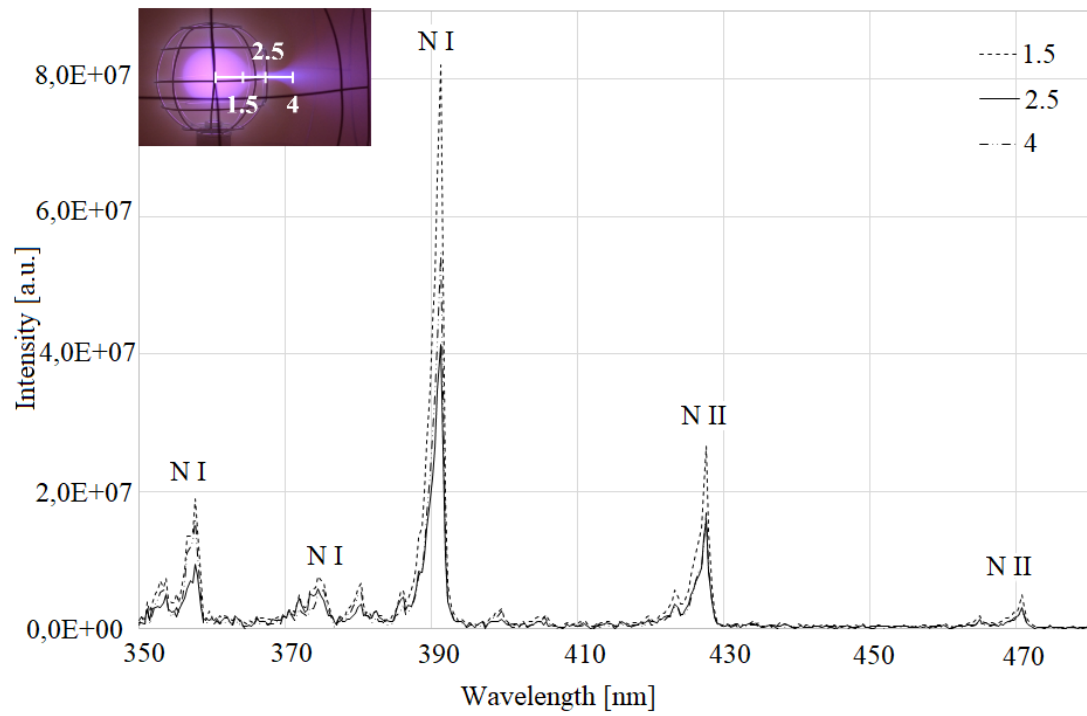
Figure 3.25.: Spectra of nitrogen discharge at position 1.5, 2.5 and $4cm$ in the wavelength range $350 - 480nm$ (*spray* jet, $V_D = 1990V, I_D = 50mA, p_{ch} = 1.6Pa$)
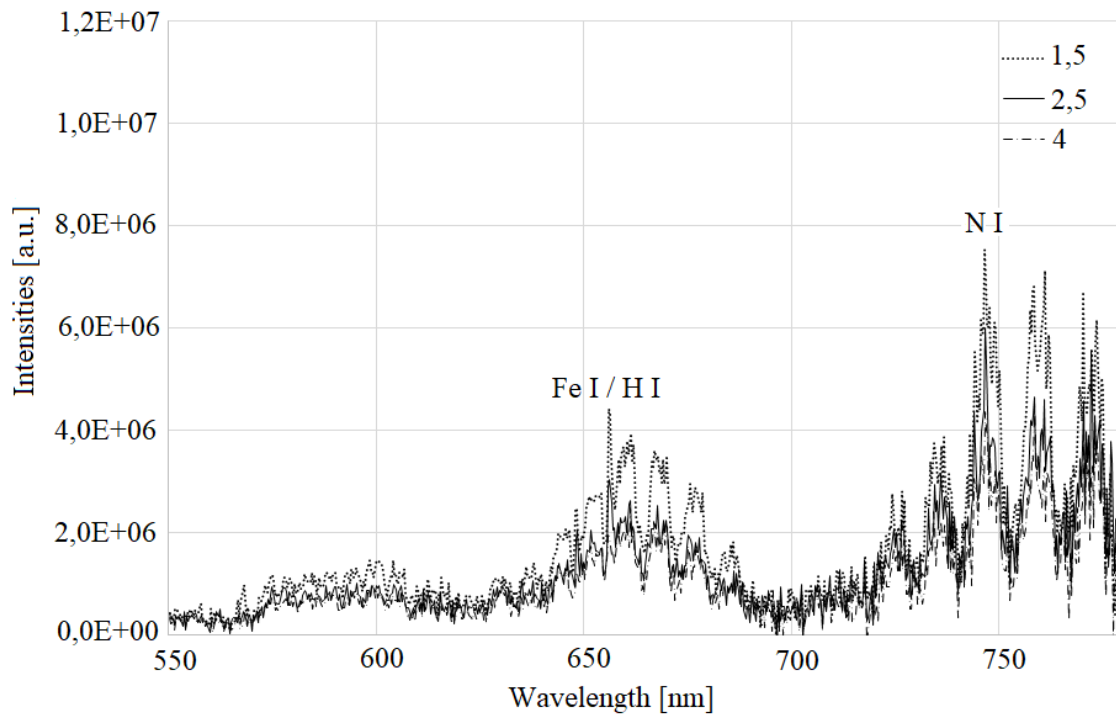
Figure 3.26.: Spectra of nitrogen discharge at position 1.5, 2.5 and $4cm$ in the wavelength range $550 - 800nm$ (*spray* jet, $V_D = 1990V, I_D = 50mA, p_{ch} = 1.6Pa$)

pulsed behavior due to ambipolar diffusion triggers the jet. In that case, this might be visible with a high-speed camera video. The *tight* jet was recorded at $1 - 5mA$ with a voltage of $700V$ in argon and with $10kHz$. At this frequency and low intensity of the IEC plasma, the noise is quite high, which is why a reliable statement about the stability of the mode is not possible. However, no pulsing of the plasma is observed with $200\mu s$ between pictures. Since the *spray* jet mode is brighter, recordings are more useful for this analysis. The video was recorded with $10kHz$ at $35mA$ discharge current and $600V$ discharge voltage. The confinement plasma shows a stable condition as well as the jet itself. However, a pulsing effect might be visible at the brightest point of the jet which is the point that separates confinement and jet. Due to the high noise this can only be evaluated as presumption. Hints about the mode characteristics can also be derived from the transition behavior. Although intensities for both modes are not very high, the difference between both modes is significant. Figures 3.27 a-i show parts of the transition video recorded at a $20kHz$ frame rate, aperture $f = 3 - 5$, $650V$ intensifier gain and $50\mu s$ exposure time for each frame. This picture sequence (3.27a-i) covers a time of $3.6ms$. Figure 3.27a shows the *tight* jet and Figure 3.27i the *spray* jet. Since the intensities of *tight*
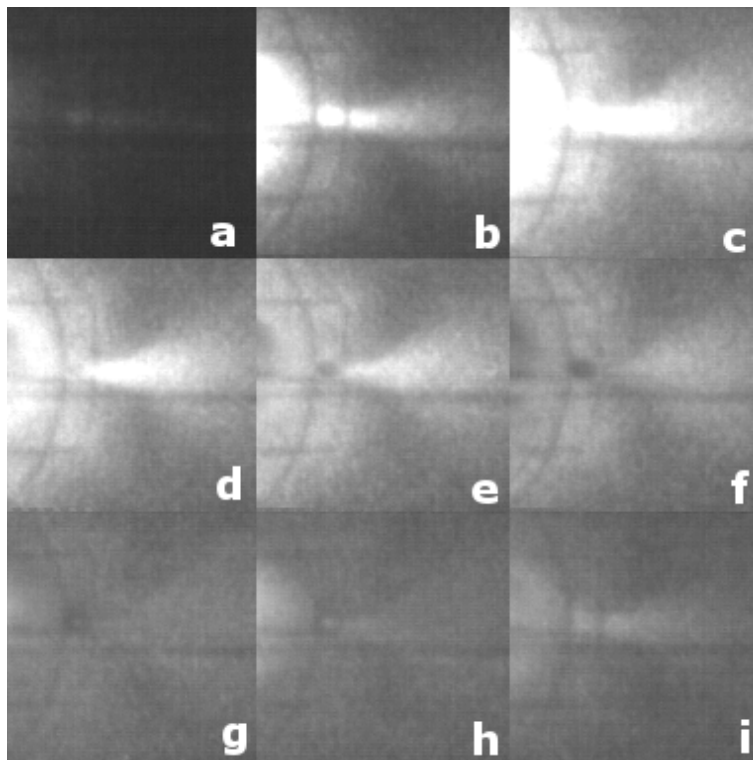
Figure 3.27.: Transition from *tight* jet to *spray* jet mode HSC data

jet, transitions plasma and *spray* jet cover a wide range, some of the pictures seem to be noisy and blurry. However, the phenomenon that triggers the transition can be seen very well. Starting in figure 3.27b, a bright plasma bulk from the inside of the cathode exits through the jet opening (3.27b-f). For the transition recording the pressure p_{ch} has been kept constant and the discharge voltage has been increased driving the current up as well. It is hypothesized that space charges in the cathode get very strong and at a certain point the external fields are not able to hold the confinement of the plasma within the cathode anymore. In Figures 3.27g-i then the *spray* mode builds up. It seems as if the plasma burst from the inside builds up a current bridge between cathode and anode. This is supported by current measurements with a shunt in the return line to the power supply (see Figure 3.2 for the setup). If the IEC device is operated in *tight* jet mode there is just a very small
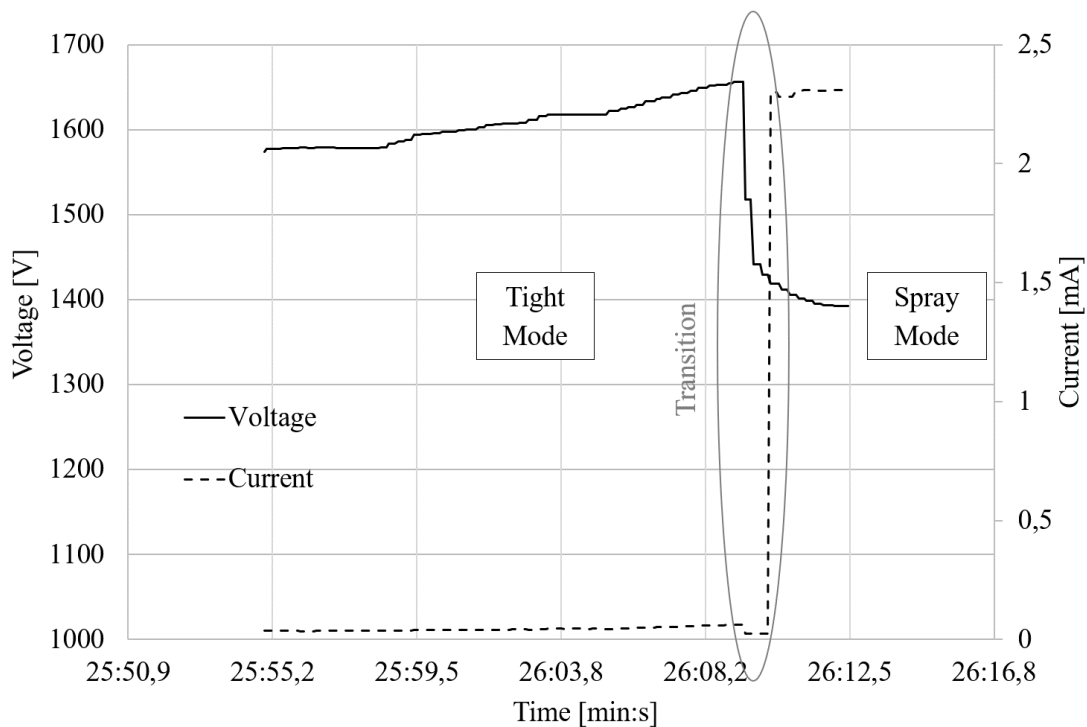
Figure 3.28.: Discharge voltage and current in return line for transition from *tight* jet to *spray* jet mode

percentage of the delivered current detectable in the return line of the power supply. As soon as the transition into the *spray* jet mode occurs, the current flowing in the return line increases significantly and is within the same order of magnitude as the provided current from the power supply. This issue is depicted in Figure 3.28 for argon. The *tight* jet mode operation conditions are the data points on the left side of the transition. The data points

on the right side of the transition are recorded in operation of the *spray* jet mode. It was evident, that for the *tight* jet mode the ratio (current in return line / delivered current) is very small (1%) compared to the ratio in the *spray* mode (almost 80%). This allows for the conclusion, that during the *tight* jet mode the current in the jet is not flowing to the anode but is leaving the grid system, whereas in the *spray* mode there is a kind of plasma bridge between the grids.

3.3. Conclusion Experimental Proof-of-Concept

The experimental proof-of-concept shall assess whether the jet extraction is applicable to thrust generation for electric propulsion applications. Therefore, a variable grid system has been build up in a dedicated vacuum test facility with an electrical and fluidic setup that couples IEC device and chamber (chamber background gas is used as propellant). The discharge characteristics and their dependencies have been investigated. Ignition and both *tight* and *spray* jet mode can be clearly differentiated by their appearance and their discharge parameters.

Just from the visual aspects, the *tight* jet mode seems to be a real jet extraction since the plasma is also visible outside of the inter-electrode space (see Figure 2.2). Still intensities of the jet are much lower than for the *spray* jet, which is characterized by a very diffuse and bright jet that is mainly visible in the inter-electrode space. Comparing the visual appearance also shows that the plasma composition of confinement and jet is different.

From the macroscopic point of view the discharge phenomena have been investigated for the following states with respect to their discharge currents and voltages. Ignition behavior with glow discharge has been characterized for used propellants and configurations and respective ignition laws for the tested configurations have been derived giving the breakdown voltage for a known $p \cdot d$.

With increasing input power after ignition, the IEC device can be operated in the different jet modes. Dependencies have been shown for design, propellant and pressure level. Typical *I-V*-characteristics can be derived for pressure and propellant variation. The *I-V*-characteristic distinguishes between *tight* and *spray* jet mode and shows a transition region. Generally, operation with all propellants is feasible. It is just depending on the available power source, since propellants like helium are harder to ionize than argon or nitrogen. Additionally, low-pressure ranges require higher power consumption for ionization. For each

propellant and pressure, there is a specific transition point when the *tight* jet jumps into the *spray* jet mode. This transition has been characterized by a change of currents flowing in the grid system. Measurements showed that the extraction current in *spray* mode flows also back between the grids so that an extraction of charged particles outside of the anode is unlikely. Although the discharge current in *tight* mode is lower and with the current not flowing back between the grids, an extraction out of the anode grid is more likely. It should be stated clearly, that at this point the jet currents cannot be linked directly to discharge current and voltage. This parameter visible by the *I-V*-characteristic can only give a state of the whole system. This state includes the glow discharge as primary particle source, all secondary particle sources and particle losses and therefore circulating currents. A parameter that has been introduced for ion accelerating systems, is the perveance. This parameter links the number of ions that can be extracted and focused into a beam to a given applied voltage:

$$Perveance = \frac{I_B}{V^{\frac{3}{2}}}. \tag{3.8}$$

For conventional two-gridded ion engines the beam current I_B is the sum of screen and accelerator grid current and the extraction potential is the potential difference between both grids. In case of IECs, which can be characterized with this parameter, definitions have to be distinguished for confinement and jet extraction. Different confinement setups were characterized with respect to space-charge effects within the cathode with this parameter [24,27]. The ion beams are defined as *microchannels* that build up in the cathode grid holes (defining an effective transparency) and inherit generated ions from the glow discharge and circulating ions from the confinement plasma. The circulating current has been defined as follows

$$I_{IC} = \frac{I_{PS} - I_{\hbar\nu}}{1 + \delta} \frac{2\eta_e}{1 - \eta_e^2}, \tag{3.9}$$

where I_{PS} is the power supply current, $I_{\hbar\nu}$ is the secondary photoelectric emission rate, δ is the secondary electron emission coefficient and η_e is the effective grid transparency [24,27]. For the confinement, the circulating current and applied grid potential can be used for perveance assessment. The definition for the jet extraction is more complicated, since the extracted jet current needs to be known and the extracting potential, which is assumed to be related to space charge effects within the cathode for an ion beam. In case of an electron beam, the hypothesis follows that the applied grid potential in combination with space-charge effects within the cathode, is the extracting potential. In summary, perveance can be a control parameter defining the operation modes, if all physical parameters can be

assessed. Considering the confinement and the change of plasma parameters with a jet, also the different modes (star and jet modes) can be distinguished with perveance.

If the confinement and the jets consist of ions, it is likely that actually thrust generation is feasible. The spectra for all propellants at the center position showed a proportion of neutrals, which is not surprising given that the center has a similar neutral background pressure as the rest of the chamber and only ions from the glow discharge (no assisted source) enter the cathode and oscillate through it. Additionally, loss mechanisms as ion-grid collisions and particle-particle collisions might occur. However, the bulk plasma also shows significant lines for ionized argon and nitrogen, but not for helium. Measurements in the *tight* and *spray* jet plasma for argon and nitrogen also showed a composition of ionized particles and neutral particles, both are existent.

For the evaluation of the proof-of-concept the following aspects have to be considered: Derived from what has been depicted so far, the *tight* jet mode is promising for thrust generation. Nevertheless, for the understanding of the jet extraction mechanism the following questions are still open:

- What is the origin of the ions in the jet? Are they coming directly from the confinement plasma or do they originate from electron impact ionization of an electron jet coming from the confinement ionizing the background gas?

- Is ambipolar diffusion the leading acceleration process of particles in the jet or only relevant for the extraction process?

Additionally, there are still open questions with respect to applicability to thrust generation in terms of:

- Are there enough ions within the *tight* jet to produce a remarkable thrust density?

- How high are the energies/velocities in the jet for an evaluation of I_{sp}?

- How dominant are losses as e.g. grid collisions reducing the efficiency?

- Is a larger operation envelope for the *tight* jet mode feasible to allow throtability?

The questions regarding the jet extraction mechanism could be answered or assessed by further studies with particles simulations as already started with the Ariadna study mentioned in section 2.1.1. Also, analytical thrust models can be set up, but should also be

validated by thrust measurements (direct or indirect). Starting points with respect to electric propulsion applications, can be ion current densities that are measured with Faraday cups and ion energies with retarding potential analyzers. Moreover, electron current densities and energies can be gained with these plasma diagnostics. Models for loss mechanisms are accessible from fusion IEC devices and can be extended for non-fusion applications. The last point has been investigated partially already in the proof-of-concept experiments. The pressure level can be reduced requiring higher input powers but allowing operation in *tight* jet mode at higher discharge currents. If the parameter that triggers the transition can be identified, then maybe a shift to even higher discharge currents for the *tight* mode is feasible. At this point, it is only understood that a plasma bulk from the cathode inside runs through the grid opening and establishes the plasma bridge between cathode and anode. And it is hypothesized, that this bridge establishes, because space charges within the cathode get so high, that the confinement with *tight* mode cannot be maintained anymore using the weakened potential at the enlarged grid opening as escape. Some of these points with respect to modeling will be assessed in the next chapter to support the experimental proof-of-concept.

4. IEC Plasma Modeling

Concluding from the experiments, the proof-of-concept will be supported by simulations. The first simulation will calculate the thrust by a model reflecting the potential physical effects leading to a jet extraction. This requires an understanding of the underlying phenomena, which hasn't been completed yet. Therefore, the approach foresees a step-by-step implementation. The second approach shall assess all possible losses and the required input power. Having that, an estimation of the residual input power inherited by the plasma gives a maximum of the power left for thrust generation. Since the understanding of the jet extraction is still limited, both approaches are in progress complementing each other. In cooperation with Gradel sàrl, having a profound expertise in neutron source development, the loss mechanisms of the IEC in fusion and non-fusion operation have been assessed and an approach of a thrust model has been introduced [19,40] (see Figure 1.2). Only partially implemented in this work up to this point, but to be completed in the future, will be a verification of these models with experiments.

4.1. Assessment of Losses in IEC devices

As stated above, one of the approaches followed in the analyses of IEC space propulsion applications is the assessment of loss mechanisms in IEC devices in non-fusion mode. Nevertheless, theoretical approximations about the influence of loss mechanisms in IEC neutron sources were developed [6] and are the starting point, although any losses provoked by the jet extraction mechanism are not considered. This means, that the residual energy in the confinement is the starting point for particle energies entering the jet. Figure 4.1 shows the different loss mechanisms that were considered, checked boxes are already implemented into a simulation tool and are to be verified (comparison code to code has been done, code to test to be done). Unchecked points, e.g. charge exchange reactions, require further consideration and will be discussed in conclusions and outlook. The relevant particle losses can also be categorized according to the relevant electron processes [41], which are

1. Radiative

   a) transitions between bound states,

   b) free-bound transitions: recombination/photoionization,

2. Collisional

   a) electron impact excitation/deexcitation,

   b) impact ionization/three-body recombination,

   c) dielectronic recombination/autoionization.

Transitions between bound states (1a) are also classified in three categories [41]:

- atom with an electron in upper energy level can decay to a lower energy level,

- atom with an electron in a lower energy level can absorb a photon by transition to an upper level,

- induced decay of electron from higher to lower energy level due to presence of radiation.

As part of the following investigations for excitation losses only the decays of electrons to lower energy levels ((1a) radiation induced and not induced decay, decay after electron impact excitation (2a)) have been considered, because these processes can be directly investigated with OES experiments. That way the energy that has been fed into the system can only be observed indirectly. This measurement technique doesn't distinguish between different decays too. Free-bound transitions (1b) are considered in Bremsstrahlung radiation. Two forms of this radiation resulting from electron-ion encounters are known. A free-free transition means the electron is in a free state after the encounter as well. A free-bound transition means the electron has been captured by an ion during the encounter. Electron-electron collisions are only relevant if their velocities are relativistic. An example will be given in the respective subsection. The ionization process is implemented through an ionization model inheriting electron impact ionization (2b).

The particle density solver delivers the particle densities that are relevant for all loss calculations (see Figure 4.1). For verification purposes, the ionization cross sections of argon and helium were compared with data from NIST. This work is not part of this thesis, but has been published [42]. Additionally, loss mechanisms occurring in fusion mode (with a fusion propellant) were computed and then compared to the work of Rider [6], followed by simulations in non-fusion mode with argon and helium with the same tool, which will be presented. This way forward was chosen for Bremsstrahlung, ion-grid collision and electron-grid collision losses. For excitation losses, the intensities were computed and compared to spectral data of NIST and then compared to experimental data. The following sections will

show the underlying theories and laws for the presented loss mechanisms in more detail and present the results of simulations and experiments.
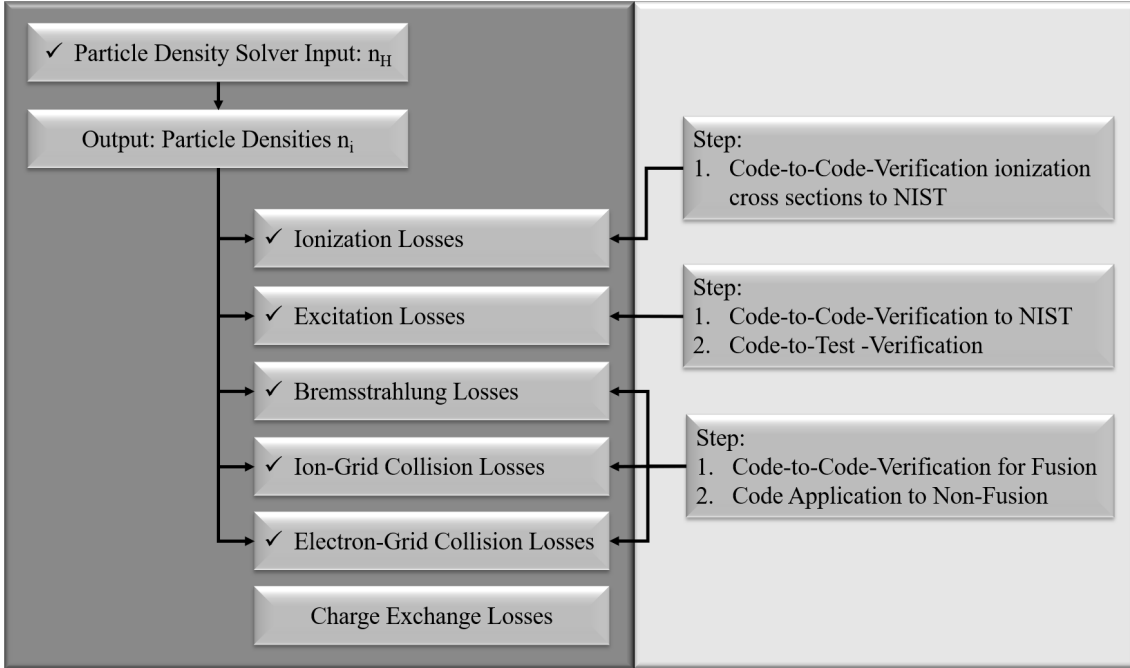
Figure 4.1.: Loss mechanisms in IEC devices with verification steps

4.1.1. Particle Density Model

For loss estimations, the particle densities in the IEC system are needed. Since the used power level determines the degree of ionization and therefore electron and ion densities, the Saha equation has been used for plasmas in local thermal equilibrium (LTE). The Saha model is based on an equilibrium of ionization and recombination [43]. This approach is a one-temperature model, only taking into account an absolute temperature. According to this, the Saha model can be described with [44]:

$$\frac{n_{i+1} \cdot n_e}{n_i} = \frac{2U_{i+1}}{U_i} \left(\frac{2\pi m_e k_B T_e}{h^2} \right)^{3/2} exp\left(-\frac{E_i}{k_B T_e} \right), \qquad (4.10)$$

with the particle densities n_i of the ionization levels, electron density n_e, the respective partition functions U_i , electron mass m_e, Boltzmann constant k_B, electron temperature T_e, Planck's constant h and ionization energy E_i of an ionization level i. Depending on the number of ionization levels i, a set of i equations has to be solved. This system of equations can be solved analytically and numerically. A numerical approach will be presented in the following, which has been developed by Zaghloul et al. [44]. Assuming

quasi-neutrality and the total heavy particle density being constant with a combination of ionization and recombination processes, the following Equation (4.11) for the electron density and Equation (4.12) for the heavy particle density complement Equation (4.10).

$$n_e = \sum_1^i i \cdot n_i, \tag{4.11}$$

$$n_H = \sum_{i=0}^n n_i. \tag{4.12}$$

This leads to the expressions:

$$\sum_{i=1}^n i \cdot \alpha_i \;=\; Z_{av}, \tag{4.13}$$

$$\sum_{i=0}^n \alpha_i \;=\; 1, \tag{4.14}$$

$$\frac{\alpha_{i+1} Z_{av} n_H}{\alpha_i} \;=\; f_{i+1}(T_e, E_i), \tag{4.15}$$

if Equation (4.12) is written using the molar fraction $\alpha_i = n_i/n_H$ and the average charge of the plasma $Z_{av} = n_e/n_H$. Rearranging Equation (4.15) provides a recursive relation:

$$\alpha_{i+1} = \frac{f_{i+1}(T_e, E_i)}{Z_{av} n_H} \cdot \alpha_i. \tag{4.16}$$

Equation (4.16) is not linear due to the correlation between Z_{av} and α_i. The derived equation for the molar fraction of the neutral particles is:

$$\alpha_0 = Z_{av} \left(\sum_{i=1}^n \frac{i \prod_{j=1}^i f_j}{(Z_{av} n_H)^i} \right)^{-1} \tag{4.17}$$

that cannot be solved analytically. But Equation (4.17) can be combined with (4.16) leading to:

$$1 - Z_{av} \left(\sum_{i=1}^n \frac{i \prod_{j=1}^i f_j}{(Z_{av} n_H)^i} \right)^{-1} \left[1 + \sum_{i=1}^n \frac{i \prod_{i=1}^i f_j}{(Z_{av} n_H)^i} \right] = 0, \tag{4.18}$$

which is solved for the average charge state Z_{av}. With Equation (4.17) and Equation (4.16) the molar fraction and consequently the densities of ionized and neutral particles can be obtained at any temperature.

4.1.2. Ionization Losses

Since ionization of the working gas is mandatory to create a plasma, this loss mechanism cannot be reduced with respect to power consumption. It is defined by the ionization

energies of the gases. Ionization levels of first order are required to create ions that can be accelerated by electrostatic fields. Ionization levels of higher order are not required, but might occur in the system. They should be avoided, because they will increase the power consumption for ionization and might aggravate erosion processes on the grids. For this solution, the Saha solver output has been coupled with the assessment of Lotz [45] for ionization cross sections. Additionally to the ionization energy, the number of ionized particles in a given time step, the ionization rate, is needed to calculate the power used for propellant ionization. The ionization cross section is averaged over an equilibrium distributed energy. The following definition has been applied:

$$\sigma_{ion}(E_C) = 2.78\pi a_0^2 \frac{R_y^2}{E_C E_i} \zeta ln\left(\frac{E_C}{E_i}\right), \tag{4.19}$$

where R_y is the Rydberg energy, a_0 the Bohr radius and ζ the number of electrons with the same principal and azimuthal quantum number in the outer electron shell. Derived from this equation, the following temperature-dependent rate coefficient $k_{ion,i}(T_e)$ is given by [46]

$$k_{ion,i}(T_e) = 5.56\sqrt{\pi}\zeta \left(\frac{4\pi\epsilon_0\hbar^3}{m_e^2 e^2}\right) \left(\frac{R_y}{E_i}\right)^{3/2} \sqrt{\frac{E_i}{k_B T_e}} \Gamma\left(0, \frac{E_i}{k_B T_e}\right), \tag{4.20}$$

where ϵ_0 is the vacuum permittivity, $\hbar = h/(2\pi)$ the reduced Planck constant and e the elementary charge. This equation is only valid if this criterion is fulfilled:

$$n_e < \frac{3}{4\pi} \left(\frac{k_B T_e}{e^2}\right)^3. \tag{4.21}$$

Multiplying Equation (4.20) with the neutral or ion particle density on level i gives an ionization rate for the ith level. And with the dedicated ionization energy E_i (Table 4.1 and 4.2, [47]) and ion particle density n_i for the next ionization level, the power lost due to ionization for a given electron temperature can be derived to:

$$\frac{P_{ion,i}}{V_{ion}} = (k_{ion,i}(T_e) \cdot n_{i-1}) \cdot E_i \cdot n_i(T_e). \tag{4.22}$$

The respective ion densities n_i and n_{i-1} are calculated by using the Saha equation (see section 4.1.1). The power loss due to ionization reaching the first ionization level is calculated by $n_{i-1} = n_0 = n_H$. For comparison with experiments, this parameter will be multiplied with the volume of the used IEC design. Since the ionization process cannot be isolated to the inter-electrode space, the whole volume of the IEC is assumed to be ionization zone, which results into $V_{ion} = 4/3\pi r_A^3$.

Table 4.1.: Ionization energies of argon

i [-]	1	2	3	4	5	6	7	8	9
$E_i[eV]$	15.76	27.63	40.74	59.58	74.84	91.29	124.41	143.46	422.60

Table 4.2.: Ionization energies of helium

i [-]	1	2
$E_i[eV]$	24.59	54.42

4.1.3. Excitation Losses

For the assessment of the power loss due to excitation processes, the wavelength of the emitted photons needs to be known, if an electron falls down from a higher excitation state. There are various transitions depending on species and excitation states of the particles. The energy difference between higher energy state k and lower energy state j can be calculated by

$$\Delta E_{kj} = \frac{h \cdot c_0}{\lambda_{kj}}, \tag{4.23}$$

with the speed of light in vacuum c_0 and the emitted wavelength λ_{kj}. Transitions can be found in the NIST database. Having the wavelength and energy levels, the respective Einstein coefficient A_{kj} can be found, stating the probability per second of an atom in excited state k to decay to an energy level j. The wavelength-dependent power loss can be derived from

$$\frac{P_{exc}}{V_{exc}} = \frac{h \cdot c_0}{\lambda_{kj}} A_{kj} n_{i,k}, \tag{4.24}$$

where $n_{i,k}$ is the particle density of a particle of ionization level i (see section 4.1.1) in the k-th excitation level. Assuming a Boltzmann distribution, this can be calculated using

$$n_{i,k}(T_e) = n_i(T_e) \frac{g_{i,k}}{U_i} exp\left(-\frac{E_{i,k}}{k_B T_e}\right), \tag{4.25}$$

with $g_{i,k}$ the degeneracy factor of the k-th excitation level of a particle of ionization level i and $E_{i,k}$ the respective excitation energy. The partition function can be calculated using:

$$U_i = \sum_{k=0}^{m} g_{i,k} \cdot e^{-\frac{E_{i,k}}{k_B T_e}}. \tag{4.26}$$

Summing up Equation (4.24) over all wavelengths gives the total excitation loss. For comparison with experimental data, the calculated power loss density will be multiplied

with $V_{exc} = 4/3\pi r_C^3$, since the detectable excitation processes were recorded in the cathode interior and not in the inter-electrode space (section 3.2.3 OES measurements). Additionally, with the calculated power loss per transition, which is the line intensity, a spectrum can be generated, that helps identifying lines in an OES measurement. Vice versa, the temperature and electron density can be estimated by fitting a measured spectrum to the calculated spectrum.

4.1.4. Bremsstrahlung Losses

This type of radiation occurs when a charged particle is deflected by another charged particle. During this encounter the electron emits Bremsstrahlung and loses some of its kinetic energy. Two expressions are discussed here in order to determine the overall power lost due to Bremsstrahlung P_{Brems}. The first approach, stated in Rider [6], is given as volumetric power density

$$\frac{P_{Brems}}{V_{Brems}} = S_{Brems}n_e^2\sqrt{\frac{k_BT_e}{e}}\left(\frac{\frac{n_j}{n_k}+Z_k^2}{\frac{n_j}{n_k}+Z_k}\left[\left(1+0.007936\frac{k_BT_e}{m_ec_0^2}\right.\right.\right.$$
$$\left.\left.\left.+1.874\left(\frac{k_BT_e}{m_ec_0^2}\right)^2\right)+\frac{3}{\sqrt{2}}\frac{k_BT_e}{m_ec_0^2}\right]\right), \tag{4.27}$$

where S_{brems} is the radiation constant for Bremsstrahlung, Z is the charge number. The first ion species is denoted by the index j, while the index k denotes the second ion species. The second approach is provided by Petkow et al. [48]:

$$\frac{P_{Brems}}{V} = S_{Brems}n_e^2\sqrt{\frac{k_BT_e}{e}}\left(\frac{\frac{n_j}{n_k}Z_j^2+Z_k^2}{\frac{n_j}{n_k}Z_j+Z_k}\right). \tag{4.28}$$

Equation (4.27) represents an interpolation between a non-relativistic and an extreme relativistic modeling of [49]. Equation (4.28) presents a formulation of classical physics. If the expression $k_BT_e/m_ec_0^2$ in Equation (4.27) is very small, the expression of classical physics is left as approximation. The formulation of [6] can only be used for fuels whose charge state of the first reactant species is $Z_j = 1$. For verification purposes, it is necessary to state that there is a little variance in the value of the Bremsstrahlung radiation constant. Reference [6] uses $S_{brems} = 1.69 \cdot 10^{-38} m^4\frac{\sqrt{Ckg}}{s}$ and [48] uses $S_{brems} = 1.6289 \cdot 10^{-38} m^4\frac{\sqrt{Ckg}}{s}$. However, the impact of this difference is negligible. For the following calculations the approach of Rider has been used. For comparison with experiments P_{Brems}/V_{exc} has to be turned into a design-dependent value. In this case, it is assumed that these losses will mainly occur within the cathode, where high charge carrier densities exist, so that $V_{Brems} = 4/3\pi r_C^3$.

4.1.5. Ion and Electron Grid Collision Losses

Particle-grid collisions can have an efficiency reducing impact and also be a major life-limiting factor. The traces of grid collisions have also been noticed at the cathode grids of the configuration tested for the proof-of-concept. Figure 4.2 shows the surface of the C3a cathode. On the inside the wire surface is still bright, while on the outside the surface is roughened.

<div align="center">

(a) cathode inside   (b) cathode outside
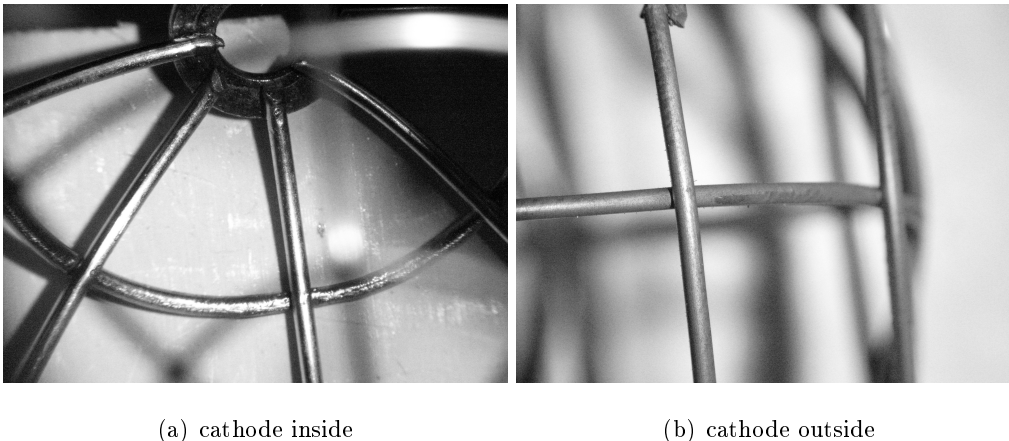
Figure 4.2.: Cathode erosion

</div>

For considering particle-grid collisions, a division of the plasma regions within the confinement is necessary. If a spherical grid setup is chosen, for verification of the results on the one hand and calculating the losses for the IRS IEC setup on the other hand, the following assumptions based on Rider [6] can be used. Assuming a single potential well (as it is the case for glow discharge operation) is created within the cathode, the plasma can be divided into three regions: core, mantle, and edge. The core is defined as $0 < r < r_{core}$, where r is the radius and r_{core} is the core radius, the mantle region as $r_{core} < r < r_{ed,in}$, and the edge region as $r_{ed,in} < r < r_{ed,out}$, whereat $r_{ed,out}$ equals the cathode radius (see Equation (4.29) and Figure 4.3a). The plasma densities of both species, electrons and ions, are assumed to stay constant in the core region, then drop off with $\frac{1}{r^2}$ up to $r_{ed,in}$ and then remain constant again (see Figure 4.3b).

$$n_{e,i} = \begin{cases} (n_{core})_{e,i} & 0 < r < r_C \\ (n_{core})_{e,i} \left(\frac{r_C}{r} \right)^2 & r_C < r < r_{ed,in} \\ (n_{core})_{e,i} \left(\frac{r_C}{r_{ed,in}} \right)^2 & r_{ed,in} < r < r_{ed,out}. \end{cases} \tag{4.29}$$
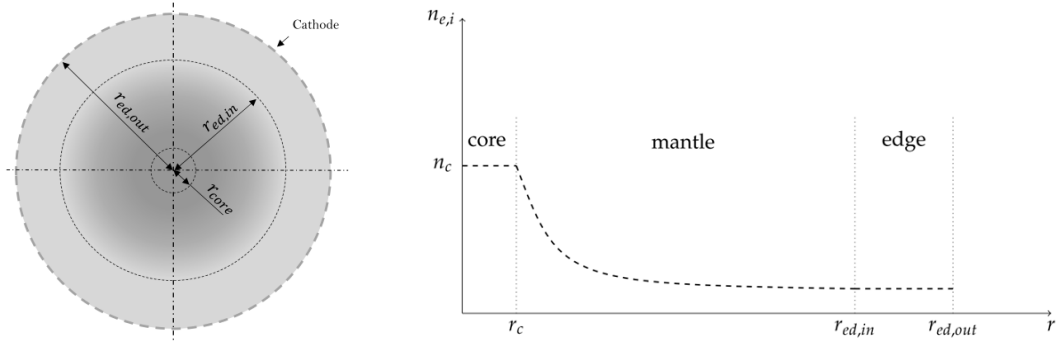
(a) Schematic of plasma regions in a spherical IEC cathode ($r_{ed,out} = r_C$)

(b) Theoretical density characteristic in a single potential well [6]

Figure 4.3.: Classification of plasma regions

An expression for the power lost due to electron-grid and ion-grid collision is given as [6]

$$P_{Grid,e,i} = (1 - \eta_{e(e,i)})4\pi r_C^2 n_{C,e,i} v_{e,i} E_{C,e,i}, \tag{4.30}$$

with

$$v_{e,i} = \sqrt{\frac{2E_{C,e,i}}{m_{e,i}}}, \tag{4.31}$$

where the index e denotes electrons and index i the ions. Theoretically there is the geometric transparency η_g, but a reasonable assumption is also $\eta_e = 0.99$ for electrons and ions if the effective transparency is considered, because the so-called *multichanneling* can lift the transparency to such high values. Additionally, it is assumed to be the same value for ions and electrons. The grid radius is $r_C = r_{ed,out}$, the grid density $n_{C,e,i}$ is the respective particle density at the cathode, given by Equation (4.29). Moreover, $n_{core,e} = n_{core,i}$ is implied, as well as electrons and ions possessing the same energy when colliding with the grid, defined as $E_{C,e} = E_{C,i} = e \cdot \Phi_{well}$, with Φ_{well} being the grid potential difference. Up to now, only the first ionization stage has been implemented here for ion-grid collisions, which is supposedly the main contributor to erosion processes at the grid and deflection of ions in the cathode grid region. Electron-grid collisions can be calculated according to this assessment, but are mainly relevant for those generated in the inter-electrode space by glow discharge. This loss mechanism will not be as relevant as excitation for the confinement region.

4.1.6. Results

This section shows the results of calculated losses for argon and helium, also using operation conditions from experimental test campaigns. These operation points cover *tight* jet and *spray* jet conditions. However, as stated before, the losses assessment does not consider losses specifically provoked by an extraction, but only considers the overall discharge and collision losses, which can be design-dependent and design-independent. Table 4.3 shows again an overview. Ionization losses are considered here design-dependent, since several plasma sources (section 2.2) exist and therefore, the power needed for ionization can also be considered design-dependent. External sources or assisted glow discharges usually have higher ionization degrees than a glow discharge.

Table 4.3.: Loss mechanisms in IEC devices divided in design-dependent and design-independent categories

Design-dependent losses	Design-independent losses
Ion-grid collisions	Bremsstrahlung
Electron-grid collisions	Excitation
Ionization / Dissociation	Charge-Exchange

The simulation tool, inheriting these solvers, has been implemented in Matlab™. Three divisions are available for the user: *Verfication*, *Comparison* and *Design*. The *Verification* part allows to implement and test a new function before using it for the *Comparison* or *Design* part. Subdivision of fusion and non-fusion operation allowed the usage of validation input parameters and models of fusion devices that have a substantial database. The *Comparison* part allows to use the implemented models and compare them for the same propellant or use the same model and compare losses for different propellants. The *Design* section has only been implemented for the non-fusion operation though. It allows a selection of fuel (argon/helium). Additionally, other input parameters related to the geometric design were implemented which can be varied, giving the losses for a specific design. For validation purposes, a tool enabling the output of a spectrum with electron density and temperature has been implemented, which also can be used here. The following operation conditions for argon (see Table 4.4) have been used, which are the same as operated for OES measurements with configuration C3a (see section 3.2.3). Helium operation conditions were also chosen with configuration C3a depicted in section 3.2.2. The numerical

Table 4.4.: Operation conditions

Operation Point	Propellant, Mode	Pressure p_{ch}	Input Power	Voltage V_D	Heavy particle density n_H
Ar 1	Argon, *tight*	$1Pa$	$13.55W$	$2710V$	$2.4137 \cdot 10^{20} m^{-3}$
Ar 2	Argon, *spray*	$1Pa$	$124.35W$	$2487V$	$2.4137 \cdot 10^{20} m^{-3}$
He 1	Helium, *tight*	$1Pa$	$1.28W$	$2557V$	$2.4137 \cdot 10^{20} m^{-3}$
He 2	Helium, *tight*	$1.5Pa$	$6.3W$	$3500V$	$3.621 \cdot 10^{20} m^{-3}$

solver requires the heavy particle density n_H as input parameter. An assessment using the chamber pressure p_{ch} via the ideal gas law can be used here:

$$N = \frac{p_{ch} \cdot V_{ch}}{k_B \cdot T_H},\tag{4.32}$$

with the particle number N and the chamber volume V_{ch}. The heavy particle density is then given by $n_H = N/V_{ch}$ and stated in Table 4.4. A heavy particle temperature of $300K$ was assumed as starting condition. If not stated otherwise, an effective transparency of 0.99 was assumed.

The diagrams in Figure 4.4 and 4.5 show the different number densities n_i of ionization levels i for operation condition Ar1 and He1 as example. For argon, six ionization levels are reached up to a temperature of $50000K$. For helium, only the first ionization level is shown within this temperature range, which is linked to the fact, that for priorities only the first ionization level is available for the ionization rate coefficients up to now and the OES measurements don't show reliable ionization data yet. According to the experimental results of section 3.2.3, the plasma composition of the confinement and jet consists of neutral argon and singly-ionized argon. As described, the optical emission spectroscopic measurements showed no helium ions. However, a discharge can be maintained which proofs the existence of at least singly-ionized helium. The derived characteristics for the particle density levels from the Saha solver are comprehensible. The power used for ionization processes has been based on a model using ionization rate coefficients in order to gain the ionization rate. The coefficients are plotted for argon in Figure 4.6. The ionization power loss is depicted in Figure 4.7 for argon and helium in all four operation conditions. The characteristics of ionization losses for argon are the same for Ar1 and Ar2, since both work with the same operation pressure. The exact temperature vs. power loss points are different, but both operation points will be in the range of the first ionization
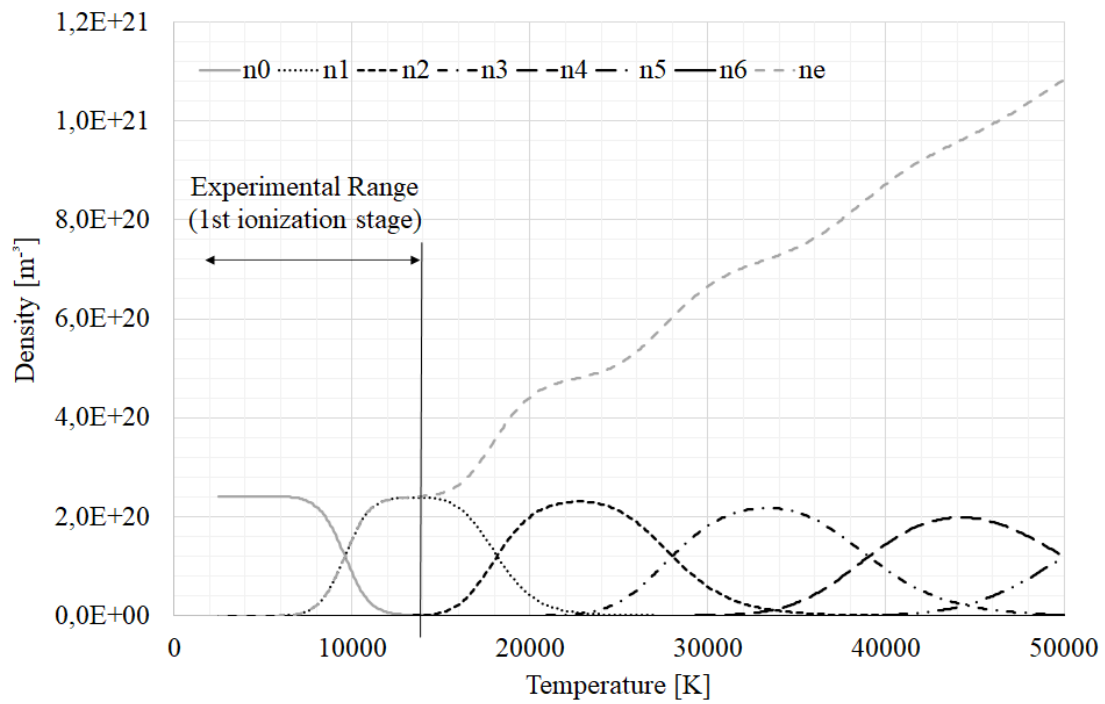
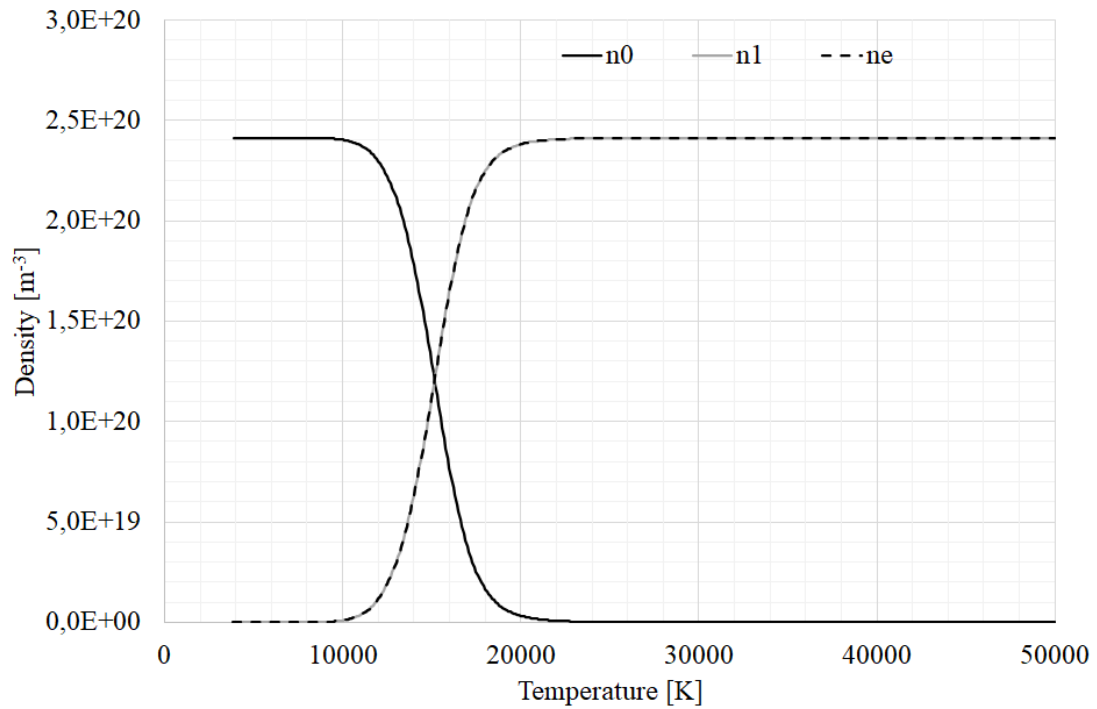Figure 4.4.: Particle densities of argon ionization (Ar1)

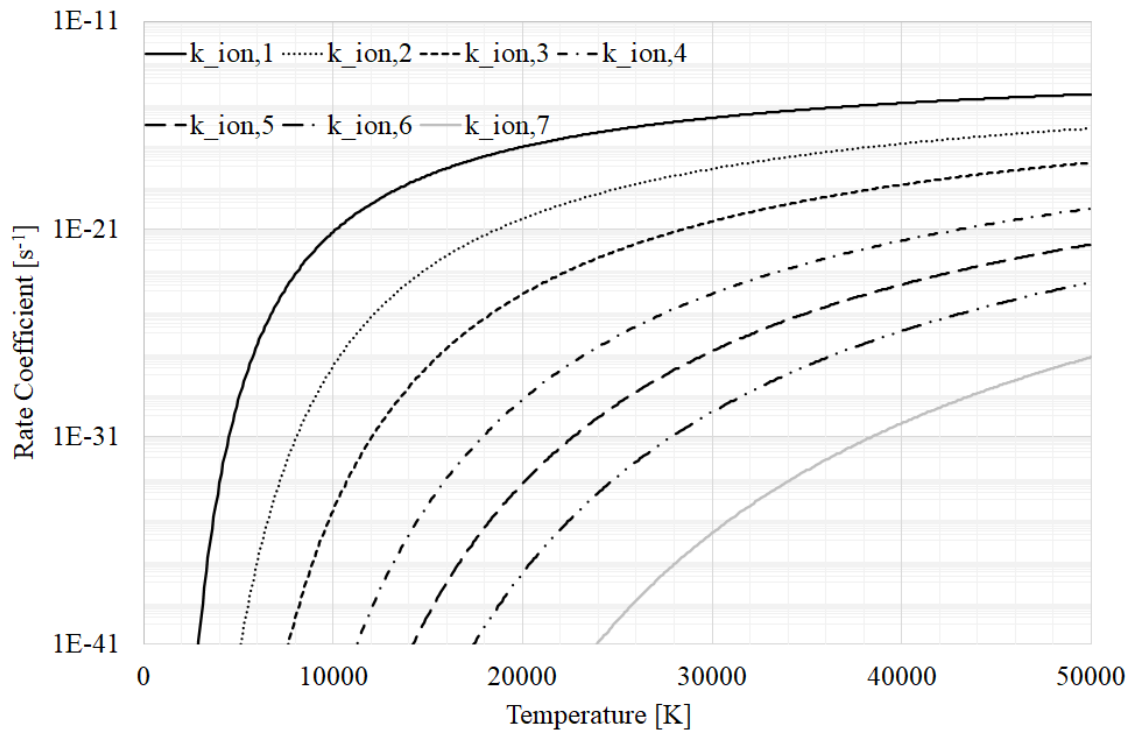Figure 4.5.: Particle densities of helium ionization (He1)

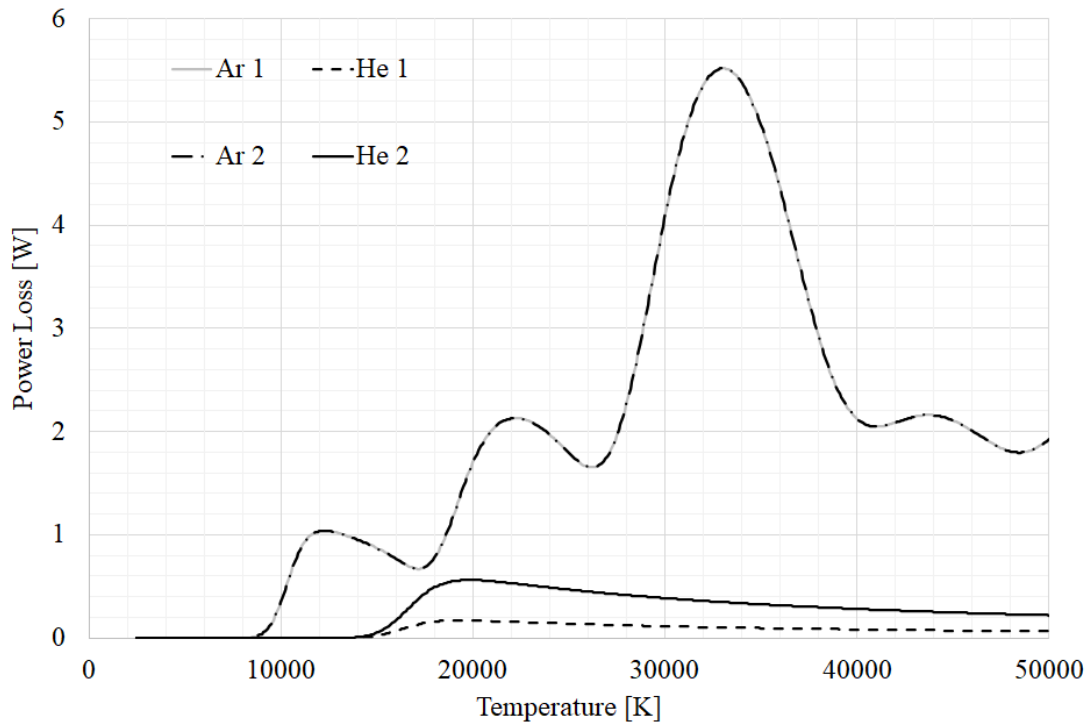Figure 4.6.: Argon ionization rate coefficients (Ar1)

Figure 4.7.: Ionization losses: argon and helium

level (n_1/n_0 -ratio is different for both points due to different discharge currents). As expected, the first ionization level of helium needs higher electron temperatures. Operation condition He2 has been operated with 33% higher heavy particle density which results in a characteristic with higher power losses. Here again, the exact temperature vs. power loss point is not known for both operation points. It is also noticed that less power is lost due to ionization of helium (only the first ionization stage is considered) than of argon with this assessment. However, more input power might be needed in order to reach the higher electron temperatures due to other collisional loss mechanisms, i.e. excitation.

Excitation losses have been derived, assuming a Boltzmann distribution of particle densities in excited states. The power loss or radiated intensities that have been calculated according to Equation (4.24) are also used to gain optical spectra which in turn allows comparison with the experimental spectra described in section 3.2.3. Spectral lines can be identified easily and an estimation of excitation temperature and electron densities can be feasible. The temperature derived from radiative deexcitation is based on consideration of collisional and radiative transitions into excited states. The NIST Saha-LTE spectra are calculated using a Saha distribution for the ionization level populations and a Boltzmann distribution for the population of the energy levels, which is also the case for the other models presented in this thesis. The NIST atomic database gives references for relative intensities for the transitions too. However, these intensities are source dependent and do not exactly match the calculated intensities, since they are dependent on the EEDF. P_{exc} according to Equation (4.24) has been depicted in Figure 4.8 and 4.9. The argon data at the higher wavelength range from $650 - 850nm$ shows a minor deviation between NIST intensities and calculated intensities (SIM) of maximum 16% (both have been normalized to the same maximum peak in the spectrum of P_{exc} at $811, 53nm$ for the respective data sets). But the fit shows high deviations in intensities for distinct peaks of up to 60% for wavelengths $< 650nm$. The values should be considered as qualitative values that describe the appearance of a particular spectrum in emission and are only approximately quantitative. Additionally, a helium data set ($p_{ch} = 4.3 \cdot 10^{-2} mbar$, $V_D = 1697V$ and $I_D = 10mA$) for the C2a confinement has been taken to check whether the line identification in Figure 3.18 is correct. Only neutral helium has been found. It is evident that the highest peak at $656nm$ is not related to helium, but to stainless steel. Similar to the argon data set, NIST and simulation data fits match better in the wavelength range $> 400nm$. Here, deviations are in the range of 9 to 20%. For wavelengths lower than $400nm$, the

deviations increase up to 50% for some peaks. The experimental data of argon from section 3.2.3 has been normalized with the same maximum peak (see Figure 4.8). The fitting approach of experimental data with simulated data considered that all peaks are visible and the intensity level is reached. The latter was not feasible for all peaks in these spectra, which is why the temperature and density assessment can only be considered preliminary. Here again, deviations between simulated and experimental data are higher for wavelengths $< 550nm$. In this case up to 60%. At wavelengths $> 650nm$ deviations are between $1 - 30\%$ except for two lines with 50%. For helium the spectra have been normalized to the helium peak of $501nm$ in a first step, which showed that the line ratios do not match at all between simulated and experimental data. Line $587nm$ has been taken instead, which provides a better match. However, experimental data and simulated data have even higher deviations from each other than for argon. An explanation for these differences can be an electron energy distribution that differs from the Maxwell-Boltzmann distribution, so that particle densities in excited states will be different. Also, other elements as part of the residual gas in the chamber and erosion products which are part of the plasma have not been taken into account for the simulations, but are visible in the recorded spectra. These species interacting with the argon or helium plasma can alter the particle energy distribution functions. The erosion process itself also acts as an energy sink. The temperature and density estimations for argon that have been derived are shown in Table 4.5. The gained data for helium is even less significant than for argon due to the deviations, resulting into inaccurate fits that give a rough temperature range of $18000 - 22200K$.

The total power loss due to excitation is depicted in Figure 4.10 and the values shown in Table 4.6 have been derived for the confinement position operating Ar1 and Ar2. A temperature of $20000K$ has been assumed for He1 and He2 exemplarily. The very high excitation losses are mainly occurring at wavelengths $< 200nm$, which is not in the detection range of the used spectrometer $(200-1100nm)$, so that they cannot be confirmed and used for fitting experimental data to simulated data. For argon 98.3% of the power loss, mainly generated by transitions at the wavelengths $104.82nm$ and $106.67nm$ for neutral argon and for helium 98.5%, mainly at the wavelength $58.43nm$, contribute to these high values. Since the electron energy distribution has not been confirmed yet to be Maxwellian, these power levels are also not confirmed and not plausible when compared to experimental data.
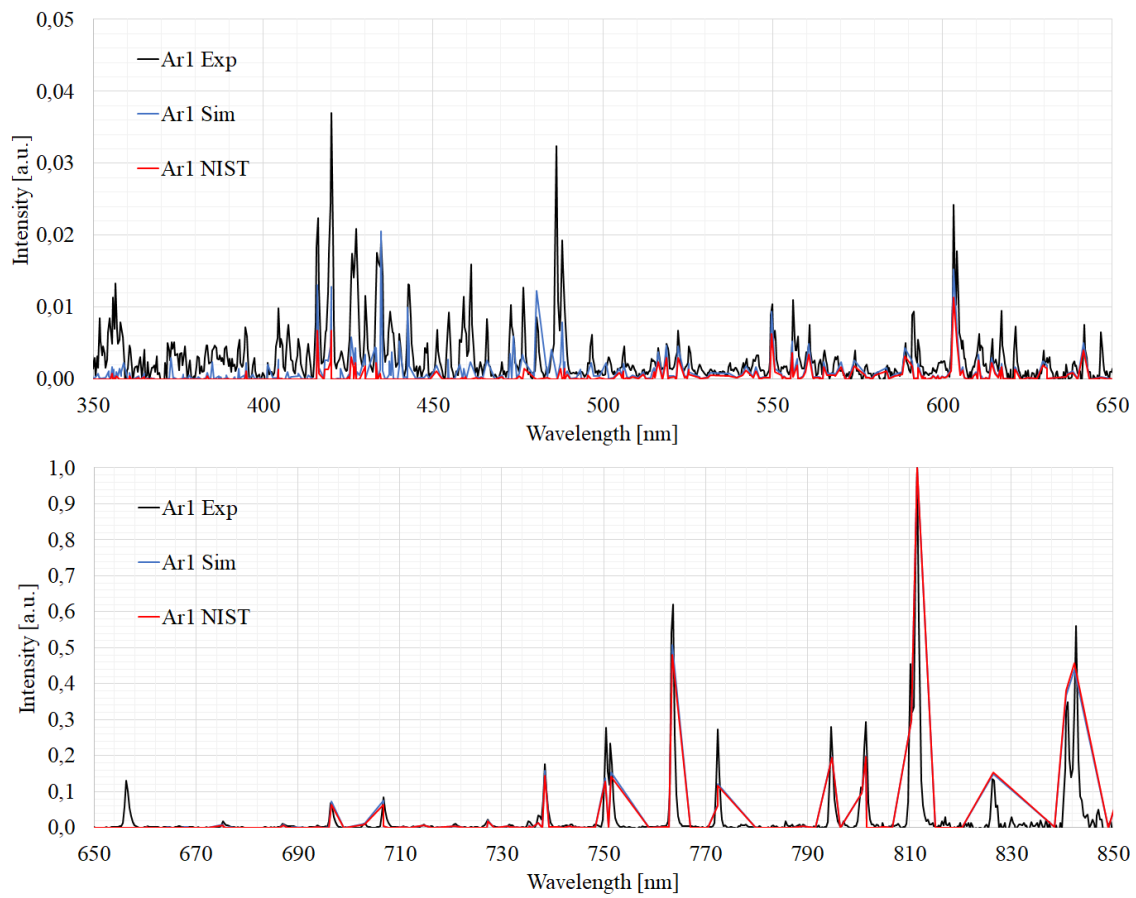
Figure 4.8.: Comparison experimental, simulation and NIST data with normalized intensities for Ar 1 in C3a at central position
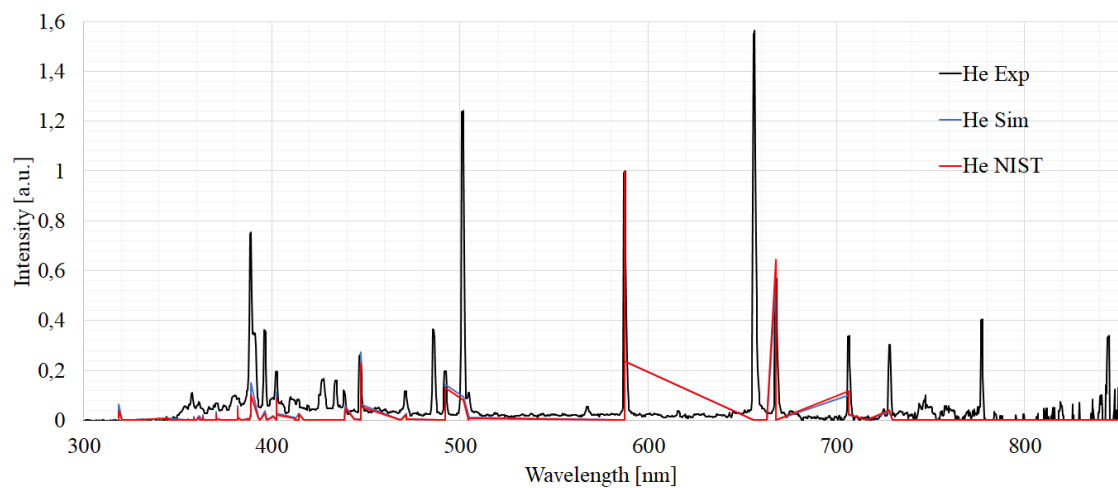
Figure 4.9.: Comparison experimental, simulation and NIST data with normalized intensities for He in C2a at central position

Table 4.5.: Particle temperatures and densities

No.	Pos.	Temperature T [K]	Electron density n_e [m^{-3}]	Neutral particle density n_0 [m^{-3}]	Singly-ionized particle density n_1 [m^{-3}]
Ar1	1.5cm	11200K (0.9651eV)	$2.1998 \cdot 10^{20}$	$2.1396 \cdot 10^{19}$	$2.1997 \cdot 10^{20}$
Ar2	1.5cm	11400K (0.9824eV)	$2.3181 \cdot 10^{20}$	$1.6369 \cdot 10^{19}$	$2.2499 \cdot 10^{20}$
Ar1	4cm	11200K (0.9651eV)	$2.1998 \cdot 10^{20}$	$2.1396 \cdot 10^{19}$	$2.1997 \cdot 10^{20}$
Ar2	4cm	10900K (0.9393eV)	$2.0964 \cdot 10^{20}$	$3.1727 \cdot 10^{19}$	$2.0964 \cdot 10^{20}$

Table 4.6.: Power losses derived from temperature and density assessment

No.	Input Power	Ionization P_{Ion}	Excitation P_{Exc}	Bremsstrahlung P_{Brems}	Ion-Grid P_{Grid}
Ar1	13.55W	0.925W	503126W	0.421W	343.3W
Ar2	124.35W	0.972W	508947W	0.444W	308.7W
He1	1.28W	0.17W	326898W	0.659W	1076.1W
He2	6.3W	0.562W	724276W	1.46W	2568.2W

Bremsstrahlung losses are depicted in Figure 4.11 and are considerably low as expected in the temperature range for the outlined experiments.

The power lost due to ion - grid collisions (Figure 4.12) is not as high as excitation, but still considerable to be disputable. An effective grid transparency was already used here, which would reduce the grid collisions. But still, a density distribution at the cathode grid (Equation (4.29)) has been assumed, that is not confirmed.
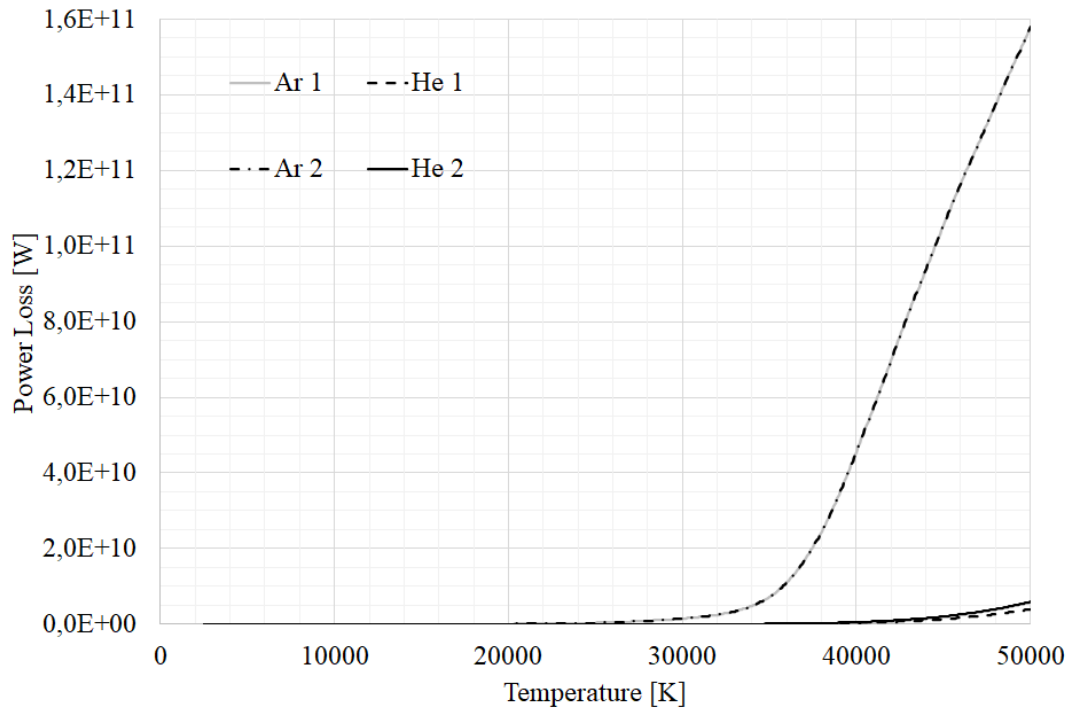
Figure 4.10.: Excitation losses: argon and helium
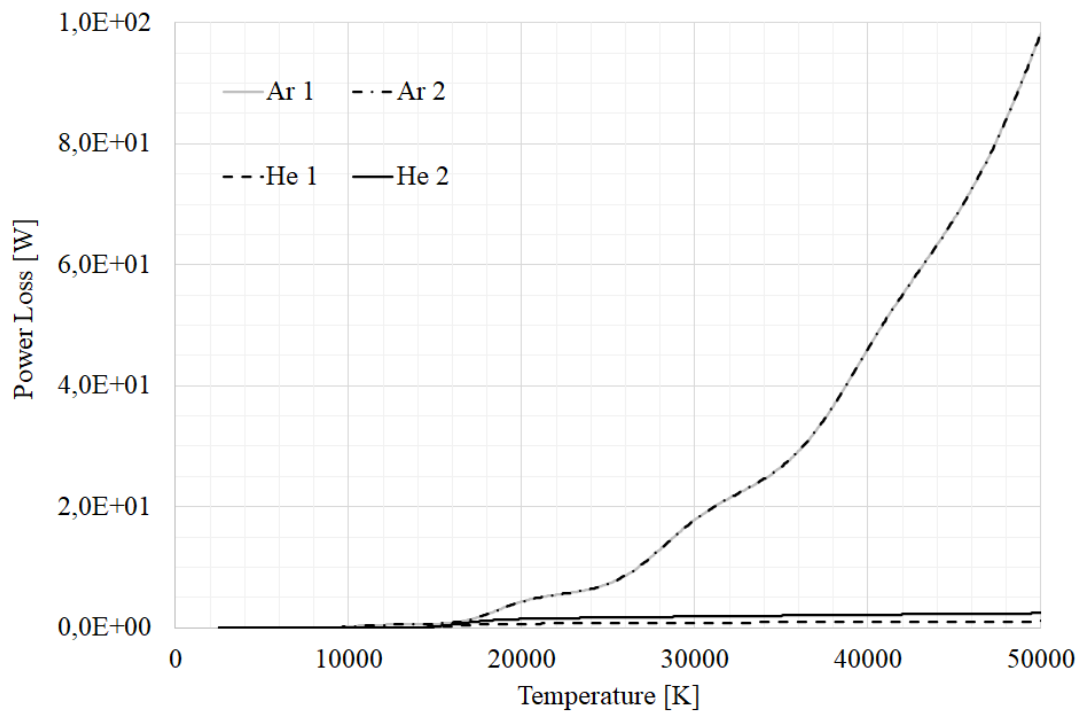
Figure 4.11.: Bremsstrahlung losses: argon and helium
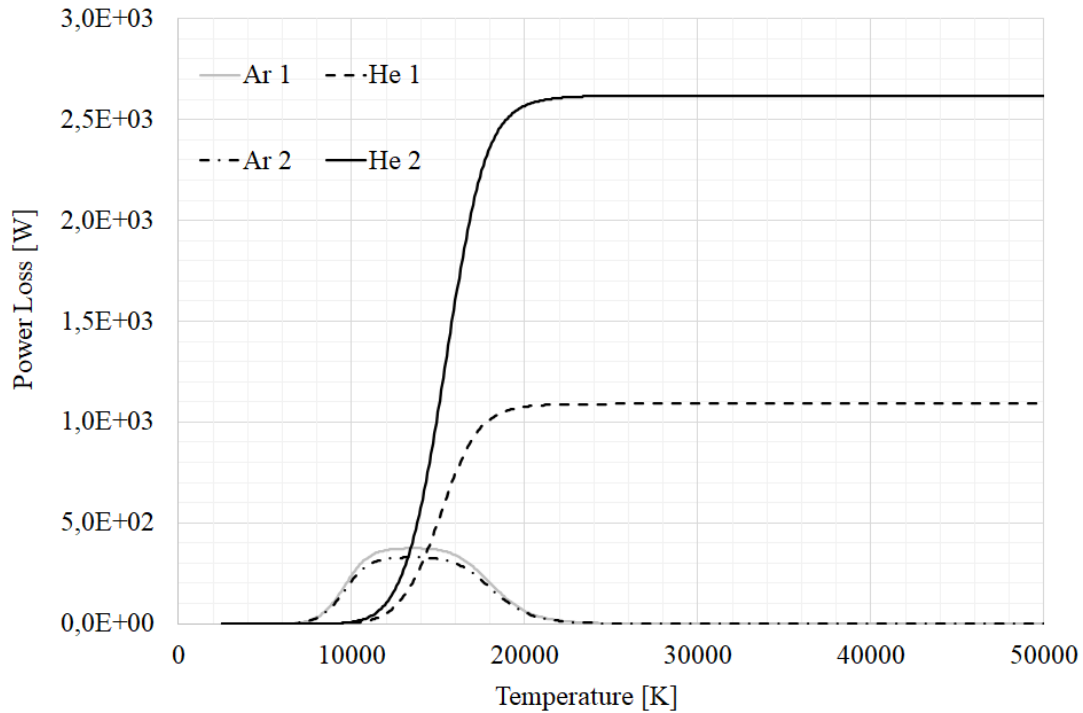
Figure 4.12.: Ion-Grid collision losses: argon and helium

4.2. Assessment of a Thrust Model for Jet Extraction

The thrust modeling approach is a direct method of assessing the thrust, apart from experimental measurements. In section 2.3 the hypotheses for the jet extraction in an IEC device were already depicted. A model based on hypotheses for the plasma acceleration after extraction is now presented. The fundamental understanding of physical phenomena is still supported by a bunch of indicators, which is why the jet was modeled as a plasma expansion by area expansion, starting with a preliminary model with simplifying assumptions which can be extended step by step. As in a neutral gas nozzle, plasma can accelerate when the cross-sectional area of the plasma increases, accelerating it from subsonic to supersonic velocity. The following conditions have been assumed for this model that has been developed by Manheimer [39]: A quasi-neutral plasma with single positively-charged ions in steady state; since the electron mass is much smaller than the ion mass, the electrons can be neglected and only the ion mass is considered in the plasma flow. Moreover, the ionization is caused by electron impact with no consideration of recombination. The pressure is assumed to be isotropic in the plasma beam and the electrons are assumed to be nearly isothermal. As long as $T_e = T_i$, is that assumption also valid for the ions. Combining the

69

continuity and momentum equation, the velocity in the region of area expansion can be assessed. Looking at the general expression of the continuity equation for a plasma (index a denoting any particle species involved) with a cross sectional area $A(x)$ and steady-state conditions for ions, the following expression is obtained

$$\frac{\delta}{\delta t}n_a + \nabla(n_a \times \vec{v_a}) = S_a \implies \frac{d}{dx}(n(x)_{e,i}v(x)_i A(x)) = S_i A(x), \qquad (4.33)$$

with v being the flow velocity. S_i presents the collision term or rather the ionization source and is given by

$$S_i = \langle \sigma_i \nu_e \rangle n_{e,i} n_n = \omega n_{e,i} \qquad (4.34)$$

where $\langle \sigma_i \nu_e \rangle = k_{ion}$ is the rate coefficient, n_n the neutral density and ω the ionization rate. The general momentum equation reduced for ions is defined as Equation (4.35), if gravitational and electromagnetic forces are neglected to contemplate only the acceleration by area expansion,

$$\frac{\delta}{\delta t}(n_a m_a \vec{v_a}) + \nabla n_a m_a \vec{v_a} \vec{v_a} + \vec{p_a} = n_a \vec{F_a} + \vec{R_a} \implies$$
$$m_i \nabla(n_{e,i}\vec{v}\vec{v}) + k_B T_e \nabla(n_{e,i}) = \vec{R_i}. \qquad (4.35)$$

Considering the pressure as isotropic in the plasma flow, the pressure tensor is $\nabla \times \vec{p} = \nabla p$ with $p = k_B n_e T_e$. The friction force $\vec{R_a}$ caused by collisions between two species j and k is expressed as

$$\vec{R_j} = \sum_j R_{jk} \approx -\sum_j m_j n_j \nu_{jk}(\vec{v_j} - \vec{v_k}), \qquad (4.36)$$

where ν_{jk} is the collision frequency between two species, but only ion collisions are considered relevant. Assuming that the ions are produced at zero velocity, $\vec{R}$ reduces to

$$\vec{R_i} = -m_i n_{e,i} \nu_i \vec{v_i}. \qquad (4.37)$$

With an expression for $\nabla(\vec{v}\vec{v}) = (\vec{v} \times \nabla)\vec{v} + \vec{v}\nabla \times \vec{v}$ the momentum equation Equation (4.35) can be rearranged giving the following expression in 1D:

$$m_i \left(n_{e,i}(x)v(x)\frac{dv(x)}{dx} + v(x)\frac{d}{dx}(n_{e,i}(x)v(x)) \right) =$$
$$-k_B T_e \frac{dn(x)}{dx} - m_i n_{e,i}(x)\nu_i v(x). \qquad (4.38)$$

The term $\frac{d}{dx}(n_{e,i}(x)v(x))$ in Equation (4.38) can be replaced by the continuity equation (Equation (4.33)). If the ionization source (Equation (4.34)) is added, Equation (4.38) becomes

$$m_i v(x)\frac{dv(x)}{dx} = -\frac{k_B T_e}{n_{e,i}(x)}\frac{dn(x)}{dx} - m_i(\nu_i + \omega)v(x). \qquad (4.39)$$

Looking at Equation (4.39) the term $\frac{dn(x)}{dx}$ still needs to be replaced. Using Equation (4.33) and converting it to

$$\frac{dn(x)}{dx} = \frac{S_i - n_{e,i}(x)\frac{dv(x)}{dx}}{v(x)} - \frac{dA(x)}{dx}\frac{n_{e,i}(x)}{A(x)}, \qquad (4.40)$$

substituting that term in Equation (4.39) leads to a differential equation for the plasma flow velocity depending on the area, ion mass, electron temperature and collisional terms,

$$\frac{dv(x)}{dx} = \frac{m_i v(x)^2(\nu_i + \omega) + k_B T_e \left(\omega - v(x)\frac{dA(x)}{dx}\frac{1}{A(x)} \right)}{k_B T_e - m_i v(x)^2}. \qquad (4.41)$$

This differential equation becomes singular if the denominator becomes zero: $k_B T_e - m_i v(x)^2 = 0$. Solved for $v(x)$ this equals exactly the ion sound velocity with an adiabatic index of $\gamma = 1$ and charge state of $Z_i = 1$,

$$v(x_s) = \sqrt{\frac{k_B T_e}{m_i}} = c_s = \sqrt{\gamma Z_i \frac{k_B T_e}{m_i}}, \qquad (4.42)$$

with x_s marking the spatial position where the plasma reaches ion sound velocity. Therefore, one boundary condition to solve Equation (4.40) is $v(x_s) = c_s$. If the nominator becomes also zero at the ion sound velocity, the singularity at x_s can be solved, leading to the following expression:

$$c_s \frac{dA(x_s)}{dx}\frac{1}{A(x_s)} = \nu_i + 2\omega. \qquad (4.43)$$

With this equation the position x_s in the jet can be calculated, but first a solution for Equation (4.41) at x_s is required. At x_s the velocity equals c_s, but inserting this into Equation (4.41) leads to an undetermined expression,

$$\left.\frac{dv(x)}{dx}\right|_{x_s} = \frac{c_s^2(\nu_i + \omega) + c_s^2 \left(\omega - c_s \frac{dA(x_s)}{dx}\frac{1}{A(x_s)} \right)}{c_s^2 - c_s^2} = \frac{0}{0}. \qquad (4.44)$$

Applying the rule of L'Hospital to Equation (4.41) leads to a quadratic function

$$\begin{aligned} \left(\left.\frac{dv(x)}{dx}\right|_{x_s} \right)^2 - \left[\frac{c_s}{2} \left. \left(\frac{dA(x)}{dx}\frac{1}{A(x)} \right) \right|_{x_s} - \nu_i - \omega \right] \left.\frac{dv}{dx}\right|_{x_s} \\ - \frac{c_s^2}{2}\frac{d}{dx} \left. \left[\frac{dA(x)}{dx}\frac{1}{A(x)} \right] \right|_{x_s} = 0. \end{aligned} \qquad (4.45)$$

For simplifications the first derivative $\frac{d}{dx}$ is marked with a prime $(')$ and the expression $\left[\frac{dA(x)}{dx}\frac{1}{A(x)} \right]$ is substituted by $z(x)$,

$$v'(x_s)^2 - \left(\frac{c_s}{2}z(x_s) - \nu_i - \omega \right) v'(x_s)\frac{c_s^2}{2}z'(x_s) = 0. \qquad (4.46)$$

This expression can be used to obtain a second boundary condition to solve Equation (4.41). With Equation (4.43) the solution reduces to

$$v'(x_s) = \frac{1}{4}\left(\sqrt{8c_s^2 z'(x_s) + \nu_i^2} - \nu_i\right). \tag{4.47}$$

With Equation (4.42) and Equation (4.47) giving boundary conditions, the plasma velocity can be determined by integrating Equation (4.41) in both directions starting from the sonic point. The relevant velocity for propulsion applications is the velocity at the anode grid. Therefore, it is reasonable to integrate from the sonic point, which should be somewhere between cathode and anode, to the anode grid which is the jet exhaust. This differential equation has to be solved numerically.

4.2.1. Solution Approach

In principle, every area function can be selected to solve Equation (4.41), but the gradient of v at the sonic point has to be a real number. With respect to Equation (4.47) that means

$$z'(x_s) \geq -\frac{\nu_i^2}{8c_s^2}, \tag{4.48}$$

otherwise $v'(x_s)$ is an imaginary number. Reinserting $z(x)$ in Equation (4.48) gives

$$-\frac{A'(x_s)^2 - A(x_s)A''(x_s)}{A(x_s)^2} \geq -\frac{\nu_i^2}{8c_s^2}. \tag{4.49}$$

It is evident, that the term on the left hand side has to be positive and therefore $z(x_s) = \frac{A'(x_s)}{A(x_s)}$ has a positive gradient. Moreover, the sonic point which can be determined using Equation (4.43) has to be a real number as well. Using the geometry of a conical jet, the dimensions depicted in Figure 4.13 are relevant. Generally, the area of a cross section profile can be defined as

$$A(r_{jet}(x)) = \pi r_{jet}^2(x) = \pi\left(\left(\frac{r_{A,jet} - r_{C,jet}}{r_A - r_C}\right)(x - r_C) + r_{C,jet}\right)^2 \tag{4.50}$$

with

$$r_{jet}(x) = tan\left(\frac{\beta_{jet}}{2}\right)(x - r_C) + r_{C,jet} \tag{4.51}$$

and

$$\beta_{jet} = 2arctan\left(\frac{r_{A,jet} - r_{C,jet}}{r_A - r_C}\right). \tag{4.52}$$

Combining Equation 4.43 and Equation 4.51, the position of x_s in the IEC jet can be calculated by

$$x_s = \frac{2c_s}{\nu_i + 2\omega} + \frac{r_{A,jet}r_C - r_A r_{C,jet}}{r_{A,jet} - r_{C,jet}}. \tag{4.53}$$
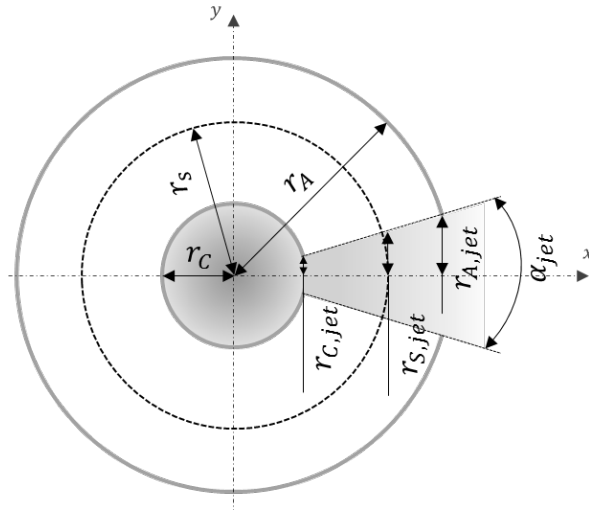
Figure 4.13.: Dimensions of a conical IEC jet

Apart from the geometry, ionization processes have an influence on the sonic point as well. As stated above, ionization is caused by electron impact. Using Argon as fuel, the ionization rate coefficient defined by Lotz [46] in Equation (4.20) is used, with the first ionization energy (see Table 4.1) and $\zeta = 6$ the number of valence electrons. Having the neutral density n_n with this function, the ionization rate ω can be determined by Equation (4.34). The ion collision frequency ν_i can be assessed by [39]

$$\nu_i = 10^{-15} \left(\frac{T_i k_B}{e} \right)^2 n_n. \tag{4.54}$$

The parenthesized term is the thermal ion energy. Since the energy is not known, ion and electron temperatures are assumed to be equal.

4.2.2. Results

For the following calculation, these input parameters are necessary: T_e, n_H and $T_e = T_i = T_{e,i}$ and $n_e = n_i = n_{e,i}$ applies with a neutral particle temperature of $T_n = const$ and an ionization degree of α with

$$\alpha = \frac{n_{e.i}}{n_n + n_{e,i}}. \tag{4.55}$$

In section 4.2.1 the general geometry of a conical jet has been discussed. For simulations a specific design is needed. The design of configuration C3a will be used having five latitude and eight longitude wires. The cross-sectional area of the jet is assumed to be a fraction

of the grid opening β. With this data the jet radius at anode and cathode is

$$r_{C,jet} = r_C \sqrt{\frac{1}{12} \cdot \beta} \qquad \text{and} \qquad r_{A,jet} = r_A \sqrt{\frac{1}{12} \cdot \beta}. \tag{4.56}$$

Adding these ratios to Equation 4.53 for a conical jet leads to

$$x_s = \frac{2 \cdot c_s}{v_i + 2\omega}, \tag{4.57}$$

showing the sonic point to be independent of the IEC geometry. Thus, the sonic point can be determined at any temperature with the previous mentioned assumed plasma conditions. Knowing that the sonic point is independent of the IEC geometry, specifically cathode and anode radius, the design can be chosen according to the maximum acceleration output. There are two approaches to be considered:

- The cathode radius r_C can be set at the minimum sonic point. If all temperatures are considered, the sonic point shifts from the cathode radius through the nozzle to the anode exit.

- The second variant configures the IEC design in a way that for every temperature the cathode radius is at the position of the sonic point. For this variant the cathode radius is fixed at the sonic point which varies for every temperature point. The velocity will always reach its maximum at the anode exit due to a maximum acceleration distance.

Considering the first approach with r_C at $x_{s,min}$ the following procedure is used. The jet area can be determined with Equation (4.50) and (4.51). For the velocity determination, the ionization frequency follows from Equation (4.34) and (4.20) giving ω and with Equation (4.54) the ion-ion collision frequency ν_i. The sonic velocity is c_s according to Equation (4.42) and the sonic point at x_s with Equation (4.57) positioned in the interelectrode space. Knowing that the sonic point can be solved by numerical integration from x_s to r_A, the requirements Equation (4.48) and (4.49) have to be checked. Solving Equation (4.49) shows that this condition is not valid, followed by an imaginary velocity gradient at the sonic point. From the equations it is evident that the velocity gradient becomes always negative for the conical jet contour. Independent of cathode radius, anode radius or sonic point, $z\prime(x)$ will always be negative (Figure 4.14). Nevertheless, three approaches could be identified to obtain a solution:

1. collision terms ω and ν_i are neglected beyond x_s, inherently assuming plasma collisions will reduce anyway due to the plasma expansion,

2. the sonic point is at the anode exit,

3. or an approximated profile is used which gives a positive $z\prime(x)$.
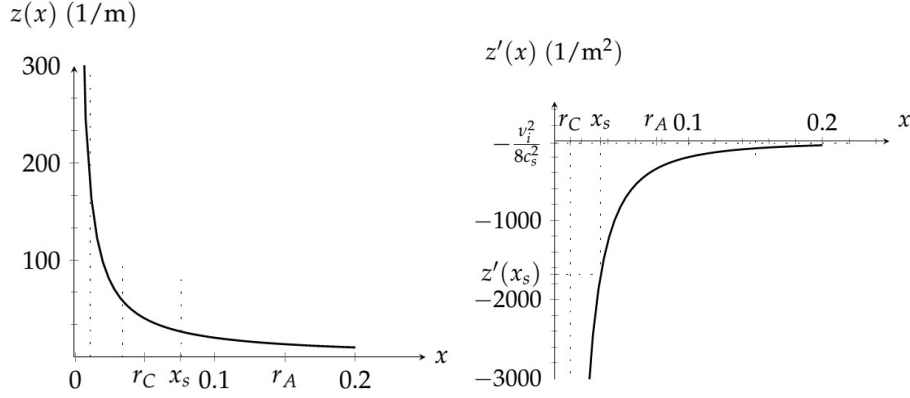
Figure 4.14.: Derivative functions of conical profile [19]

1. Conical Jet Profile, No Collisions

Neglecting collisions in the velocity determination Equation (4.41) reduces to

$$\frac{dv}{dx} = \frac{-k_B T_e v(x) \cdot \frac{dA}{dx} \frac{1}{A}}{k_B T_e - m_i v^2},$$
(4.58)

and can be integrated from the sonic point x_s to $x(x > x_s)$ leading to

$$\frac{1}{2}\frac{m_i}{k_B T_e}v(x)^2 - \frac{1}{2}\frac{m_i}{k_B T_e}c_s^2 - ln\left(\frac{v(x)}{c_s}\right) = ln\left(\frac{A(x)}{A_s}\right).$$
(4.59)

Three design configurations are considered for the following calculations:

- $r_C = x_{s,min}$ (fixed grid radii),

- $r_C = x_s$ (variable grid radii),

- $r_A = x_s$ (variable grid radii),

with a fixed electrode surface ratio A_A/A_C. For the latter configuration the sonic velocity is always the exhaust velocity. Figure 4.15 shows a plot of the exhaust velocities for the different configurations with an example set of operation parameters. The highest exhaust velocity is found with the second configuration as expected. The maximum length of acceleration is provided here.
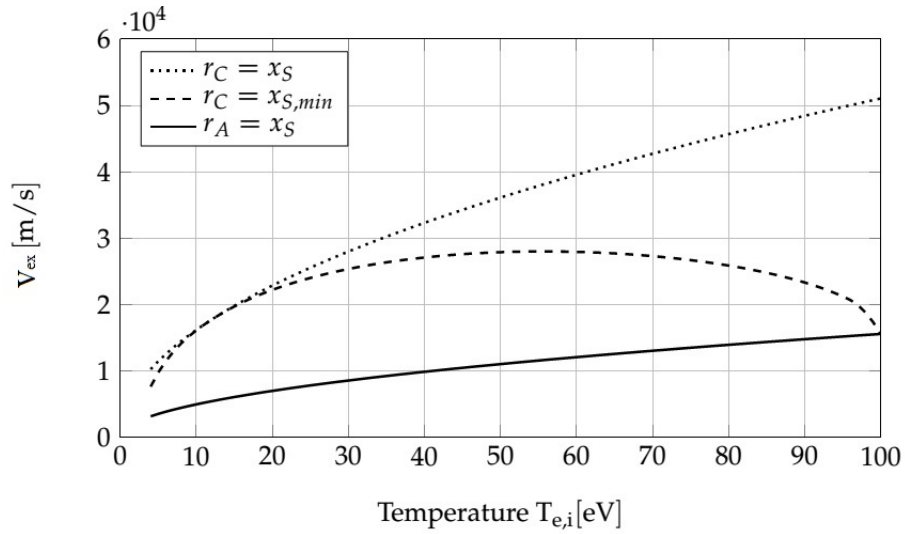
Figure 4.15.: Ion velocities ($\alpha = 0.1, T_n = 300K, A_A/A_C = 42.42, \alpha = 0.3$) [19]
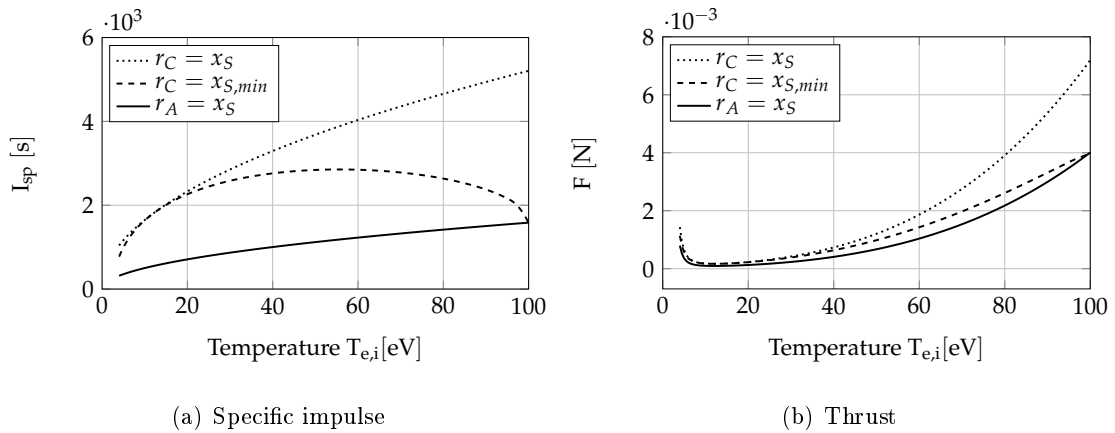
(a) Specific impulse

(b) Thrust

Figure 4.16.: Ion velocities ($\alpha = 0.1$, $T_n = 300K$, $A_A/A_C = 42.42$, $r_C = 1.17cm$, $r_A = 7.62cm$, jet area ratjo=0.3, $n_n = 3 \cdot 10^{19}m^{-3}$ and $T_{e,i} = 4eV$) [19]

Derived from that, the I_{sp} can be calculated shown in Figure 4.16a. The thrust, can be determined with the ion and electron pressure at the exhaust. The ion pressure is defined as

$$p_{i,ex} = \frac{m_i v_{ex} n_{i,ex}}{A_{ex} t} = n_{i,ex} m_i v_{ex}^2, \tag{4.60}$$

with $A = V/x$ and $v = x/t$. The electron pressure is assumed to be isotropic with

$$p_{e,ex} = n_{e,ex} k_B T_e, \tag{4.61}$$

leading to the total jet pressure by adding up. Integrating the continuity equation from sonic point to exhaust leads to

$$\int_{A_s}^{A_{ex}} \frac{1}{A} dA \int_{c_s}^{v_{ex}} \frac{1}{v} dv \int_{n_s}^{n_{ex}} \frac{1}{n} dn = 0 \rightarrow n_{ex} v_{ex} A_{ex} = n_s c_s A_s. \tag{4.62}$$

Here, n is the plasma density assuming quasi-neutrality $n = n_e + n_i = 2n_{e,i}$. The thrust can then be obtained using $c_s^2 = k_B T_e / m_i$ and $v_{ex} = \chi \cdot c_s$ with the factor χ by the following expression

$$F = A_s k_B T_e 2 n_{e,i} \left(\chi + \frac{1}{\chi} \right). \tag{4.63}$$

The thrust is illustrated in Figure 4.16b for the three configurations.

2. Approximated Jet Profile, Including Collisions

A second solution for the differential equation is presented by including constant collision terms but using an approximated profile. The jet profile is approximated by an exponential function (Equation (4.64)) depicted in Figure 4.17a.

$$r(x) = a + be^{cx}, \tag{4.64}$$

where a, b, c are constants with $0 < a < 1$, $0 < b < 1$ and $0 < c$. The $z\prime(x_s)$ (Equation (4.48)) and the velocity gradient at the sonic point $v\prime(x_s)$ are positive as illustrated below (Figure 4.17b). As mentioned, this profile has to be adapted for every temperature. A temperature variation showed that if the term $(\nu_i + 2\omega)/c_s$ is small, which means considering temperatures $< 100 eV$, the exponential function is less bended and fits better to the conical profile. Figure 4.18 shows the velocity evolution from the sonic point to the exit plane. Results show that the velocities derived by the solution including collision terms are lower than those neglecting collisions. This is plausible, but this method shows only one result, since the jet profile is only an approximation and the e-function has to be adapted for every temperature.
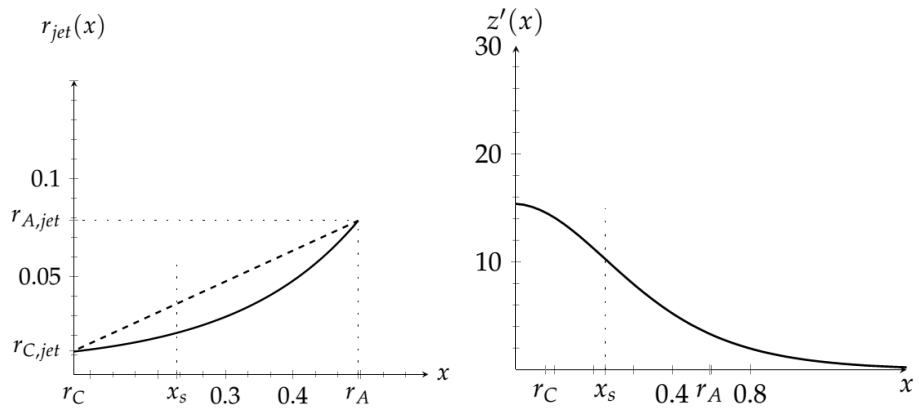
(a) Jet radius of approximated jet profile (solid) and conical jet profile (dashed)

(b) Derivative function of approximated profile

Figure 4.17.: Derivative functions of approximated profile
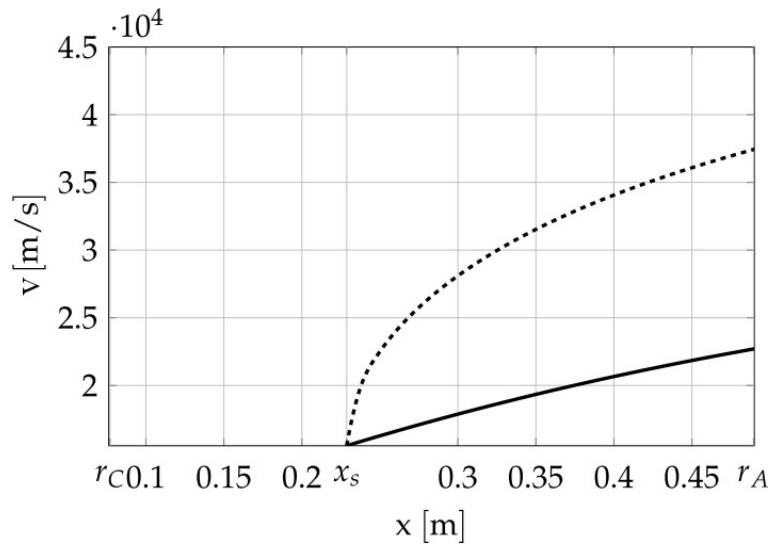
Figure 4.18.: Velocity as a function of the jet path (conical, no collisions - dashed, e-function, incl. collisions - solid), $\alpha = 0.1$, $T_n = 300K$, $A_A/A_C = 42.42$, $r_C = 7.62cm$, $r_A = 49.65cm$, jet area ratio=0.3, $n_n = 1 \cdot 10^{19}m^{-3}$ and $T_{e,i} = 100eV$) [19]

4.3. Conclusion Plasma Modeling

The following can be stated in order to summarize the efforts and planned improvements for both approaches:

1. A loss model, approaching the amount of energy left in the system for thrust generation, has been tested in terms of sensitivities and applicability for power estimation using also experimental data sets as input parameters. Bremsstrahlung losses and particle-grid collisions have been implemented and verified for fusion propellants and are also applicable to argon and helium. Ionization and excitation losses were compared to other databases (NIST) but only limited consistency has been observed. Comparison of simulations and experiments also revealed deviations, so that this assessment can only be called preliminary and the electron energy distribution function needs to be confirmed. The following table shows a summary of assumptions for the implemented models:

Table 4.7.: Model based assumptions

Model	Assumption
particle density solver	local thermal equilibrium (atoms adopt state population given by Boltzmann, radiation is not necessarily thermal)
	Maxwellian velocity distribution f(v) for electrons
ionization power	general equilibrium model of rate coefficients, exist no matter what kind of shape f(v) has (coefficients are used when statistical thermodynamic arguments do not apply)
excitation power	statistical density distribution of two possible quantum states in thermal equilibrium (Boltzmann)
Bremsstrahlung radiation	includes nonrelativistic and extreme relativistic limits for electron-ion and electron-electron bremsstrahlung, interpolation to obtain radiation rates in intermediate regime
Ion-Grid / Electron-Grid Collisions	single potential well for charge carrier distribution within cathode

The following other assumptions need to be verified or investigated with respect to their impact and if necessary, they have to be adapted:

a) Non-Maxwellian electron energy distribution: There are two energy distributions that are commonly applied, which are the Dryvesteyn and Maxwell EEDF. In case of a Dryvesteyn function elastic collisions dominate, which in turn means that inelastic collisions as in ionization and excitation processes do not play the major role as for a Maxwellian plasma where inelastic collision dominate. The underlying EEDF for the models presented herein is the Maxwell distribution function. However, comparison of experimental and simulation data, showed considerable deviations especially for intensities of ionized particle transitions. Based on that, it is likely that the EEDF in an IEC confinement deviates from Maxwell, which in turn means that the ionization degree could be an overestimate, if low temperature collisions are more important than assumed with Maxwell. Nevertheless, what makes these discussions even more critical is the fact, that the particle energy distributions (electron, ion and neutral) depend on the particle's original birth region in the system [24].

b) Non-equilibrium energy distribution: A partial thermodynamic equilibrium allows for different temperatures of electrons and heavy particles. In that context the assumption of $T_e > T_i$ and $T_i = T_H$ enables an estimate of the ratio T_e/T_H [50].

c) A time derivative of populations should be implemented and tested, if the population of states is not in equilibrium. The time span for relaxation to an excited state equilibrium is shorter than for relaxation to ionization stage equilibrium. This could explain why ionized stages are not adequately represented in the simulated spectra and excitation losses in the measured spectrum are higher in the lower wavelength range ($< 500nm$).

d) Implementation of nitrogen as propellant will require the extension to dissociation losses. Higher ionization levels (E_i for $i = 2$) for helium should be implemented and accessible in this simulation tool. Both means would allow a more comprehensive check on plausibility of the assumptions used in all models as well.

2. A 1-dimensional thrust model describing plasma acceleration by plasma expansion has been implemented. A solution for the velocity differential equation for a conical jet profile neglecting collisions has been used. A preliminary assessment of thrust and

specific impulse (I_{sp}) was derived. The sensitivity analysis was performed for the case of a conical jet without collisions [19]. Plasma properties as n_H, α and jet constriction were varied for the case $r_C = x_s$. The variation of the jet cross-sectional area from 0.1 to 0.6 has only an influence on the thrust. Considering Equation (4.63) which includes A_s, it is evident that the thrust increases with increasing cross sectional area. Changing the ionization degree from 0.05 to 0.5 has an influence on the sonic point, but this impact is almost negligible in temperature regions of $T_{e,i} < 100eV$. Since the ionization degree is directly affecting the ion and electron particle density, there is also an effect on thrust. Higher ionization degree means higher thrust. The neutral particle variation shows a great impact on the sonic point; the lower n_H, the greater x_s and only the thrust is affected but not the I_{sp}. A preliminary assessment of solving the velocity differential equation with an approximated exponential function profile including collisions (electron impact ionization and ion-ion collisions) was presented. But here, an adjustment of this e-function for every plasma condition is necessary. An assessment implementing decreasing collision terms along the jet axis with increasing jet broadening has been presented, which is not part of this thesis. Additional points to be discussed or improved are:

a) A thermal non-equilibrium should be implemented allowing $T_i \neq T_e$, which is relevant for the implementation of the mechanism ambipolar diffusion and expansion based temperature decrease.

b) The current model only includes the first ionization stage with $n_e = n_i = n_{e,i}$. With higher operation powers this level will not be sufficient.

c) Other propellants: helium and nitrogen should be implemented and accessible in this simulation tool. This would allow a more comprehensive check on plausibility of the model assumptions as well.

The overall conclusion is that the additional consideration of particle models helped a lot in the understanding of processes on microscopic level and the link to the macroscopic level has been established. The loss model has been derived for a better understanding of the general confinement methods and its efficiency, also giving output parameters that in turn can be input parameters for the thrust model. In that way macroscopic input parameters can be linked to microscopic output/input parameters that will in the end lead to general propulsion characteristics such as thrust and I_{sp}. The most useful chain

in terms of linking experimental data to numerical data for thrust and I_{sp} assessment has been depicted in Figure 4.19.
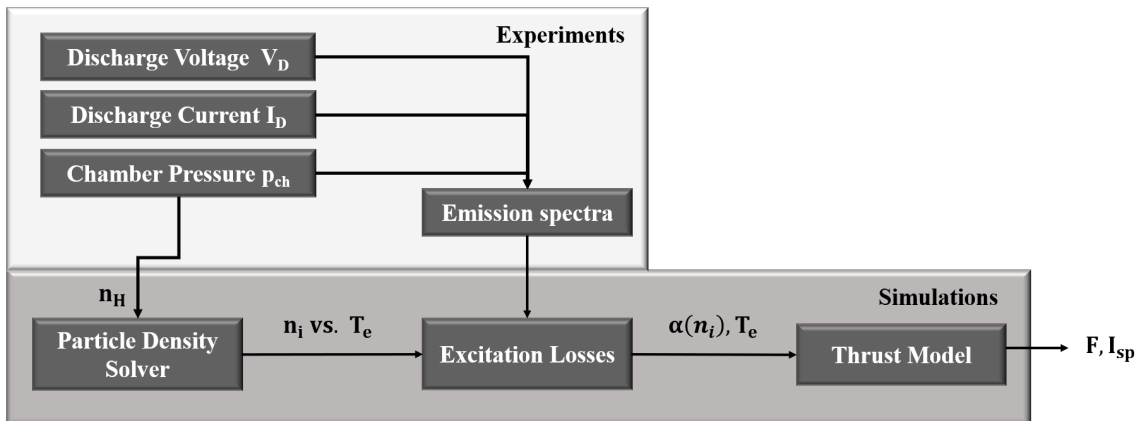

Figure 4.19.: Chain of experiments and simulations to obtain thrust and I_{sp}

This chain starts with macroscopic operation parameters (V_D, I_D, p_{ch}). Then the heavy particle density, which is a microscopic parameter, has been derived from the chamber pressure to be a start input parameter for the particle solver that has particle density distributions depending on the electron temperature as output parameter. In combination with an additional diagnostic technique (OES), simulation data can be fitted to experimental data, that results into a particle distribution at a specific temperature, which is an input parameter for the thrust model that in the end delivers a thrust for the IEC operation parameters. In this thesis it was not possible to calculate the potential I_{sp} and thrust from the experimental data (derived in section 4.1.6), because the fit of excitation data revealed an ionization stage above the first ionization level. Therefore, an exemplary operation condition has been used as test case. As part of these considerations also uncertainties, that are inherent to the simulation results due to uncertainties in experimental data, have to be analyzed. The heavy particle density for the numerical Saha solver can be set equal to the neutral particle pressure which has been derived from the chamber pressure for open IEC systems. However, for the IEC setup used at IRS the pressure gauge is about $1.5m$ far away. But the influence of an inhomogeneous pressure distribution is considered low for the heavy particle density assessment.

The other models derived for ionization and Bremsstrahlung give an idea on how dominant these processes are at the same temperature. It was assumed that Bremsstrahlung will only be relevant at power levels necessary to operate IEC fusion devices, but seem to be more relevant than expected even if they are low. That ion-grid collisions are a

major contributor is not surprising. That is the case for all gridded ion accelerator devices. However, more work needs to be done to assess the electron density distribution at the cathode grid. This would be feasible with OES, through the same fitting approach that has been used to assess the particle properties at the center of the confinement, but is not logical as long as the EEDF has not been verified yet.

5. Conclusion Applicability for Space Propulsion

Whether the Inertial Electrostatic Confinement device can be used for space propulsion applications on spacecrafts, needs to be evaluated with respect to characteristic parameters such as thrust F, specific impulse I_{sp} and efficiency. At this point, specific features such as a combination of IEC electric propulsion with a fusion mode, a RAM-IEC-EP device or an EP-device with active thrust vector control are not considered, but a conventional EP device which can be enhanced with the aforementioned features. These characteristic parameters are expressed as:

$$F = \dot{m} \cdot v_{ex} \tag{5.65}$$

$$I_{sp} = \frac{v_{ex}}{g_0} \tag{5.66}$$

with the gravitational acceleration g_0. The mass flow is usually considered an input parameter for the EP device and v_{ex} an output parameter. Both parameters determine the applicable mission phase for an EP device. Generally, the following classifications exist:

- High Thrust: Continuous Operation (Orbit Raising, Cruise)

- High I_{sp}: Station Keeping.

As mentioned in the introduction section, the assessment of propulsion parameters can be achieved by test, simulation or a combination of both. In both cases, macroscopic parameters, e.g. pressure, discharge voltage and current, and microscopic parameters such as particle temperatures and densities are needed to characterize the technology and understand the underlying phenomena. A thrust measurement would give answers to thrust and I_{sp} right away. However, that would require a jump from a fusion power device to an EP prototype right away. In this case, without being able to ensure an adequate design and understanding of operation (modes and physical processes). For IEC devices, the mass flow and particle exit velocity need to be known at the cathode opening in order to assess thrust and specific impulse. Both parameters cannot be measured or gained through simulations easily.

5.1. Functional Principle

The different phases plasma generation, extraction and acceleration have been identified and described now, partially confirmed by experiments or supported by simulations, partially still being hypotheses. And similarities to conventional electric propulsion systems are apparent.

- Plasma generation: This process, i.e. electron impact ionization by glow discharge, takes place in the inter-electrode space and generated ions are accelerated into the cathode. Additional ionization due to interaction with the cathode grid and background gas leads to occurrence of electrons and further ions in the cathode volume.

- Plasma extraction: The high negative potential at the cathode grid provokes that ions and electrons will not leave the cathode inside. Virtual electrodes are built up. The enlarged grid opening weakens the confinement at this position and enables the escape of electrons which in turn can drag ions along. This process is called ambipolar diffusion.

- Plasma acceleration: It is assumed that the potential difference between grids does not play a role in ion acceleration due to the reverse polarization. That in turn indicates, that the acceleration process is triggered by the same mechanism, that enables the extraction or additional processes, which can be covered by e.g. plasma expansion.

These phases can also be identified for Hall-Effect thruster (HET) and Gridded-Ion engines (GIE) [51]. For HETs, plasma generation is accomplished by electron impact ionization in a static magnetic field, plasma extraction and acceleration by a potential difference between anode and an electron cloud at the thruster exit. For GIEs, plasma generation is established with electron impact ionization enabled by hollow cathodes or radio-frequency generators, plasma extraction by the so-called screen grid and plasma acceleration by the potential difference between screen and accelerator grid.

From its appearance, species composition and discharge characteristic, the tight jet mode is the relevant mode for thrust generation. With the transition from tight to spray jet mode, the current is not extracted out of the grid system anymore. Experiments showed that a plasma bulk bursts out of the confinement area through the cathode opening and results into the spray shaped discharge between the grids. The hypothesis explaining this

transition assumes, that due to increasing input power the particle densities within the cathode also increase and virtual electrodes build up until at a certain point the confinement cannot be sustained anymore. For that reason, the *spray* mode will not be considered for the further analysis.

5.2. Plasma Properties and Thruster Characteristics

The parameters characterizing the IEC can be divided into macroscopic and microscopic. Macroscopic parameters, defined as operation parameters, are operation pressure/mass flow, discharge voltage and current and microscopic parameters are particle properties as velocities, energies, densities and temperatures. Starting from this and considering the open IEC device (anode is a spherical grid), as it has been tested and analyzed at IRS, it is characterized by the operating pressure, not by a global mass flow to feed the device. Even with a closed anode (only one opening for the jet) and an access port for the propellant, the ion extraction current which is generating thrust, should be assessed at the cathode directly. Due to that it would be necessary to measure the extracted ion current at the cathode opening. The ion current can be assessed with Faraday cups at the cathode exit. However, this is an intrusive measurement technique, that can alter the electric field shape at the cathode grid due to the fact, that the probe will be biased to attract ions and repel electrons. The probe measures ion or electron current per area depending on the bias potential. Knowing the probe surface, the ion current can be determined which is defined as charge per second. Having only singly-charged ions in the beam, which has been proofed by OES measurements, the particle number per second can be retrieved, which allows to determine the mass flow. The exit velocity can be assessed with Time-of-Flight probes (Langmuir probe), Retarding Potential Analyzer and ExB probes. All these measurement techniques depend on electrostatic biasing that can alter the electric field shape of the grid system. Langmuir probes adapted to flight time measurements also need a disturbance or characteristic, that can be recorded at two measurement points separated by a known distance. The retarding potential analyzer (RPA) allows to assess the ion energies distribution, but does not distinguish between different ionization level. The ExB probe is a velocity selective probe, that can distinguish between ionization level and assesses the particle velocity. Alternatively, these probes can be placed in the beam outside of the grid system (see Figure 5.1). In that case it is assumed that the beam background gas
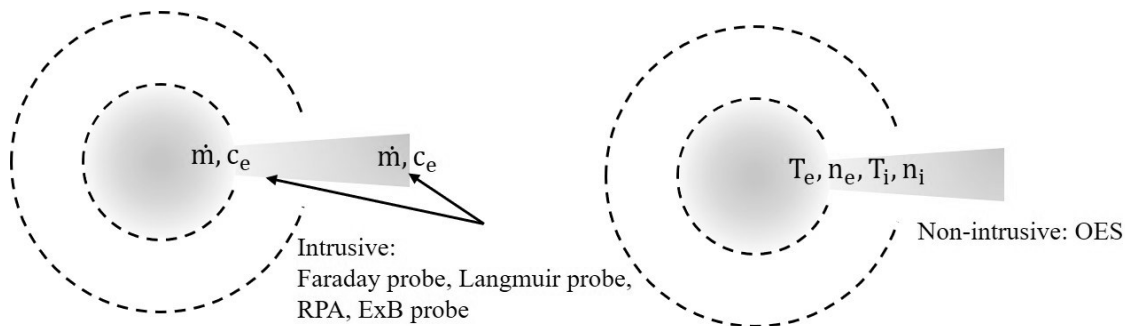
Figure 5.1.: Intrusive and non-intrusive measurement techniques

interaction has no impact on the beam properties. Simulations of the effects on the electric field when a biased probe is inserted into the grid system could give hints which position is the closest with no effect on the discharge behavior, which can also be confirmed by test. However, the starting conditions for this research were different so that only indicators existed that the jet actually consists of accelerated ions. The plasma extraction and acceleration process was investigated in a first step with a simulation study (PIC) with a simplified confinement setup [18] and input data from a literature research. A detailed simulation of the confinement with a combination of PIC, DSMC and Fokker-Planck solver including parameter studies with particle weight, mesh cell size and time step would require a distinct amount of work, followed by simulations with a jet extraction in order to ensure an adequate implementation enabling an evaluation of physical plausibility. This detailed study should be part of future investigations so that the jet properties gained in simulations may be compared to diagnostic measurements in the jet outside of the grid system.

The focus of this work was laid on a different approach to gain more fundamental understanding of the processes in the confinement and jet first. Optical emission measurements, which are not intrusive were feasible due to the fact that an open IEC device was used and revealed the species composition in confinement and jet showing the existence of singly-charged ions in both jet modes. However, the origin of these ions it not known. It is also supposable that the jet consists mainly of electrons which ionize the background gas on its way out of the grid system. These would not contribute much to thrust generation. For that reason, a direct thrust measurement will be useful. The IEC plasma models of loss assessment for the general IEC confinement and thrust generation for a jet were set up in order to separate confinement and jet extraction. This also implies simplifications as the

disregard of loss mechanism of e.g. grid collisions and additional ionization of background gas due to jet particles. Ionization power can be estimated as well as Bremsstrahlung power losses, showing the operation range where Bremsstrahlung becomes dominant. Collisional losses as particle-grid collisions with respect to power loss have been assessed. For lifetime analysis dedicated tools should be used that do not only estimate the amount of particles lost due to these processes but also give geometric data of material loss at the cathode grid. In addition, charge exchange reactions can be relevant for erosion processes. Having considerable discharge chamber pressures, these reactions can be dominant resulting into slow ions and fast neutrals. The excitation process has been used to apply OES measurements and estimate electron temperatures and densities by assuming an EEDF. This approach allows an assessment of input parameters for the thrust model on microscopic level. As already mentioned, the electron energy distribution function needs to be reviewed and also measured directly, which will increase confidence on the thrust and I_{sp} calculations, that rely on input parameters as temperatures and densities. Concluding from this, the technology readiness level 3 (characteristic proof-of-concept) has been reached for this technology by combining a profound database of experimental data with models for thrust, I_{sp} and power losses that have been partially validated.

A. Appendix

Accuracy Analysis

All diagrams shown before inherit an error analysis for the presented operation and design parameters. The following Table A.1 shows the assessment.

Parameter	Accuracy	Remark
Voltage V	$\pm 2\%$ reading	Testec voltage probe
Current I	$\pm 0.05 mA$	Power Supply
Pressure p_{ch}	$\pm 30\%$ (gas conversion, sensor accuracy, thermal stability)	Pfeiffer pressure gauge
grid distance d	C1: $0.005m$, C2a/C2b/C3a: $0.0025m$	Manufacturing accuracy + grid positioning

Table A.1.: Parameter accuracy

Bibliography

[1] N. Wallace, P. Jameson, C. Saunders, M. Fehringer, C. Edwards, and R. Floberghagen. The goce ion propulsion assembly - lessons learnt from the first 22 months of flight operations, iepc-2011-327. *International Electric Propulsion Conference*, 2011.

[2] S. Clark, P. Randall, R. Lewis, D. Marangone, D. Goebels, V. Chaplin, H. Gray, K. Kempkens, and Wallace; N. Bepicolombo - solar electric propulsion system test and qualification approach, iepc-2019-586. *International Electric Propulsion Conference*, 2019.

[3] E.H. Cardiff and C.G. Marr. Propulsion options for the lisa mission, aiaa 2004-3440. *Joint Propulsion Conference and Exhibit*, 2004.

[4] P.T. Farnsworth. Electric discharge device for producing interactions between nuclei, 1966. US Patent 3.258.402.

[5] R.L. Hirsch. Apparatus for generating fusion reactions, 1970. US Patent 3.530.036.

[6] T.H. Rider. A general critique of inertial-electrostatic confinement fusion systems. *Physics of Plasmas*, 2(6):1853–1872, 1995.

[7] T.A. Thorson, R.D. Durst, R.J. Fonck, and L.P. Wainwright. Convergence, electrostatic potential, and density measurements in a spherically convergent ion focus. *Physics of Plasmas*, 4(1):4–15, 1997.

[8] M. Ohnishi, K.H. Sato, Y. Yamamoto, and K. Yoshikawa. Correlation between potential well structure and neutron production in inertial electrostatic confinement fusion. *Nuclear Fusion*, 5:611–619, 1997.

[9] G.H. Miley, Y. Gu, P.B. Bromley, J.H. Nadler, and J. Sved. Plasma jet source using an inertial electrostatic confinement discharge plasma, 2000. US Patent 6.121.569.

[10] J. Khachan, D. Moore, and S. Bosi. Spatial distribution of ion energies in an inertial electrostatic confinement device. *Phys. Plasmas*, 10(3):596–599, 2003.

[11] C.C. Dietrich. Improving particle confinement in inertial electrostatic fusion for spacecraft power and propulsion. Phd thesis, Massachusetts Institute of Technology, 2007.

[12] B.A. Ulmen. Formation and extraction of a dense plasma jet from a helicon plasma-injected inertial electrostatic confinement device. Phd thesis, University of Illinois at Urbana Champaign, 2013.

[13] C. Syring and G. Herdrich. Jet extraction modes of inertial electrostatic confinement devices for electric propulsion applications. *Vacuum*, 136 C:177–183, 2013.

[14] G.H. Miley and J. Sved. The iec star-mode fusion neutron source for naa, status and next-step designs. *Applied Radiation and Isotopes*, 53:779–783, 2000.

[15] ESA Requirements and Standards Division. Space engineering: adoption notice of iso 16290, space systems - definition of the technology readiness level (trls) and their criteria of assessment. *ECSS-E-AS-11C*, 1:1–12, 2014.

[16] G.H. Miley, H. Momota, L. Wu, M.P. Reilly, and V.L. Teofilo. Iec thruster for space probe applications and propulsion. *AIP Conf. Proc.*, 1103:164–174, 2009.

[17] T.J. McGuire. Improved lifetimes and synchronization behavior in multi-grid inertial electrostatic confinement fusion devices. Phd thesis, Massachusetts Institute of Technology, 2007.

[18] G. Herdrich, D. Petkow, C. Syring, and M. Pfeiffer. Kinetic modelling of the jet extraction mechanism in spherical iec devices. *Final Report, ESA Ariadna Study 12 3201*, 2013.

[19] C. Syring, M. Zürn, D. Petkow, and G. Herdrich. Thrust model and analytical assessment of losses in iec devices. *5th Russian German Conference on Electric Propulsion*, 2014.

[20] R.A. Nebel and D.C. Barnes. The periodically oscillating plasma sphere. *Fusion Technology*, 34:28–45, 1998.

[21] N. Krall. The polywell: A spherical convergent ion focus concept. *Fusion Technology*, 22:1–9, 1992.

[22] D.C. Barns, T.B. Mitchell, and M.M. Schauer. Beyond the brillouin limit with the penning fusion experiment. *Phys. Plasmas*, 4(5):1745–1751, 1997.

[23] R.L. Hirsch. Inertial-electrostatic confinement of ionized fusion gases. *Journal of Applied Physics*, 38(11):4522–4534, 1967.

[24] G. H. Miley and S. K. Murali. *Inertial electrostatic confinement (IEC) fusion: fundamentals and applications.* Springer, 2014.

[25] M. Ohnishi and H. Osawa. Particle-in-cell simulation of inertial electrostatic confinement fusion plasma. *Fusion Technology*, 39:1211–1216, 2001.

[26] K. Masuda, T. Mizutani, K. Yoshikawa, K. Nagasaki, K. Takiyama, H. Toku, H. Hashimoto, and A. Nagafuchi. Measurement of the energy distribution of fast excited atoms by doppler shift spectroscopy in an inertial-electrostatic confinement fusion device. *Proceeding 19th Symposium on Fusion Engineering*, 2002.

[27] R. Meyer. Inertial electrostatic confinement: theoretical and experimental studies of spherical devices. Phd thesis, University of Missourri-Columbia, 2007.

[28] C.C. Dobson and I. Hrbud. Electron density and two-channel neutron emission measurements in steady-state spherical inertial-electrostatically confined plasmas, with review of the one-dimensional kinetic model. *Journal of Applied Physics*, 96(1):94–108, 2004.

[29] J. Khachan and S. Collis. Measurements of ion energy distributions by doppler shift spectroscopy in an inertial-electrostatic confinement device. *Phys. Plasmas*, 8(4):1299–1304, 2001.

[30] M. Fitzgerald. Discharge physics and plasma transport in inertial electrostatic confinement devices. Phd thesis, University of Sydney, 2009.

[31] D.J. Meeker, J.T. Verdeyen, and B.E. Cherrington. Measurement of electron density in a cylindrical inertial electrostatic plasma confinement device. *Journal of Applied Physics*, 44:5347–5355, 1973.

[32] M. A. Grado-Caffaro. Fowler-nordheim electron tunneling under very intense electric field. *Optik*, 121:2001–2002, 2010.

[33] A. Küchler. *Hochspannungstechnik.* Springer Vieweg, 4 edition, 2017.

[34] S. Dushman. Electron emission from metals as a function of temperature. *Phys. Rev.*, 21:623, 1923.

[35] A. Bogaerts, E. Neyts, R. Gijbels, and J. v.d.Mullen. Gas discharge plasmas and their applications. *Spectrochimica Acta Part B*, 57:609–658, 2002.

[36] M. H. Mittleman and L. Wilets. Statistical treatment of ionization in atomic collisions. *Physical Review*, 154(1):12–16, 1967.

[37] W.C. Elmore, J.L. Tuck, and K.M. Watson. On the inertial-electrostatic confinement of a plasma. *The Physics of Fluids*, 2(3):239–246, 1959.

[38] T.J. Dolan. Electrostatic-inertial plasma confinement. *Journal of Applied Physics*, 43:4, 1972.

[39] W.M. Manheimer and R.F. Fernsler. Plasma acceleration by area expansion. *IEEE Transactions on Plasma Science*, pages 75–84, 2001.

[40] G. Herdrich, C. Syring, T. Torgau, Y.-A. Chan, and D. Petkow. An approach for thrust and losses in inertial electrostatic confinement devices for electric propulsion applications. *34th International Electric Propulsion Conference*, 2015.

[41] I.H. Hutchinson. *Principles of plasma diagnostics*. Cambridge University Press, 2 edition, 2002.

[42] T. Torgau. Development of a tool for the assessment of losses in iec plasma sources. Diploma thesis, University of Stuttgart, 2014.

[43] M.N. Saha. Ionization in the solar chromosphere. *The London, Edinburgh, and Dublin Philosophical Magazine and Journal of Science*, 40(238):472–488, 1920.

[44] M.R. Zaghloul, M.A. Bourham, and J.M. Doster. A simple formulation and solution strategy of the saha equation for ideal and nonideal plasmas. *Physics D: Applied Physics*, 33(8):977, 2000.

[45] W. Lotz. Electron-impact ionization cross-sections and ionization rate coefficients for atoms and ions. *Astrophysical Journal Supplement*, 14:207–238, 1967.

[46] S.A. Chernyi, G.G.and Losev, S.O. Macheret, and B.V. Potapkin. Physical and chemical processes in gas dynamics: cross sections and rate constants. *Progress in Astronautics and Aeronautics*, i:196–311, 2002.

[47] Nist atomic spectra database ionization energies form. `https://physics.nist.gov/PhysRefData/ASD/ionEnergy.html`. Accessed 2019-02-28.

[48] D. Petkow, R.A. Gabrielli, G. Herdrich, R. Laufer, and H.-P. Röser. Generalized lawson criterion for magnetic fusion applications in space. *Fusion Engineering and Design*, 87(1):30–38, 2012.

[49] S. Maxon. Bremsstrahlung rate and spectra from hot gas (z=1). *Physical Review A*, 5:1630–1633, 1972.

[50] G. Herdrich. Raumfahrtrelevante plasmen und deren anwendungsbezogene klassifizierung. Habilitation, Institut für Raumfahrtsysteme, Universität Stuttgart, 2012.

[51] D.M. Goebel and I. Katz. *Fundamentals of electric propulsion: ion and hall thrusters.* Wiley, 1st edition, 2008.